

¹ A Search in the Two-Photon Final State for
² Evidence of New Particle Production in pp
³ Collisions at $\sqrt{s} = 7$ TeV

⁴ Rachel P. Yohay
University of Virginia
`rpy3y@virginia.edu`

⁵ May 29, 2012

Contents

7	1	The Supersymmetric Extension to the Standard Model	3
8	1.1	Supermultiplet Representation	3
9	1.2	The Unbroken SUSY Lagrangian	4
10	1.3	Soft SUSY Breaking	10
11	1.4	Gauge-Mediated SUSY Breaking	12
12	1.5	Phenomenology of General Gauge Mediation	15
13	1.6	Experimental Status of SUSY	19
14	2	Event Selection	23
15	2.1	Object Reconstruction	24
16	2.1.1	Photons	24
17	2.1.2	Electrons	35
18	2.1.3	Jets and Missing Transverse Energy	35
19	2.2	HLT	41
20	2.3	Event Quality	44
21	2.4	Photon Identification Efficiency	47
22	2.4.1	Tag and Probe Method	48
23	2.4.2	Photon Efficiency Scale Factor $\epsilon_e^{\text{data}}/\epsilon_e^{\text{MC}}$	51
24	3	Data Analysis	56
25	3.1	Modeling the QCD Background	60

26	3.1.1	Outline of the Procedure	60
27	3.1.2	Reweighting	61
28	3.1.3	Normalization	72
29	3.2	Modeling the Electroweak Background	72
30	3.3	Errors on the Background Prediction	78
31	3.4	Results	84
32	4	Interpretation of Results in Terms of GMSB Models	90
33	4.1	Simplified Models	90
34	4.2	Upper Limit Calculation and Model Exclusion	92
35	4.2.1	Signal Acceptance \times Efficiency	92
36	4.2.2	CL_s and the Profile Likelihood Test Statistic	96
37	4.3	Cross Section Upper Limits	103
38	4.4	Exclusion Contours	104
39	A	Monte Carlo Samples	109
40	A.0.1	List of Samples	109
41	A.0.2	Explanation of Naming Conventions	110

⁴² **Chapter 1**

⁴³ **The Supersymmetric Extension to
the Standard Model**

⁴⁵ The following introduction to SUSY focuses primarily on the aspects of the formalism that are relevant to phenomenology. In particular, most of the details of SUSY breaking (about which there is little theoretical consensus) are omitted, except where they are relevant to experiment. The notation is similar to that used in refs. [5] and [6], and much of the information presented is culled from those references.

⁵⁰ **1.1 Supermultiplet Representation**

⁵¹ The Standard Model is extended to include supersymmetry by the introduction of a supersymmetry transformation that takes fermionic states to bosonic states and vice versa. The resulting model is called the *minimal supersymmetric Standard Model* (MSSM). In analogy with the known symmetries of the Standard Model, the SUSY transformation has associated generators that obey defining commutation and anti-commutation relations, and a fundamental representation. All SM particles and their superpartners fall into one of two *supermultiplet* representations. Using the property that

$$n_F = n_B, \quad (1.1)$$

59 where n_F is the number of fermionic degrees of freedom per supermultiplet and n_B is
 60 the number of bosonic degrees of freedom, the two types of supermultiplets are

- 61 1. *Chiral supermultiplets*: one Weyl fermion (two helicity states $\Rightarrow n_F = 2$) and
 62 one complex scalar field (with two real components $\Rightarrow n_B = 2$)

 63 2. *Gauge supermultiplets*: One spin-1 vector boson (two helicity states $\Rightarrow n_B = 2$)
 64 and one Weyl fermion (two helicity states $\Rightarrow n_F = 2$)

65 In the gauge supermultiplet, the vector boson is assumed massless (i.e. before
 66 EWSB generates a mass for it). Since the superpartners to the SM particles have not
 67 yet been discovered, they must be significantly heavier than their SM counterparts.
 68 Unbroken SUSY predicts that the SM particles and their superpartners must have
 69 exactly the same mass, so ultimately a mechanism for SUSY breaking must be intro-
 70 duced to generate masses for the superpartners (see Sec. 1.3). Tables 1.1 and 1.2 show
 71 the chiral and gauge supermultiplets of the MSSM, respectively. Note that the scalar
 72 partners to the SM fermions are denoted by placing an “s” in front of their names,
 73 while the chiral fermion partners to the SM gauge bosons are denoted by appending
 74 “ino” to their names.

75 1.2 The Unbroken SUSY Lagrangian

76 The first piece of the full unbroken SUSY Lagrangian density consists of the kinetic
 77 and interacting terms related to the chiral supermultiplets. As explained in Sec. 1.1,
 78 a chiral supermultiplet consists of a Weyl fermion ψ (the ordinary fermion) and a
 79 complex scalar ϕ (the sfermion). For a collection of such chiral supermultiplets, the
 80 Lagrangian is

Table 1.1: Chiral supermultiplets of the supersymmetric Standard Model. Adapted from Table 1.1 of ref. [6].

Type of supermultiplet	Notation	Spin-0 component	Spin-1/2 component	Representation under $SU(3)_C \otimes SU(2)_L \otimes U(1)_Y$
Left-handed quark/squark doublet ($\times 3$ families)	Q	$(\tilde{u}_L \tilde{d}_L)$	$(u_L d_L)$	$(\mathbf{3}, \mathbf{2}, \frac{1}{6})$
Right-handed up-type quark/squark singlet ($\times 3$ families)	\bar{u}	\tilde{u}_R^*	u_R^\dagger	$(\bar{\mathbf{3}}, \mathbf{1}, -\frac{2}{3})$
Right-handed down-type quark/squark singlet ($\times 3$ families)	\bar{d}	\tilde{d}_R^*	d_R^\dagger	$(\bar{\mathbf{3}}, \mathbf{1}, \frac{1}{3})$
Left-handed lepton/slepton doublet ($\times 3$ families)	L	$(\tilde{\nu}_{eL} \tilde{e}_L)$	$(\bar{\nu}_{eL} e_L)$	$(\mathbf{1}, \mathbf{2}, -\frac{1}{2})$
Right-handed lepton/slepton singlet ($\times 3$ families)	\bar{e}	\tilde{e}_R^*	e_R^\dagger	$(\bar{\mathbf{1}}, \mathbf{1}, 1)$
Up-type Higgs/Higgsino doublet	H_u	$(H_u^+ H_u^0)$	$(\tilde{H}_u^+ \tilde{H}_u^0)$	$(\mathbf{1}, \mathbf{2}, \frac{1}{2})$
Down-type Higgs/Higgsino doublet	H_d	$(H_d^0 H_d^-)$	$(\tilde{H}_d^0 \tilde{H}_d^-)$	$(\mathbf{1}, \mathbf{2}, -\frac{1}{2})$

Table 1.2: Gauge supermultiplets of the supersymmetric Standard Model. Adapted from Table 1.2 of ref. [6].

Type of supermultiplet	Spin-1/2 component	Spin-1 component	Representation under $SU(3)_C \otimes SU(2)_L \otimes U(1)_Y$
Gluon/gluino	\tilde{g}	g	$(\mathbf{8}, \mathbf{1}, 0)$
W/wino	$\tilde{W}^\pm \tilde{W}^0$	$W^\pm W^0$	$(\mathbf{1}, \mathbf{3}, 0)$
B/bino	\tilde{B}^0	B^0	$(\mathbf{1}, \mathbf{1}, 0)$

$$\begin{aligned}\mathcal{L}_{\text{chiral}} = & -\partial^\mu \phi^{*i} \partial_\mu \phi_i - V_{\text{chiral}}(\phi, \phi^*) - i\psi^{\dagger i} \bar{\sigma}^\mu \partial_\mu \psi_i - \frac{1}{2} M^{ij} \psi_i \psi_j \\ & - \frac{1}{2} M_{ij}^* \psi^{\dagger i} \psi^{\dagger j} - \frac{1}{2} y^{ijk} \phi_i \psi_j \psi_k - \frac{1}{2} y_{ijk}^* \phi^{*i} \psi^{\dagger j} \psi^{\dagger k}\end{aligned}\quad (1.2)$$

where i runs over all supermultiplets in Table 1.1, $\bar{\sigma}^\mu$ are $-1 \times$ the Pauli matrices (except for $\sigma^0 = \bar{\sigma}^0$), M^{ij} is a mass matrix for the fermions, y^{ijk} are the Yukawa couplings between one scalar and two spinor fields, and $V_{\text{chiral}}(\phi, \phi^*)$ is the scalar potential

$$\begin{aligned}V_{\text{chiral}}(\phi, \phi^*) = & M_{ik}^* M^{kj} \phi^{*i} \phi_j + \frac{1}{2} M^{in} y_{jkn}^* \phi_i \phi^{*j} \phi^{*k} \\ & + \frac{1}{2} M_{in}^* y^{jkn} \phi^{*i} \phi_j \phi_k + \frac{1}{4} y^{ijn} y_{klm}^* \phi_i \phi_j \phi^{*k} \phi^{*l}.\end{aligned}\quad (1.3)$$

The Lagrangian can also be written as the kinetic terms plus derivatives of the *superpotential* W :

$$\begin{aligned}\mathcal{L}_{\text{chiral}} = & -\partial^\mu \phi^{*i} \partial_\mu \phi_i - i\psi^{\dagger i} \bar{\sigma}^\mu \partial_\mu \psi_i \\ & - \frac{1}{2} \left(\frac{\delta^2 W}{\delta \phi^i \delta \phi^j} \psi_i \psi_j + \frac{\delta^2 W^*}{\delta \phi_i \delta \phi_j} \psi^{\dagger i} \psi^{\dagger j} \right) - \frac{\delta W}{\delta \phi^i} \frac{\delta W^*}{\delta \phi_i}\end{aligned}\quad (1.4)$$

where

$$W = M^{ij} \phi_i \phi_j + \frac{1}{6} y^{ijk} \phi_i \phi_j \phi_k. \quad (1.5)$$

The second part of the Lagrangian involves the gauge supermultiplets. In terms of the spin-1 ordinary gauge boson A_μ^a and the spin-1/2 Weyl spinor gaugino λ^a of

⁹⁰ the gauge supermultiplet, where a runs over the number of generators for the SM
⁹¹ subgroup (i.e. 1-8 for $SU(3)_C$, 1-3 for $SU(2)_L$, and 1 for $U(1)_Y$), this part of the
⁹² Lagrangian is

$$\mathcal{L}_{\text{gauge}} = -\frac{1}{4}F_{\mu\nu}^a F^{\mu\nu a} - i\lambda^{\dagger a}\bar{\sigma}^\mu D_\mu \lambda^a + \frac{1}{2}D^a D^a \quad (1.6)$$

⁹³ where

$$F_{\mu\nu}^a = \partial_\mu A_\nu^a - \partial_\nu A_\mu^a + g f^{abc} A_\mu^b A_\nu^c \quad (1.7)$$

⁹⁴ (g is the coupling constant and f^{abc} are the structure constants for the particular SM
⁹⁵ gauge group),

$$D_\mu \lambda^a = \partial_\mu \lambda^a + g f^{abc} A_\mu^b \lambda^c, \quad (1.8)$$

⁹⁶ and D^a is an auxiliary field that does not propagate (in the literature, it is used as a
⁹⁷ bookkeeping tool and can be removed via its algebraic equation of motion).

⁹⁸ To build a fully supersymmetric and gauge-invariant Lagrangian, the ordinary
⁹⁹ derivatives in $\mathcal{L}_{\text{chiral}}$ (Eq. 1.2) must be replaced by covariant derivatives

$$D_\mu \phi_i = \partial_\mu \phi_i - ig A_\mu^a (T^a \phi)_i \quad (1.9)$$

$$D_\mu \phi^{*i} = \partial_\mu \phi^{*i} + ig A_\mu^a (\phi^* T^a)^i \quad (1.10)$$

$$D_\mu \psi_i = \partial_\mu \psi_i - ig A_\mu^a (T^a \psi)_i. \quad (1.11)$$

¹⁰⁰ This leads to the full Lagrangian

$$\begin{aligned}
\mathcal{L} &= \mathcal{L}_{\text{chiral}} + \mathcal{L}_{\text{gauge}} \\
&\quad - \sqrt{2}g(\phi^{*i}T^a\psi_i)\lambda^a - \sqrt{2}g\lambda^{\dagger a}(\psi^{\dagger i}T^a\phi_i) + g(\phi^{*i}T^a\phi_i)D^a \\
&= -\partial^\mu\phi^{*i}\partial_\mu\phi_i - i\psi^{\dagger i}\bar{\sigma}^\mu\partial_\mu\psi_i + ig\partial^\mu\phi^{*i}A_\mu^a(T^a\phi)_i - ig\partial_\mu\phi_iA^{\mu a}(\phi^*T^a)^i \\
&\quad - g^2A^{\mu a}(\phi^*T^a)^iA_\mu^a(T^a\phi)_i - g\psi^{\dagger i}\bar{\sigma}^\mu A_\mu^a(T^a\psi)_i - V_{\text{chiral}}(\phi, \phi^*) \\
&\quad - \frac{1}{2}M^{ij}\psi_i\psi_j - \frac{1}{2}M_{ij}^*\psi^{\dagger i}\psi^{\dagger j} - \frac{1}{2}y^{ijk}\phi_i\psi_j\psi_k - \frac{1}{2}y_{ijk}^*\phi^{*i}\psi^{\dagger j}\psi^{\dagger k} \\
&\quad - \frac{1}{4}F_{\mu\nu}^aF^{\mu\nu a} - i\lambda^{\dagger a}\bar{\sigma}^\mu\partial_\mu\lambda^a - ig\lambda^{\dagger a}\bar{\sigma}^\mu f^{abc}A_\mu^b\lambda^c + \frac{1}{2}D^aD^a \\
&\quad - \sqrt{2}g(\phi^{*i}T^a\psi_i)\lambda^a - \sqrt{2}g\lambda^{\dagger a}(\psi^{\dagger i}T^a\phi_i) + g(\phi^{*i}T^a\phi_i)D^a. \tag{1.12}
\end{aligned}$$

¹⁰¹ Writing out $F_{\mu\nu}^a$ and $V_{\text{chiral}}(\phi, \phi^*)$ explicitly combining the D^a terms using the equation

¹⁰² of motion $D^a = -g\phi^{*i}T^a\phi_i$, and rearranging some terms, the final unbroken SUSY

¹⁰³ Lagrangian is

$$\begin{aligned}
\mathcal{L} = & -\partial^\mu \phi^{*i} \partial_\mu \phi_i - i\psi^{\dagger i} \bar{\sigma}^\mu \partial_\mu \psi_i \\
& - \frac{1}{4} (\partial_\mu A_\nu^a - \partial_\nu A_\mu^a) (\partial^\mu A^{\nu a} - \partial^\nu A^{\mu a}) - i\lambda^{\dagger a} \bar{\sigma}^\mu \partial_\mu \lambda^a \\
& - M_{ik}^* M^{kj} \phi^{*i} \phi_j - \frac{1}{2} M^{ij} \psi_i \psi_j - \frac{1}{2} M_{ij}^* \psi^{\dagger i} \psi^{\dagger j} \\
& + ig \partial^\mu \phi^{*i} A_\mu^a (T^a \phi)_i - ig \partial_\mu \phi_i A^{\mu a} (\phi^* T^a)^i - g \psi^{\dagger i} \bar{\sigma}^\mu A_\mu^a (T^a \psi)_i \\
& - ig \lambda^{\dagger a} \bar{\sigma}^\mu f^{abc} A_\mu^b \lambda^c \\
& - \frac{1}{4} g f^{abc} [(\partial_\mu A_\nu^a - \partial_\nu A_\mu^a) A^{\mu b} A^{\nu c} + A_\mu^b A_\nu^c (\partial^\mu A^{\nu a} - \partial^\nu A^{\mu a})] \\
& - \frac{1}{2} M_{in}^* y^{jkn} \phi^{*i} \phi_j \phi_k - \frac{1}{2} M^{in} y_{jkn}^* \phi_i \phi^{*j} \phi^{*k} \\
& - \frac{1}{2} y^{ijk} \phi_i \psi_j \psi_k - \frac{1}{2} y_{ijk}^* \phi^{*i} \psi^{\dagger j} \psi^{\dagger k} \\
& - \sqrt{2} g (\phi^{*i} T^a \psi_i) \lambda^a - \sqrt{2} g \lambda^{\dagger a} (\psi^{\dagger i} T^a \phi_i) \\
& - g^2 A^{\mu a} (\phi^* T^a)^i A_\mu^a (T^a \phi)_i - \frac{1}{4} g^2 f^{abc} A_\mu^b A_\nu^c f^{abc} A^{\mu b} A^{\nu c} \\
& - \frac{1}{4} y^{ijn} y_{kln}^* \phi_i \phi_j \phi^{*k} \phi^{*l} - \frac{1}{2} g^2 (\phi^{*i} T^a \phi_i)^2.
\end{aligned} \tag{1.13}$$

¹⁰⁴ The above Lagrangian applies to chiral supermultiplets interacting with one kind
¹⁰⁵ of gauge supermultiplet (i.e. one SM gauge group). In the general case, there are
¹⁰⁶ additional terms corresponding to interactions with all three SM gauge groups.

¹⁰⁷ The following list gives a description of the terms in Eq. 1.13:

- ¹⁰⁸ • First two lines: kinetic terms for the four types of fields ϕ_i , ψ_i , A_μ^a , and λ^a
- ¹⁰⁹ • Third line: mass terms for the ϕ_i and ψ_i (see Figs. 1.1(a) and 1.1(b))
- ¹¹⁰ • Fourth and fifth lines: cubic couplings in which ϕ_i , ψ_i , or λ^a radiates an A_μ^a (see
¹¹¹ Figs. 1.1(c), 1.1(d), and 1.1(e))
- ¹¹² • Sixth line: triple gauge boson couplings (see Fig. 1.1(f))
- ¹¹³ • Seventh line: triple sfermion couplings (see Fig. 1.1(g))

- ¹¹⁴ • Eighth line: cubic couplings in which ψ_i radiates a ϕ_i (see Fig. 1.1(h))
- ¹¹⁵ • Ninth line: ϕ_i - ψ_i - λ^a vertices (see Fig. 1.1(i))
- ¹¹⁶ • 10th line: A_μ^a - A_μ^a - ϕ_i - ϕ_i and quadruple gauge boson couplings (see Figs. 1.1(j)
¹¹⁷ and 1.1(k))
- ¹¹⁸ • 11th line: ϕ_i^4 vertices (see Figs. 1.1(l) and 1.1(m))

¹¹⁹ 1.3 Soft SUSY Breaking

¹²⁰ Since quadratic divergences in sfermion masses vanish to all orders in perturbation
¹²¹ theory in plain unbroken SUSY [6] due to the presence of gauge and Yukawa interac-
¹²² tions with the necessary relationships between coupling constants, it is desirable that
¹²³ the terms that break SUSY not disturb this property. In addition, SUSY should be
¹²⁴ broken spontaneously, as electroweak symmetry is broken in the Standard Model, so
¹²⁵ that it is only made manifest at high energies. To satisfy these constraints, SUSY-
¹²⁶ breaking terms are simply added to the unbroken SUSY Lagrangian in Eq. 1.13 such
¹²⁷ that $\mathcal{L}_{\text{total}} = \mathcal{L}_{\text{unbroken}} + \mathcal{L}_{\text{breaking}}$. The coefficients of terms in $\mathcal{L}_{\text{breaking}}$ must have
¹²⁸ positive mass dimension in order not to contribute quadratically divergent loop cor-
¹²⁹ rections to the scalar masses (like the Higgs mass).¹ This form of SUSY breaking is
¹³⁰ called *soft*, and all coefficients of soft SUSY breaking terms are expected to be of
¹³¹ order m_{soft} or m_{soft}^2 .

¹This point can be argued via dimensional analysis. Radiative corrections take the form Δm_S^2 , where m_S is the mass of the scalar particle in question. The dimensions of Δm_S^2 are mass². Δm_S^2 is proportional to some coupling constant or mass coefficient k multiplied by a function of Λ_{UV} , the high energy cutoff scale. The function of Λ_{UV} is determined by a loop integral, and thus typically takes the form Λ_{UV}^2 (quadratically divergent) or $\ln \frac{\Lambda_{\text{UV}}}{m_{\text{low}}}$ (logarithmically divergent, where m_{low} is some other lower-mass scale in the problem). Now, if k already contributes at least one power of mass to Δm_S^2 , then the high-energy behavior—the function of Λ_{UV} —can only contribute at most one power of the dimensionful parameter Λ_{UV} . However, there are typically no loop integrals that diverge linearly in Λ_{UV} , so by forcing k to have positive mass dimension, the form of the radiative corrections contributed by SUSY-breaking terms is limited to $\Delta m_S^2 \sim m_{\text{low}}^2 \ln \frac{\Lambda_{\text{UV}}}{m_{\text{low}}}$. In effect, the possibility of dangerous corrections proportional to Λ_{UV}^2 is excluded by dimensional analysis if the requirement that k contribute at least one power of mass is enforced.

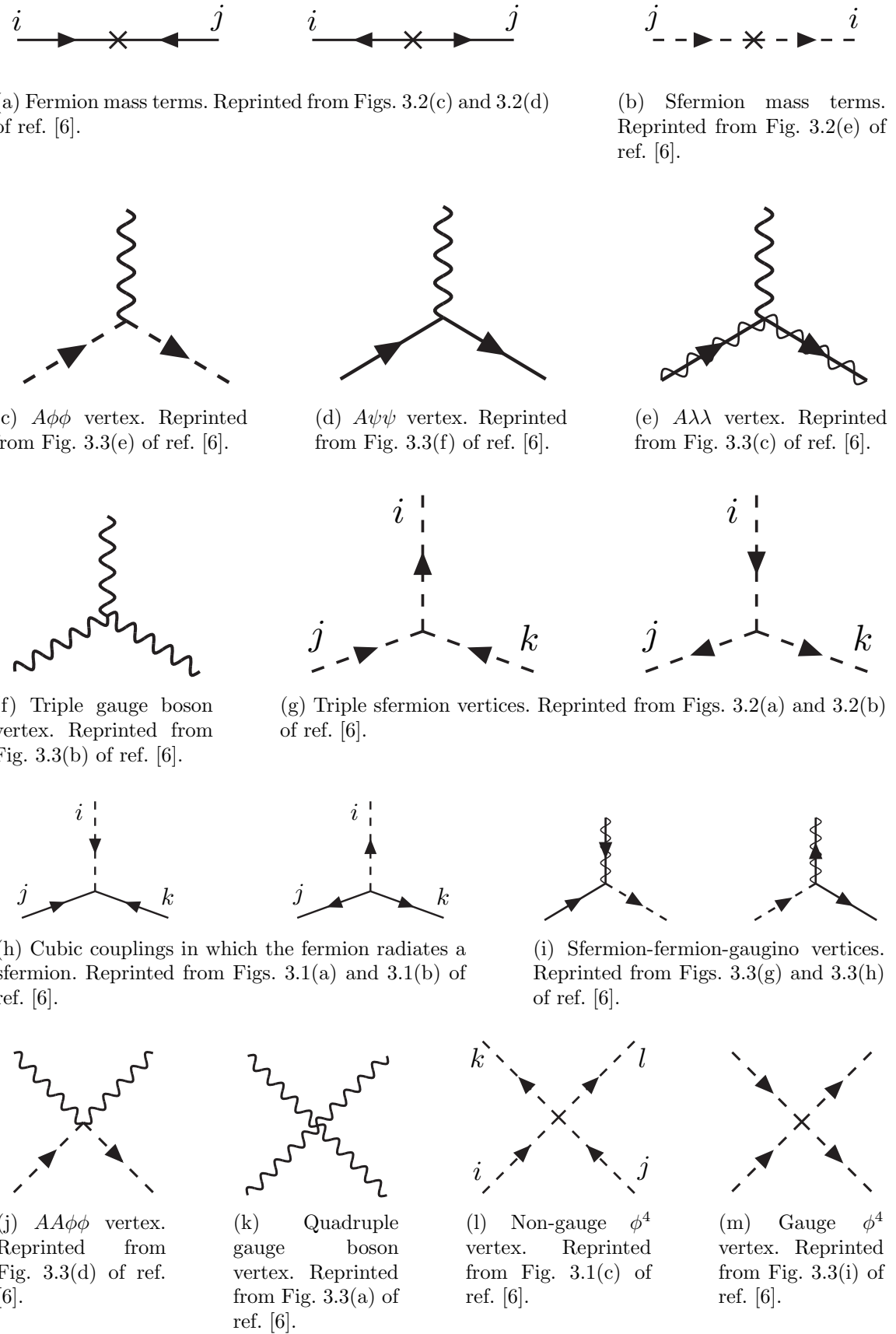


Figure 1.1: Interactions in the unbroken SUSY Lagrangian.

¹³² Soft SUSY breaking terms give masses to the sfermions and gauginos and introduce
¹³³ a cubic sfermion vertex. The soft terms are given by

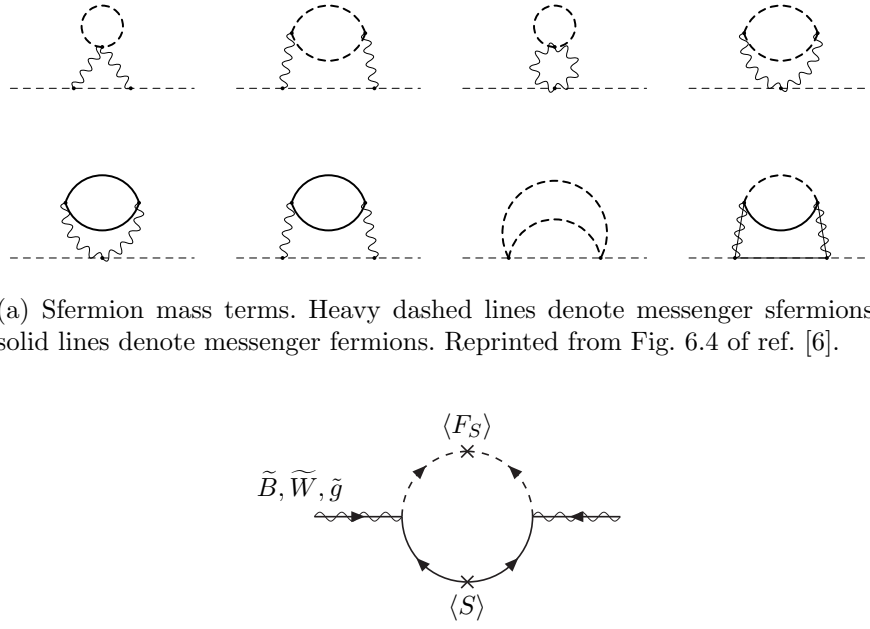
$$\begin{aligned}
 \mathcal{L}_{\text{soft}} = & -\frac{1}{2}(M_3\tilde{g}^a\tilde{g}^a + M_2\tilde{W}^a\tilde{W}^a + M_1\tilde{B}\tilde{B} + \text{h.c.}) \\
 & - (a_u^{ij}\tilde{u}_{Ri}^*\tilde{Q}_j H_u - a_d^{ij}\tilde{d}_{Ri}^*\tilde{Q}_j H_d - a_e^{ij}\tilde{e}_{Ri}^*\tilde{L}_j H_d + \text{h.c.}) \\
 & - m_{\tilde{Q}_{ij}}^2 \tilde{Q}_i^\dagger \tilde{Q}_j - m_{\tilde{L}_{ij}}^2 \tilde{L}_i^\dagger \tilde{L}_j \\
 & - m_{\tilde{u}_{ij}}^2 \tilde{u}_{Ri}^* \tilde{u}_{Rj}^* - m_{\tilde{d}_{ij}}^2 \tilde{d}_{Ri}^* \tilde{d}_{Rj}^* - m_{\tilde{e}_{ij}}^2 \tilde{e}_{Ri}^* \tilde{e}_{Rj}^* \\
 & - m_{H_u}^2 H_u^* H_u - m_{H_d}^2 H_d^* H_d - (b H_u H_d + \text{h.c.})
 \end{aligned} \tag{1.14}$$

¹³⁴ where a runs from 1-8 for \tilde{g}^a and from 1-3 for \tilde{W}^a , and i, j run over the three families.
¹³⁵ The color indices are not shown. The first line of Eq. 1.14 contains the gaugino mass
¹³⁶ terms. The second line contains cubic scalar couplings that contribute to mixing
¹³⁷ between the left- and right-handed third generation sfermions (it is assumed in the
¹³⁸ supersymmetric Standard Model that the a_u^{ij} , a_d^{ij} , and a_e^{ij} are negligible unless $i =$
¹³⁹ $j = 3$). The third and fourth lines of Eq. 1.14 contain squark and slepton mass terms,
¹⁴⁰ and finally the last line contains the Higgs mass terms.

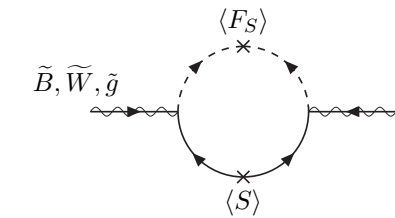
¹⁴¹ Many viable models of achieving soft SUSY breaking have been studied over the
¹⁴² last 30 years. For an overview, see Sec. 6 of ref. [6]. However, this thesis will only cover
¹⁴³ *gauge-mediated SUSY breaking* (GMSB), because the two-photon search performed
¹⁴⁴ is far more sensitive to this model than to other models of SUSY breaking.

¹⁴⁵ 1.4 Gauge-Mediated SUSY Breaking

¹⁴⁶ In gauge-mediated models [7], “hidden” fields spontaneously break the supersymme-
¹⁴⁷ try of very heavy chiral *messenger* supermultiplets. There are a number of compet-
¹⁴⁸ ing models (see ref. [7]) that explain the precise mechanism of spontaneous SUSY



(a) Sfermion mass terms. Heavy dashed lines denote messenger sfermions; solid lines denote messenger fermions. Reprinted from Fig. 6.4 of ref. [6].



(b) Gaugino mass term. The $\langle S \rangle$ part of the loop is a messenger fermion contribution; the $\langle F_S \rangle$ part is a messenger sfermion contribution. Reprinted from Fig. 6.3 of ref. [6].

Figure 1.2: Contributions to sfermion and gaugino masses from loop interactions with messenger particles in the GMSB framework.

149 breaking, but fortunately the details of those models mostly decouple from the phe-
 150 nomenology of GMSB. The messengers then communicate the SUSY breaking to the
 151 sparticles via loop diagrams of gauge interaction strength (i.e. via vertices like those
 152 shown in Figs. 1.1(c), 1.1(d), 1.1(i), 1.1(j), and 1.1(m), which are proportional to
 153 the SM gauge couplings constants). Feynman diagrams corresponding to gaugino and
 154 sfermion mass terms are shown in Figure 1.2.

155 Historically, GMSB and gravity-mediated SUSY breaking, or mSUGRA [8], have
 156 been the two most thoroughly experimentally studied scenarios of SUSY breaking.
 157 One advantage of GMSB over mSUGRA is that it naturally suppresses flavor vio-
 158 lation, a generic prediction of supersymmetry. Flavor violation is introduced in the
 159 scalar³ couplings and sfermion mass terms of $\mathcal{L}_{\text{soft}}$ (second, third, and fourth lines of

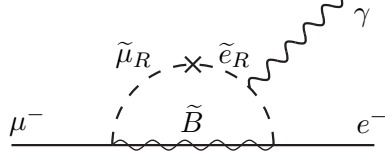


Figure 1.3: Possible contribution to $\mu \rightarrow e\gamma$ from $m_{\tilde{e}ij}$ soft term. Reprinted from Fig. 5.6(a) of ref. [6].

Eq. 1.14). Since a_u^{ij} , a_d^{ij} , a_e^{ij} , m_{Qij} , m_{Lij} , $m_{\tilde{u}ij}$, $m_{\tilde{d}ij}$, and $m_{\tilde{e}ij}$ are matrices in family space, any nonzero off-diagonal elements will lead to mixing between sfermions of different families. This can lead, for example, to contributions to the diagram $\mu \rightarrow e\gamma$ (Figure 1.3) exceeding the experimental bounds. To avoid this disaster, *universality* conditions are assumed:

$$\mathbf{m}_{\tilde{Q}}^2 = m_{\tilde{Q}}^2 \mathbf{1}, \mathbf{m}_{\tilde{L}}^2 = m_{\tilde{L}}^2 \mathbf{1}, \mathbf{m}_{\tilde{u}}^2 = m_{\tilde{u}}^2 \mathbf{1}, \mathbf{m}_{\tilde{d}}^2 = m_{\tilde{d}}^2 \mathbf{1}, \mathbf{m}_{\tilde{e}}^2 = m_{\tilde{e}}^2 \mathbf{1} \quad (1.15)$$

i.e. all sfermion mass matrices arising from the soft terms are assumed to be proportional to the unit matrix $\mathbf{1}$, such that there can be no flavor mixing from these terms and contributions to flavor-changing processes are drastically reduced.² In mSUGRA models, universality is assumed from the beginning, while in GMSB it is a natural consequence of the fact that the sparticle-messenger vertices are flavor-blind.

In minimal GMSB (mGMSB), there are four messenger supermultiplets q, \bar{q}, l, \bar{l} providing the messenger (s)quarks and (s)leptons. There is one breaking scale Λ . The gaugino masses computed from diagrams like Fig. 1.2(b) are given by

$$M_a = \frac{\alpha_a}{4\pi} \Lambda \quad (1.16)$$

²Universality also includes some assumptions about the form of a_{uij} , a_{dij} , and a_{eij} and the stipulation that the soft terms not introduce any CP-violating phases.

¹⁷³ where a runs from 1-3 and the α_a are the SM gauge coupling constants. The sfermion
¹⁷⁴ masses computed from diagrams like Fig. 1.2(a) are given by

$$m_{\phi_i}^2 = 2\Lambda^2 \sum_{a=1}^3 \left(\frac{\alpha_a}{4\pi}\right)^2 C_a(i) \quad (1.17)$$

¹⁷⁵ where $C_a(i)$ are group theory factors that are identical for all particles residing in
¹⁷⁶ the same type of supermultiplet (e.g. for all left-handed (s)quarks or left-handed
¹⁷⁷ (s)leptons). As explained in the previous paragraph, the gaugino and sfermion masses
¹⁷⁸ do not depend on fermion family.

¹⁷⁹ In recent years, much theoretical progress has been made in unifying models of
¹⁸⁰ gauge mediation and developing less restrictive models than mGMSB. *General gauge*
¹⁸¹ *mediation* (GGM) [9] retains the essential features of mGMSB, such as flavor de-
¹⁸² generacy and communication of SUSY breaking via messengers, but does not make
¹⁸³ assumptions about the specific messenger sector or SUSY breaking scale. Many dif-
¹⁸⁴ ferent collider final states can be interpreted in terms of GGM, and conversely, GGM
¹⁸⁵ implies a wealth of signatures, only a small fraction of which have been searched for
¹⁸⁶ at colliders [10, 11, 12]. The following section discusses the aspects of GGM collider
¹⁸⁷ phenomenology relevant to this thesis.

¹⁸⁸ 1.5 Phenomenology of General Gauge Mediation

¹⁸⁹ The main distinguishing feature of all GMSB phenomenology is that the gravitino \tilde{G} is
¹⁹⁰ very light (eV-keV). In general, the gravitino mass is proportional to $\langle F \rangle / M_P$, where
¹⁹¹ $\langle F \rangle$ is the vacuum expectation value (VEV) of a field F that spontaneously breaks
¹⁹² SUSY in the vacuum state and M_P is the Planck mass. In GGM models, $\langle F \rangle \sim 10^8$
¹⁹³ GeV, leading to a very light gravitino. In contrast, mSUGRA predicts $\langle F \rangle \sim 10^{20}$
¹⁹⁴ GeV. The fact that the gravitino is so much lighter than any other particles in the

¹⁹⁵ supersymmetric Standard Model, and that it interacts only gravitationally (and thus
¹⁹⁶ extremely feebly), leads to two important phenomenological consequences:

- ¹⁹⁷ 1. All sparticle decay chains end with the production of a gravitino.
- ¹⁹⁸ 2. The gravitino escapes 4π , hermetic collider detectors without interacting, leav-
¹⁹⁹ ing a signature of “missing” momentum transverse to the beam direction.

²⁰⁰ Even if the gravitino were lighter than any other sparticle, but heavier than an
²⁰¹ ordinary SM particle, it still could not decay to the SM particle due to *R-parity*. R-
²⁰² parity is a conserved quantity of the supersymmetric Standard Model that enforces
²⁰³ baryon and lepton number conservation, which would otherwise be generically allowed
²⁰⁴ at levels in conflict with experiment (e.g. the non-observation of baryon- and lepton-
²⁰⁵ number-violating proton decay). All sparticles have R-parity -1, while all ordinary SM
²⁰⁶ particles have R-parity +1, and R-parity conservation dictates that at any vertex, the
²⁰⁷ product of the R-parities of each leg must be +1. This leads to two more important
²⁰⁸ consequences:

- ²⁰⁹ 1. Since conservation of energy only allows it to decay to ordinary SM particles,
²¹⁰ but R-parity prevents a sparticle-particle-particle vertex, the *lightest supersym-
²¹¹ metric particle* (LSP) must be absolutely stable. All sparticle decays proceed
²¹² through the *next-to-lightest supersymmetric particle* (NLSP), which in turn de-
²¹³ cays to the LSP. The fact that it is stable and only gravitationally interacting
²¹⁴ makes the gravitino a candidate dark matter particle (see Sec. 1.6).
- ²¹⁵ 2. In colliders, sparticles are produced in pairs (particle + particle \rightarrow sparticle +
²¹⁶ sparticle).

²¹⁷ In GMSB, then, the gravitino is the LSP. If the NLSP is a gaugino,³ then the
²¹⁸ possible decays depend on mixing among the gauginos. Due to the effects of EWSB,

³In principle, the NLSP could be anything, but in most popular GGM models, it is either a gaugino or a stau. The stau NLSP search is not the subject of this thesis, so it will not be considered in this section.

²¹⁹ the four neutral gauginos \tilde{H}_u^0 , \tilde{H}_d^0 , \tilde{B} , \tilde{W}^0 mix into four *neutralino* mass eigenstates
²²⁰ $\tilde{\chi}_1^0, \tilde{\chi}_2^0, \tilde{\chi}_3^0, \tilde{\chi}_4^0$, and the four charged gauginos $\tilde{H}_u^+, \tilde{H}_d^-, \tilde{W}^+, \tilde{W}^-$ mix into two *chargino*
²²¹ mass eigenstates $\tilde{\chi}_1^\pm, \tilde{\chi}_2^\pm$ (two mass eigenstates each with two possible charges = four
²²² particles). In the limit that EWSB effects are small, the neutralino and chargino
²²³ masses can be written as the gauge eigenstate masses plus a small perturbation:

$$m_{\tilde{\chi}_1^0} = M_1 - \frac{m_Z^2 \sin^2 \theta_W (M_1 + \mu \sin 2\beta)}{\mu^2 - M_1^2} + \dots \quad (1.18)$$

$$m_{\tilde{\chi}_2^0} = M_2 - \frac{m_W^2 (M_2 + \mu \sin 2\beta)}{\mu^2 - M_2^2} + \dots \quad (1.19)$$

$$m_{\tilde{\chi}_3^0} = |\mu| + \frac{m_Z^2 (\text{sgn}(\mu) - \sin 2\beta)(\mu + M_1 \cos^2 \theta_W + M_2 \sin^2 \theta_W)}{2(\mu + M_1)(\mu + M_2)} + \dots \quad (1.20)$$

$$m_{\tilde{\chi}_4^0} = |\mu| + \frac{m_Z^2 (\text{sgn}(\mu) + \sin 2\beta)(\mu - M_1 \cos^2 \theta_W - M_2 \sin^2 \theta_W)}{2(\mu - M_1)(\mu - M_2)} + \dots \quad (1.21)$$

$$m_{\tilde{\chi}_1^\pm} = M_2 - \frac{m_W^2 (M_2 + \mu \sin 2\beta)}{\mu^2 - M_2^2} + \dots \quad (1.22)$$

$$m_{\tilde{\chi}_2^\pm} = |\mu| + \frac{m_W^2 \text{sgn}(\mu)(\mu + M_2 \sin 2\beta)}{\mu^2 - M_2^2} + \dots \quad (1.23)$$

²²⁴ where $\tan \beta = \langle H_u^0 \rangle / \langle H_d^0 \rangle$.

²²⁵ The two scenarios studied in ref. [12] are the following:

²²⁶ • **Bino NLSP:** $M_1 \sim$ few hundred GeV, $M_2, |\mu| \gg M_1$. All but the lightest
²²⁷ neutralino are effectively inaccessible at the LHC due to their large masses. The
²²⁸ NLSP can always decay to $\gamma + \tilde{G}$, and if it is heavy enough, to $Z + \tilde{G}$ or $H + \tilde{G}$.

²²⁹ • **Wino NLSP:** $M_2 \sim$ few hundred GeV, $M_1, |\mu| \gg M_2$. The lightest neutralino
²³⁰ and the lightest chargino are nearly degenerate in mass, and are the only two
²³¹ particles to play a role at the LHC. The decays described in the previous bullet
²³² point can happen, as well as chargino decays to $W + \tilde{G}$.

²³³ The subject of this thesis is the classic bino NLSP decay $\gamma + \tilde{G}$.

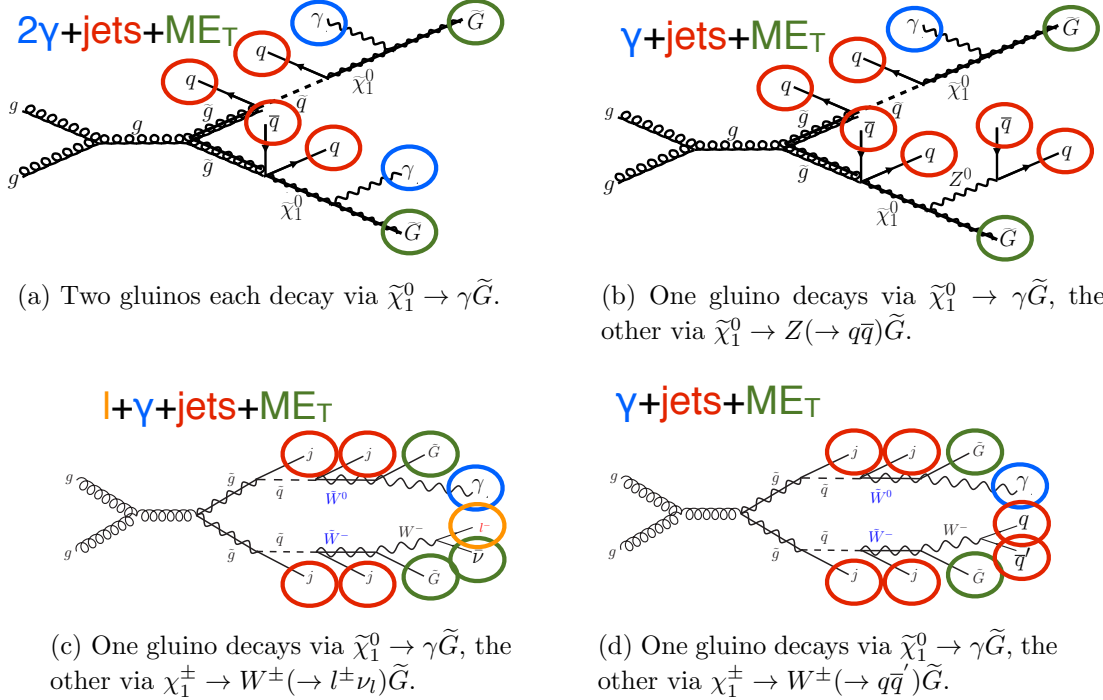


Figure 1.4: Typical LHC signatures of the bino and wino NLSP scenarios.

234 Since strong production of SUSY particles dominates over electroweak production
235 at the LHC due to the enhanced gg parton luminosity over the $q\bar{q}$ parton luminosity,
236 early LHC searches are particularly sensitive to light squarks and gluinos. General
237 gauge mediation makes no a priori restrictions on the mass splitting between the
238 strongly interacting sparticles and the weakly interacting sparticles, so models with
239 light squarks and gluinos are viable. In fact, such models could not be probed as
240 well at the Tevatron⁴ as they are at the LHC due to the aforementioned parton
241 luminosities.

242 Typical LHC signatures of the bino and wino NLSP scenarios are shown in Fig-
243 ure 1.4.

⁴Located on the Fermilab site in Batavia, Illinois, the Tevatron was a proton-antiproton collider operating at 1.96 TeV center-of-mass energy. The Tevatron ran from 1987 to 2011 [13].

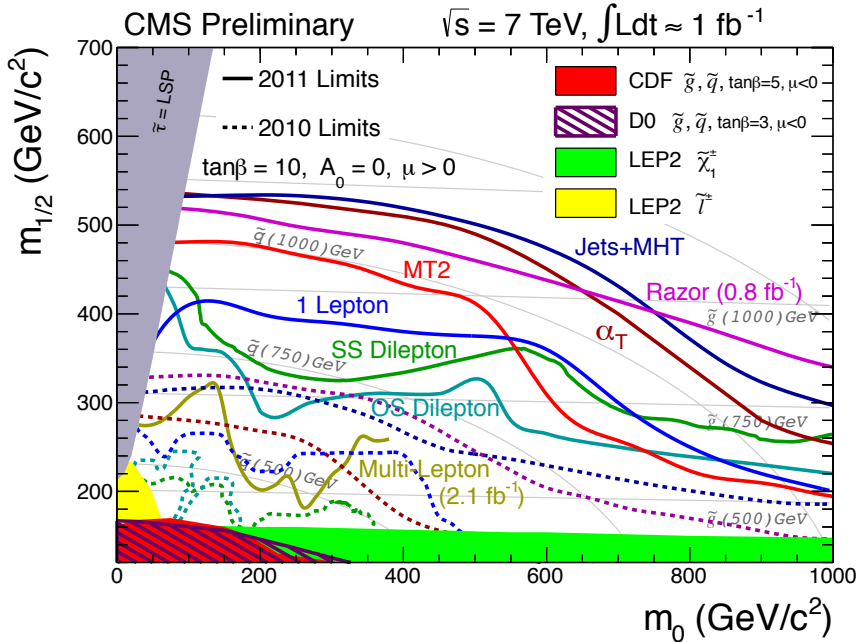


Figure 1.5: CMS limits on mSUGRA with $\tan \beta = 10$. The limits set by individual searches are shown as separate colored lines. Solid lines refer to 2011 searches (i.e. using an integrated luminosity of $\sim 1 \text{ fb}^{-1}$), while dashed lines refer to 2010 searches ($\sim 36 \text{ pb}^{-1}$). Reprinted from ref. [16].

244 1.6 Experimental Status of SUSY

245 Collider searches for evidence of supersymmetry began in earnest in the 1980s [14]
 246 and continue to this day. Most recently, the LHC and Tevatron experiments have set
 247 the strictest limits on a variety of SUSY breaking scenarios, including GMSB and
 248 mSUGRA.

249 Figure 1.5 shows the current limits set by the CMS experiment on the mSUGRA
 250 model (with $\tan \beta = 10$) in the m_0 - $m_{1/2}$ plane. (Note that although the plot is trun-
 251 cated at $m_0 = 1000 \text{ GeV}/c^2$, some searches are sensitive out to $m_0 \sim 2000 \text{ GeV}/c^2$.)
 252 Although the LHC has pushed m_0 above $\sim 1 \text{ TeV}/c^2$ for $m_{1/2}$ up to $\sim 400 \text{ GeV}/c^2$,
 253 casting some doubt onto the theory's prospects for solving the hierarchy problem,
 254 there is still a sizable chunk of mSUGRA parameter space that is not ruled out by
 255 collider experiments. Furthermore, parts of the CMS unexplored regions overlap with
 256 areas allowed by astrophysics experiments [15].

Removed
 CMS
 Moriond
 result

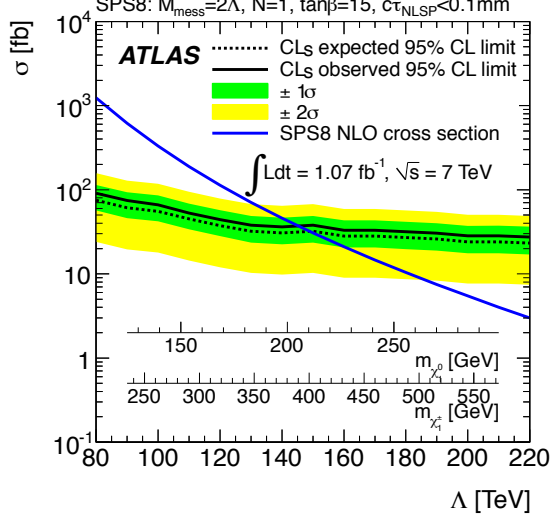


Figure 1.6: ATLAS cross section upper limit on the SPS8 [18] model of mGMSB as a function of SUSY breaking scale Λ , lightest neutralino mass $m_{\tilde{\chi}_1^0}$, or lightest chargino mass $m_{\tilde{\chi}_1^\pm}$. Values of Λ , $m_{\tilde{\chi}_1^0}$, or $m_{\tilde{\chi}_1^\pm}$ below the intersection point between the blue (predicted SPS8 cross section) and black (observed cross section upper limit) curves are excluded. The model parameters listed above the plot are defined in Secs. 1.4 and 1.5, except for τ_{NLSP} , which is the neutralino lifetime. Reprinted from ref. [10].

257 Figure 1.6 shows the most up-to-date limit (using 1 fb^{-1} of integrated luminos-
258 ity collected by the ATLAS experiment [17] at the LHC) on the Snowmass Points
259 and Slopes (SPS) model of mGMSB, dubbed SPS8 [18]. In general, the lifetime of
260 the lightest neutralino in GMSB models can take on any value between hundreds of
261 nanometers to a few kilometers depending on the mass of the lightest neutralino and
262 the SUSY breaking scale [6]. The search published in ref. [10] (from which Figs. 1.6
263 and ?? are culled) considers only *prompt* neutralino variants, i.e. with neutralino life-
264 time short enough that the distance traveled by the neutralino before decay cannot be
265 resolved by the detector. The most recent limits on non-prompt SPS8-style neutralino
266 models were set by the Collider Detector at Fermilab (CDF) collaboration with 570
267 pb^{-1} , and are shown in Figure 1.7 [11].

268 Finally, if the gravitino is to make up some or all of the dark matter, constraints
269 on the form of gauge mediation must come from cosmological considerations and
270 astronomical observations. The gravitino in gauge mediation models is usually very

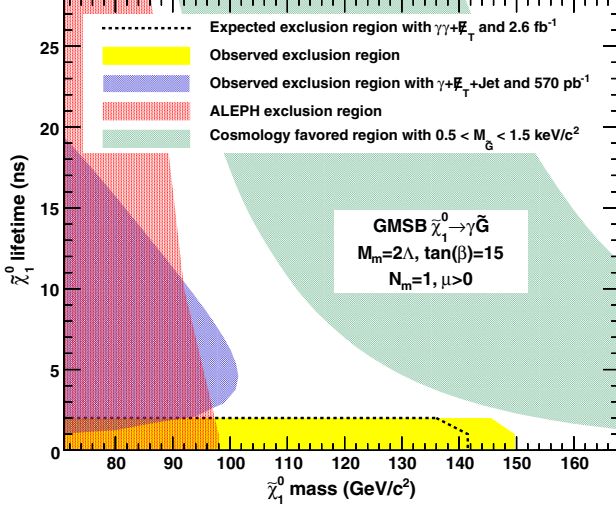


Figure 1.7: CDF exclusion contour in the $\tau_{\tilde{\chi}_1^0}$ - $m_{\tilde{\chi}_1^0}$ plane, where $\tau_{\tilde{\chi}_1^0}$ is the lifetime of the neutralino. Reprinted from ref. [11].

271 light ($\mathcal{O}(\text{eV-MeV})$) because it is proportional to the SUSY breaking scale divided by
 272 the Planck mass, and in GMSB the breaking scale is typically only of order a few
 273 hundred TeV ([6] and Sec. 1.5). A light, highly relativistic dark matter particle might
 274 have been produced, for instance, in the early, radiation-dominated period of the
 275 universe [20]. This *warm dark matter* (WDM) may be responsible for all of the dark
 276 matter needed to account for galactic structure, or it may share the duties with *cold*
 277 *dark matter* (CDM, weakly interacting particles with masses in the GeV range). In
 278 any viable model, the predicted relic density of the dark matter species must match
 279 the observed value of $\Omega h^2 \sim 0.1$ [21]. For many GMSB models, this measurement
 280 constrains the gravitino mass to the keV range [22]. This constraint, however, does
 281 not translate into a very strong bound on the lifetime of the lightest neutralino. Using
 282 the following equation (taken from [22]):

$$\tau_{\tilde{\chi}_1^0} \sim 130 \left(\frac{100 \text{ GeV}}{m_{\tilde{\chi}_1^0}} \right)^5 \left(\frac{\sqrt{\langle F \rangle}}{100 \text{ TeV}} \right)^4 \mu\text{m} \quad (1.24)$$

283 and applying the gravitino mass constraint $\sqrt{\langle F \rangle} \lesssim 3000 \text{ TeV}$ (cf. the first paragraph
 284 of Sec. 1.5 with $m_{\tilde{G}} \sim \text{keV}$) and $m_{\tilde{\chi}_1^0} = 100 \text{ GeV}$, the upper bound on the neutralino

285 lifetime is 100 meters. For $\sqrt{\langle F \rangle} \sim 100$ TeV, the neutralino lifetime is detectable on
286 collider time scales.

287 Recently, a lower bound on the WDM particle mass in either pure warm or mixed
288 warm and cold dark matter scenarios was set using observations of the Lyman- α for-
289 est. For pure WDM, $m_{\text{WDM}} > 8$ keV, while for some mixed WDM-CDM scenarios,
290 $m_{\text{WDM}} > 1.1\text{-}1.5$ keV [20, 23]. These bounds and others have motivated the develop-
291 ment of more complicated gauge mediation models [23]. However, rather than focus
292 on a specific GMSB model, of which there are many, the search detailed here is in-
293 terpreted in a minimally model dependent way. With this approach, the results can
294 be applied to many competing models. The remainder of this thesis is devoted to the
295 experimental details of the search, analysis strategy, and presentation of the results.
296 The work described in this thesis forms the basis for the CMS public result “Search
297 for Supersymmetry in Events with Photons and Missing Energy” [19], published in
298 April 2012.

299 **Chapter 2**

300 **Event Selection**

301 In keeping with the phenomenology described in Sec. 1.5, the candidate GGM events
302 selected in this search consist of two high- E_T photons and a significant momentum
303 imbalance transverse to the beam, indicating the production of an escaping gravitino.
304 This momentum imbalance is usually referred to as *missing transverse energy* and is
305 denoted by the symbol \cancel{E}_T .

306 However, in order to use real CMS data (as opposed to simulation) to derive pre-
307 dictions for the backgrounds to the search, *control samples* distinct from the *candidate*
308 two-photon sample must be collected. These samples consist of different numerical
309 combinations of photons, electrons, and jets, and are explained in more detail in
310 Chapter 3. Since this search is performed in the high- \cancel{E}_T tail of the \cancel{E}_T distribution,
311 where adequate detector simulation is very difficult, it is advantageous to use *data-
312 driven* background estimates, which capture the true detector response, over numbers
313 derived from simulation.

314 In the following sections, the reconstruction of photons, electrons, jets, and \cancel{E}_T
315 is explained. Sec. 2.1 begins with an explanation of the high level reconstruction.
316 It is followed by Sec. 2.2, which describes the triggers used to collect the candidate
317 and control samples. Sec. 2.3 describes event cleaning cuts that are applied to the

³¹⁸ candidate and control samples. Finally, the chapter concludes with a measurement of
³¹⁹ the photon identification efficiency in Sec. 2.4.

³²⁰ 2.1 Object Reconstruction

³²¹ This section describes the *offline* object reconstruction, i.e. the reconstruction of par-
³²² ticle objects from events that have already been triggered and written to permanent
³²³ storage, as opposed to the building of trigger objects explained in Secs. ?? and 2.2.

³²⁴ 2.1.1 Photons

³²⁵ Uncalibrated EB/EE Hits

³²⁶ Photon reconstruction begins with the ADC count value for each of the 10 recorded
³²⁷ time samples per ECAL crystal per trigger. To construct an *uncalibrated hit*, the
³²⁸ gain (1, 6, or 12; see Sec. ??) of each sample is determined and the ADC count
³²⁹ value scaled appropriately. The pedestal is estimated from the average of the first
³³⁰ three samples, which, for a properly timed in hit, should contain no signal. This
³³¹ pedestal value is subtracted from the rest of the samples. Finally, the amplitude of the
³³² pulse is reconstructed using a predetermined weight for each sample [25]. The weights
³³³ correspond to the pulse shape expected from the MGPA and shaping circuit response.
³³⁴ The time of the hit is also reconstructed using the ratios between neighboring time
³³⁵ samples [26]. A typical ECAL channel pulse shape is shown in Figure 2.1.

³³⁶ Calibrated EB/EE Hits

³³⁷ In the next phase of the photon reconstruction, calibrations are applied to the un-
³³⁸ calibrated hits to form *calibrated hits* with energy measured in GeV. Channels are
³³⁹ excluded from seeding calibrated hits if

- ³⁴⁰ • they are excessively noisy,

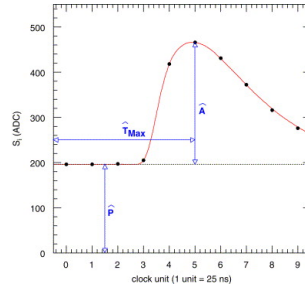


Figure 2.1: Typical ECAL channel pulse shape. \hat{P} is the pedestal value, \hat{A} is the pulse amplitude, and \hat{T}_{\max} is the hit time. The red line is the assumed pulse shape from which the weights are derived. Reprinted from ref. [25].

- 341 • they are stuck in fixed gain (i.e. the MGPA gain does not change properly to
- 342 avoid saturation),
- 343 • they are totally dead,
- 344 • they have one or more neighboring dead channels, or
- 345 • they do not have good trigger primitives (i.e. trigger primitive is missing, satu-
- 346 rated, or *spike-like*).

Added

347 *ECAL spikes* are hits in which low energy protons and heavy ions from jets ionize this
 348 in the sensitive volume of the EB APD, causing the APD to register a fake large- para-
 349 amplitude hit. Because they are not the result of a real electromagnetic shower, spikes graph
 350 tend to be isolated. They may also appear to arrive early or late with respect to the and the
 351 nominal bunch crossing. Most spikes are reconstructed with a hit time ~ 10 ns earlier next
 352 than real EM hits because unlike real hits, whose pulse shapes include the time about
 353 constant associated with crystal scintillation, the reconstructed spikes only involve spikes
 354 the rise time of the electronics. There also is a long tail of late arriving spikes due to
 355 slow neutrons from jets [27].

356 Because of their particular timing and topological characteristics, cuts have been
 357 developed to effectively identify and reject spike-like hits. This analysis utilizes both
 358 the “Swiss cross” cut $1 - E_4/E_1 > 0.95$, where E_1 is the energy of the spike candidate

359 crystal and E_4 is the sum of the energies in the four crystals whose edges are parallel to
 360 the four edges of the spike candidate crystal, and a timing cut $t \geq 3$ ns, to flag spikes.
 361 More information about these cuts can be found in ref. [27]. A simpler algorithm
 362 using the fine grain veto bit of the L1 TPG is used to reject spikes at the trigger level
 363 **[insert citation]**.

364 In addition to the trigger primitives, no uncalibrated hits that are spike-like are eli-
 365 gible for calibration. The calibrations applied are crystal transparency loss corrections
 366 measured continuously by the laser/LED system, energy intercalibrations (relative en-
 367 ergy calibration between crystals), absolute scale calibrations between ADC counts
 368 and GeV,¹ and time intercalibrations (relative time calibration between crystals).

369 The ECAL crystals were pre-calibrated before installation in CMS using labora-
 370 tory light yield and photodetector gain measurements [29]. In addition, some EB and
 371 EE crystals were intercalibrated using test beams [30], and all EB crystals were inter-
 372 calibrated with cosmic ray muons [31]. EE precalibrations were validated with LHC
 373 *splash events* in 2009 [31, 32], in which the beam was dumped onto a collimator ap-
 374 proximately 150 meters upstream of CMS, causing a spray of muons to enter CMS at
 375 one endcap and exit at the other. Splash events were also used to derive time intercal-
 376 ibration constants. Before colliding beam operations commenced, the intercalibration
 377 precision was estimated to be 0.5%-2.2% in EB and 1%-5% in EE [33].

378 Three calibration methods were employed once colliding beam operations began:

- 379 • ϕ symmetry relative calibration between crystals, exploiting the azimuthal sym-
 metry of CMS
- 381 • π^0 and η relative calibration between crystals, using the diphoton decays of
 these particles

¹The ADC-GeV scale factors (one for EB and one for EE) are defined such that the sum of fully calibrated and scaled hits in a particular 5×5 cluster of crystals (plus the associated energy deposited in ES) is 50 GeV for a 50 GeV incident unconverted photon [28].

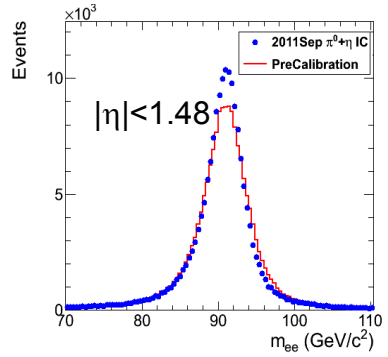


Figure 2.2: Z peak reconstructed using pre-LHC calibration constants (red) or September 2011 π^0/η -derived intercalibration constants (blue). Reprinted from ref. [34].

383 • E/p absolute calibration, comparing the momentum measured in the tracker p
 384 to the energy measured in the ECAL E of a sample of electrons from Z decay

385 By September 2011, the intercalibration precision in EB was measured to be be-
 386 tween 0.3% and 1.1% using the π^0/η method [34]. Figure 2.2 shows the improvement
 387 in Z reconstruction from pre-LHC calibration constants to the latest π^0/η -derived
 388 constants.

389 **Calibrated ES Hits**

Added

390 ES calibrated hits are formed from the three samples read out per sensor. Just as in the paren-
 391 case of EB/EE crystals, ES uncalibrated hits gain-adjusted, pedestal-subtracted, and thetical
 392 reconstructed using weights. To make a calibrated ES hit, intercalibration constants, remark
 393 angle correction constants (for the non-uniformity of sensor angle with respect to the
 394 vertical across ES), and a MIP-GeV absolute scale factor are applied.

395 **Clustering**

396 After calibrated ECAL hits are formed, they must be clustered into shapes that
 397 represent the energy deposit from a single particle. *Basic clusters* are formed around
 398 seed hits, defined as a hit that

- 399 • has calibrated $E_T > 1(0.18)$ GeV in EB(EE),
- 400 • does not originate from a dead channel or one with faulty hardware,
- 401 • is not poorly calibrated,
- 402 • was reconstructed with the standard algorithm (i.e. not a special recovery algo-
- 403 rithm for channels with subpar data integrity),
- 404 • is not saturated,
- 405 • is not spike-like, and
- 406 • is in time (EB).

407 EB basic clusters are formed around the seeds via the *hybrid* algorithm, while EE basic
 408 clusters are formed with the `multi5x5` algorithm [35]. In addition to non-radiating
 409 electrons and unconverted photons, both algorithms are designed to also recover all of
 410 the energy associated with electron bremsstrahlung deposits and photon conversions.
 411 The geometry of the CMS magnetic field means that bremsstrahlung and conversions
 412 will tend to spread the shower out in ϕ , not η . Both algorithms work by forming
 413 basic clusters around seeds, then combining the basic clusters into *superclusters* (SC)
 414 by searching in a window extended in the ϕ direction for all basic clusters consistent
 415 with bremsstrahlung radiation from the primary electron, or with a photon conversion.
 416 Figure 2.3 illustrates the hybrid algorithm in EB. In EE, the energy deposited in ES
 417 must also be added into the total clustered energy sum.

418 Figure 2.4 shows the effect of superclustering on $Z \rightarrow ee$ reconstruction.

419 **Supercluster Corrections**

420 The total clustered ECAL energy is defined as

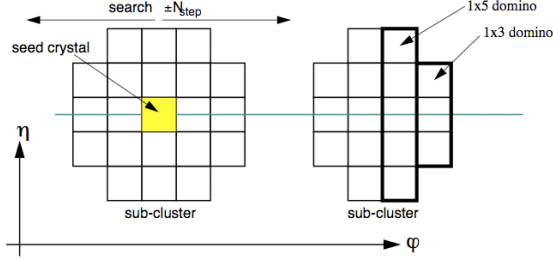


Figure 2.3: Hybrid algorithm in EB. The shower extent is essentially constant in η , but spreads out in ϕ as the two sub-clusters (or basic clusters) are grouped into the same supercluster. Reprinted from ref. [35].

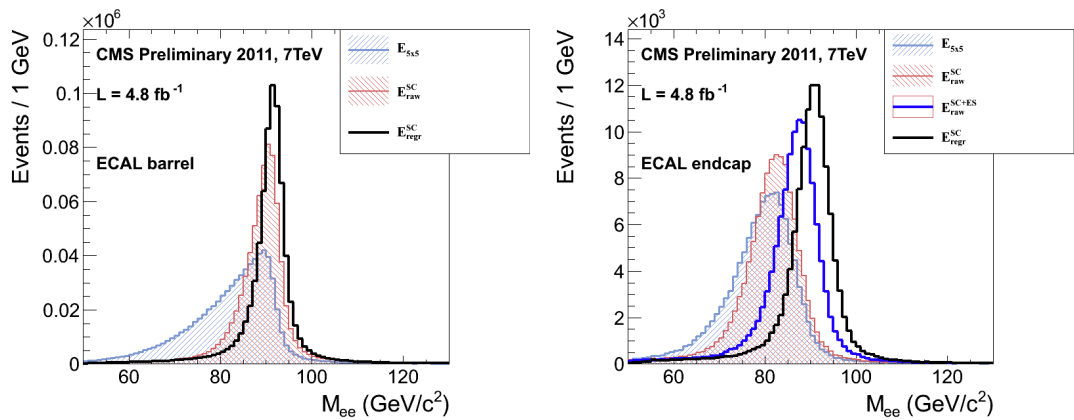


Figure 2.4: Z peak reconstructed in the dielectron channel for different kinds of clustering. The left plot is for EB and the right plot for EE. The constituent hits were calibrated with the best available intercalibrations and laser calibrations as of December 2011. The light blue histogram shows the reconstruction using a 5×5 energy sum, the red histogram shows the reconstruction using the SC energy for crystals only (the dark blue histogram on the right-hand side adds in the energy from ES), and the black histogram shows the reconstruction after the SCs are corrected using a multivariate method [?]. Reprinted from Fig. 30 of ref. [?].

$$E = F \times \sum_{i=1}^{n_{\text{crystal}}} G \times c_i \times A_i \quad (2.1)$$

421 where G is the ADC-GeV or MIP-GeV scale factor, c_i are the intercalibration con-
 422 stants, A_i is the uncalibrated hit amplitude in ADC counts, and F is a SC correction
 423 factor. G and c_i were explained in Sec. 2.1.1. F is a product of three factors for hybrid
 424 SCs (two for multi5x5 SCs) [35]:

- 425 1. $C_{\text{EB}}(\eta)$, which compensates for lateral energy leakage due to the crystal off-
 426 pointing in EB. These corrections are taken from MC simulation [35] and were
 427 confirmed in test beams [30].
- 428 2. $f(\text{brem})$, which corrects for biases in the clustering algorithms for showers char-
 429 acterized by differing amounts of bremsstrahlung. These corrections are taken
 430 from MC simulation [35].
- 431 3. Residual correction $f(E_T, \eta)$, due to the variation in η of detector material
 432 traversed by a primary electron or photon, and to any residual E_T dependence
 433 of the reconstruction. These corrections are determined from MC and validated
 434 on $Z \rightarrow ee$ data samples [36].

Changed

435 As a benchmark of ECAL calibration performance, the extra energy smearing in
 436 MC needed to achieve data/MC agreement in the Z width was between $\sim 0.9\%$ (in
 437 the central part of EB for electrons with little bremsstrahlung) and $\sim 3.3\%$ (in the
 438 outer part of EE for heavily radiating electrons) [37].

439 From Supercluster to Photon

440 The CMS photon object is any SC with $E_T > 10$ GeV and $H/E < 0.5$, unless the SC
 441 $E_T > 100$ GeV, in which case the H/E requirement is dropped. H/E is defined as the

442 ratio of energy in the HCAL in a 0.15 cone around the SC centroid, directly behind
 443 the SC, to the SC energy. SCs with $R9 > 0.94(0.95)$ in EB(EE), where $R9$ is defined
 444 as the ratio of the energy in the central 3×3 cluster of crystals divided by the SC
 445 energy $E_{3 \times 3}/E_{\text{SC}}$, are the best calibrated and most accurate type of electromagnetic
 446 shower. Therefore, for these objects, the photon energy is defined as the energy sum
 447 of the fully calibrated hits in the central 5×5 cluster around the seed (with $C_{\text{EB}}(\eta)$
 448 applied for EB photons). For all other SCs, the photon energy is equal to the fully
 449 corrected SC energy (cf. Sec. 2.1.1).

Reorganized

450 In this search, candidate photons and *fake photons* (f , “fakes”) are further selected next 3
 451 according to the criteria listed in Table 2.1. Fakes are used in the determination of para-
 452 the QCD background, as explained in Chapter 3. graphs;

edited
Ta-ble 2.1
caption

Table 2.1: Selection criteria for photons and fakes. “Pixel seed,” I_{comb} , and $\sigma_{i\eta i\eta}$ are defined in the text.

Variable	Cut (γ)	Cut (f)
SC $ \eta $	< 1.4442	< 1.4442
H/E	< 0.05	< 0.05
$R9$	< 1	< 1
Has pixel seed	No	No
$I_{\text{comb}}, \sigma_{i\eta i\eta}$	$< 6 \text{ GeV} \&\& < 0.011$	$(\geq 6 \&\& < 20 \text{ GeV}) \parallel \geq 0.011$

Updated
effective
area

453 I_{comb} is defined as

$$I_{\text{comb}} = I_{\text{ECAL}} - 0.093\rho + I_{\text{HCAL}} - 0.0281\rho + I_{\text{track}} \quad (2.2)$$

454 where I_{ECAL} , I_{HCAL} , and I_{track} are E_T sums in the annular regions defined in Figure 2.5
 455 and ρ is the average pileup energy density in the calorimeters (per unit $\eta \cdot \phi$) as
 456 measured with the Fastjet algorithm [38, 39]. Note that the ECAL and track isolation
 457 veto strips at constant η ensure that the isolation cuts are similarly efficient for
 458 converted photons, radiating electrons, and unconverted photons.

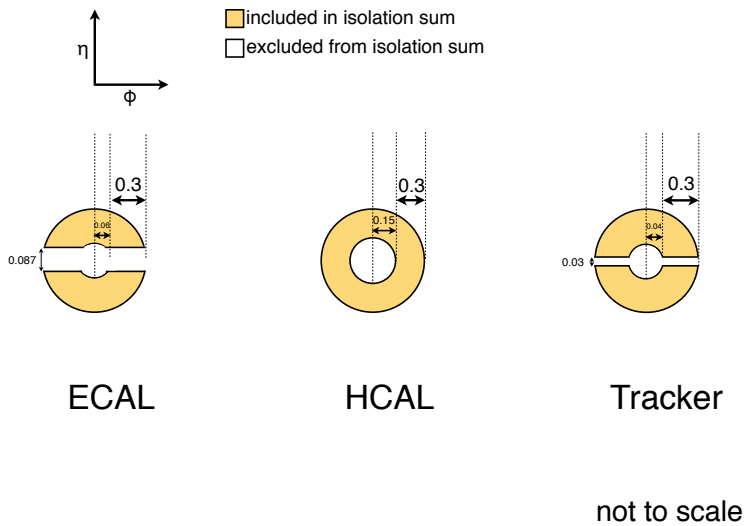


Figure 2.5: ECAL, HCAL, and track Isolation cones.

459 $\sigma_{i\eta i\eta}$ is the log energy weighted extent of the shower in η and is defined as Added

$$\sigma_{i\eta i\eta} = \frac{\sum_{i=1}^{25} w_i (\eta_i - \bar{\eta})^2}{\sum_{i=1}^{25} w_i} \quad (2.3) \quad \begin{matrix} \text{defini-} \\ \text{tion} \end{matrix}$$

where the sums run over the 5×5 matrix of crystals surrounding the seed, $w_i = \max(0, 4.7 + \ln(E_i/E))$, E_i is the energy of the i^{th} crystal, E is the total energy in the 25 crystals, η_i is the offset in η of the i^{th} crystal from the seed, and $\bar{\eta}$ is the weighted average η of the 25 crystals (using the w_i as weights) [40].

Figure 2.6 shows the ρ distribution for a sample of two-photon events, with at least one 40 GeV and one 25 GeV photon, passing the selection requirements in Table 2.1 and the trigger requirements in Table 2.3. This sample represents the full 2011 dataset of 4.7 fb^{-1} . Since the average ρ is $\sim 7.5 \text{ GeV}$, and there is a long tail above this average value, it is necessary to subtract pileup energy from the ECAL and HCAL isolation cones to recover otherwise clean photons in events with large pileup. The ECAL and HCAL *effective areas* of 0.093 and 0.0281, respectively, are

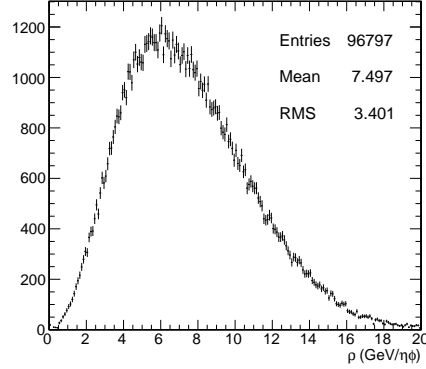


Figure 2.6: ρ distribution for a sample of two-photon events, with at least one 40 GeV and one 25 GeV photon, passing the selection requirements in Table 2.1 and the trigger requirements in Table 2.3. This sample covers the full 2011 dataset of 4.7 fb^{-1} .

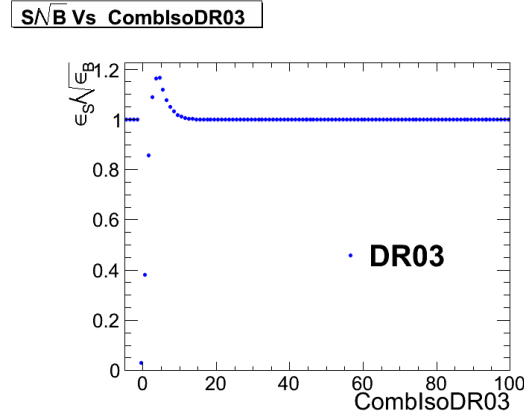


Figure 2.7: S/\sqrt{B} (S and B defined in the text) vs. combined isolation. Reprinted from Fig. 7 of ref. [41].

471 calculated by fitting the average ECAL or HCAL isolation energy vs. ρ in a sample
 472 of $Z \rightarrow ee$ events to a straight line. The slope of the line—which has the units of $\eta \cdot \phi$,
 473 or area—is the effective area.

New

474 The cut on combined isolation of 6 GeV (Table 2.1) is the result of an S/\sqrt{B}
 475 optimization procedure [41]. S is a sample of photons in simulated GGM events that
 476 are products of neutralino decay, while B is a sample of photons matched to generated
 477 hadronic jets in simulated QCD events. Figure 2.7 shows the value of S/\sqrt{B} vs.
 478 combined isolation, in particular the pronounced peak around 6 GeV.

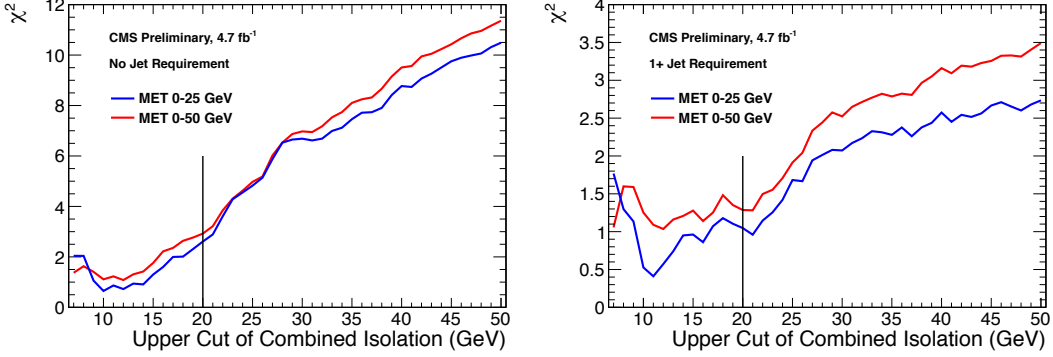


Figure 2.8: Neyman’s χ^2 between the ff and $\gamma\gamma$ \cancel{E}_T distributions, truncated at either 25 (red) or 50 (blue) GeV, vs. upper bound on fake combined isolation. The left plot includes all events; the right plot is for events with ≥ 1 jet defined as in Table 2.2, but with the ΔR cleaning criteria applied to the two primary EM objects and all additional electrons, photons, and fake photons. The full reweighting and normalization procedure is employed in the \cancel{E}_T calculation (see Sec. 3.1). Error bars include statistical, reweighting, and normalization error (see Sec. 3.3). Reprinted from Fig. 9 of ref. [41].

479 The upper bound on fake photon combined isolation guarantees that poorly iso-
 480 lated dijet events, with \cancel{E}_T resolution dissimilar to the candidate diphoton events,
 481 do not enter the ff sample. The exact value of 20 GeV (cf. Table 2.1) arises from
 482 a low- \cancel{E}_T $ff/\gamma\gamma$ χ^2 optimization procedure [41]. Figure 2.8 shows the value of the
 483 Neyman’s χ^2 between the ff and $\gamma\gamma$ \cancel{E}_T distributions, truncated at either 25 or 50
 484 GeV, vs. upper bound on fake combined isolation. As shown in the figure, 20 GeV
 485 very nearly minimizes the χ^2 , while also being large enough that a sufficient number
 486 of ff events may be collected.

487 Finally, a “pixel seed” is defined as a hit in the pixel detector consistent with a
 488 track extrapolated from the position of the ECAL SC back to the primary vertex.
 489 Real photons, having no charge and therefore no bending in the magnetic field, should
 490 not have a pixel seed.

491 2.1.2 Electrons

492 Electrons are reconstructed identically to photons, except that in the electron case
493 the presence of a pixel seed is enforced, rather than vetoed.² Photons and electrons
494 are defined by very similar criteria so that $Z \rightarrow ee$ events can be used to model
495 the QCD background in the two-photon sample without introducing any bias in the
496 electron energy measurement (cf. Sec. 3.1).

497 2.1.3 Jets and Missing Transverse Energy

498 Particle Flow

499 In this analysis, jets and \cancel{E}_T are formed from *particle flow* (PF) candidates. The parti-
500 cle flow algorithm [45, 46] uses information from all CMS subdetectors to reconstruct
501 as accurately as possible the positions and momenta of all visible jet constituents,
502 exploiting the fine granularity of the tracker and ECAL to achieve a greatly improved
503 momentum resolution over calorimeter-only jets [47]. The PF algorithm is summa-
504 rized below [48].

505 1. Reconstruct the fundamental detector objects via iterative procedures

- 506 • Tracks in the inner silicon layers
 - 507 – High efficiency and low fake rate for charged hadrons in jets
 - 508 – Relaxed primary vertex constraint allows photon conversions, parti-
509 cles originating from nuclear interactions in the silicon, and long-lived
510 particles to be reconstructed
- 511 • Calorimeter clusters
- 512 • Muon tracks in the outer muon layers

513 ²In many CMS analyses, electrons are reconstructed very differently from photons. In particular,
514 a special tracking algorithm [44] is used to best follow a radiating electron. However, in this analysis,
515 the electron tracking is not used.

513 2. Create a “block” of linked fundamental objects

- 514 • Link silicon tracks to calorimeter clusters via $\Delta R_{\text{track-cluster}}$ (account for
515 electron bremsstrahlung)
- 516 • Link clusters in one calorimeter layer to clusters in a separate layer via
517 $\Delta R_{\text{cluster-cluster}}$
- 518 • Link silicon tracks to muon tracks via global track χ^2

519 3. ID the particles in the block

- 520 • If global (silicon + muon layers) muon p_T is compatible with silicon track
521 p_T , ID as a muon and remove corresponding tracks from block
- 522 • ID electron tracks via special algorithm and removed all corresponding
523 tracks and cluster from block
- 524 • Remove fake tracks from the block Fixed
- 525 • Remove excess track-cluster links via $\Delta R_{\text{track-cluster}}$ minimization (but al- typo
526 low multiple tracks to be associated to one cluster)
- 527 • If the cluster energy is significantly larger then the energy of the linked
528 track, ID as a PF photon or PF neutral hadron and remove corresponding
529 clusters from the block
- 530 • If the cluster is not linked to a track, ID as a PF photon or PF neutral
531 hadron and remove corresponding clusters from the block
- 532 • Remaining track-cluster links are PF charged hadrons

533 **Jets**

534 PF candidates are clustered into jets by means of the anti- k_T algorithm with $R = 0.5$
535 [49]. In this algorithm, all possible pairs of PF candidates i, j are looped over, and
536 the momenta of the pair that minimize the distance variable

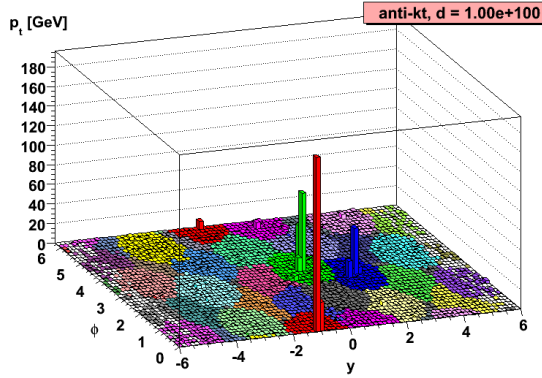


Figure 2.9: Example event display showing jets clustered via the anti- k_T algorithm. y is pseudorapidity. Reprinted from slide 85 of ref. [50].

$$d_{ij} = \frac{\Delta R_{ij}^2}{R^2 \max(k_{Ti}^2, k_{Tj}^2)} \quad (2.4)$$

537 are combined, where k_{Ti} is the transverse momentum of “combined” PF candidate i .
 538 The constituent PF candidates are clustered together. The process is repeated until
 539 $d_{ij} > 1/k_{Ti}^2$ for all pairs of clustered PF momenta [50]. An illustration is given in Fig-
 540 ure 2.9. The anti- k_T algorithm is infrared and collinear safe, leading to well-behaved Added
 541 theoretical predictions and ease of comparison between data and MC simulation. It refer-
 542 also tends to form circular jets, making it easy for experimental effects such as ex- ence to
 543 pected out-of-cone energy and fiducial acceptance to be measured or simulated. For Fig. 2.9
 544 these reasons, the anti- k_T jet clustering algorithm was chosen for this analysis.

545 Once jets are clustered, they must be corrected for biases in the energy mea-
 546 surement due to non-compensation [51], invisible energy (lost to overcoming nuclear
 547 binding energy, in neutrinos, or in unclustered muons, for example) [51], detector
 548 geometry and cracks [52], zero suppression and trigger inefficiencies [53], pileup, and
 549 effects of the clustering algorithm [52]. Four multiplicative correction factors are ap-
 550 plied to the raw jet four-momentum p_μ^{raw} [47]:

- 551 • $C_{\text{offset}}(p_T^{\text{raw}})$, which accounts for extra energy due to noise, pileup, and the un-

552 derlying event;

- 553 • $C_{\text{MC}}(C_{\text{offset}}p_T^{\text{raw}}, \eta)$, which is derived from MC and accounts for most of the p_T
 554 and η dependence;
- 555 • $C_{\text{rel}}(\eta)$, which accounts for the remaining differences in uniformity over the
 556 entire calorimeter between data and MC; and
- 557 • $C_{\text{abs}}(C_{\text{rel}}C_{\text{MC}}C_{\text{offset}}p_T^{\text{raw}})$, which accounts for the remaining differences in linear-
 558 ity over the full p_T range between data and MC.

559 Figure 2.10 shows the total jet energy correction factor $C_{\text{offset}}C_{\text{MC}}C_{\text{rel}}C_{\text{abs}}$ vs. η
 560 for jets reconstructed with the anti- k_T algorithm, $R = 0.5$. The PF jet corrections
 561 are more uniform across η than those of CALO jets (composed of simple calorimeter
 562 towers) or JPT jets (Jet Plus Tracks; composed of calorimeter energies replaced,
 563 where possible, with matching track p_T) [54]. In addition, for p_T in the range 30-200
 564 GeV and $|\eta|$ up to 2.0, the PF jet energy correction uncertainty is lower than that of
 565 the other two types of jets, and never exceeds $\sim 3\%$ [47]. The superior performance
 566 of PF jets motivates their use in this search.

567 In this analysis, candidate and QCD control events are binned by number of jets
 568 satisfying the criteria in Table 2.2.

569 Missing Transverse Energy

570 To be consistent with the jet reconstruction, \cancel{E}_T in this analysis is also reconstructed
 571 from PF candidates. Raw \cancel{E}_T is defined as

$$\cancel{E}_{T\text{raw}} = \left| - \sum_{i=1}^{n_{\text{PF}}} \vec{p}_{Ti} \right| \quad (2.5)$$

Table 2.2: Definition of HB/HE hadronic jets.

Variable	Cut
Algorithm	L1FastL2L3Residual corrected PF
p_T	$> 30 \text{ GeV}$
$ \eta $	< 2.6
Neutral hadronic energy fraction	< 0.99
Neutral electromagnetic energy fraction	< 0.99
Number of constituents	> 1
Charged hadronic energy	$> 0.0 \text{ GeV}$ if $ \eta < 2.4$
Number of charged hadrons	> 0 if $ \eta < 2.4$
Charged electromagnetic energy fraction	< 0.99 if $ \eta < 2.4$
ΔR to nearest PF electron ^a , muon ^b , or one of the two primary EM objects	> 0.5

^aA PF electron is defined as an electron reconstructed with the PF algorithm [42] with $p_T > 15 \text{ GeV}$, $|\eta| < 2.6$, and $(I_{\text{charged}} + I_{\text{photon}} + I_{\text{neutral}})/p_T < 0.2$, where $I_{\text{charged}}(I_{\text{photon}})(I_{\text{neutral}})$ is the sum of PF charged hadron(PF photon)(PF neutral hadron) momenta in a $\Delta R = 0.4$ cone around the PF electron.

^bMuons are reconstructed [43] from a combination of muon station and inner tracker hits. Here, a muon must have track $\chi^2 < 10$, at least one good muon station hit, inner track transverse impact parameter $< 0.02 \text{ cm}$, inner track longitudinal impact parameter $< 0.5 \text{ cm}$, $p_T > 15 \text{ GeV}$, $|\eta| < 2.6$, and $(I_{\text{ECAL}} + I_{\text{HCAL}} + I_{\text{track}})/p_T < 0.2$, where $I_{\text{ECAL}}(I_{\text{HCAL}})(I_{\text{track}})$ is the sum of ECAL(HCAL)(track) momenta in a $\Delta R = 0.3$ cone around the muon.

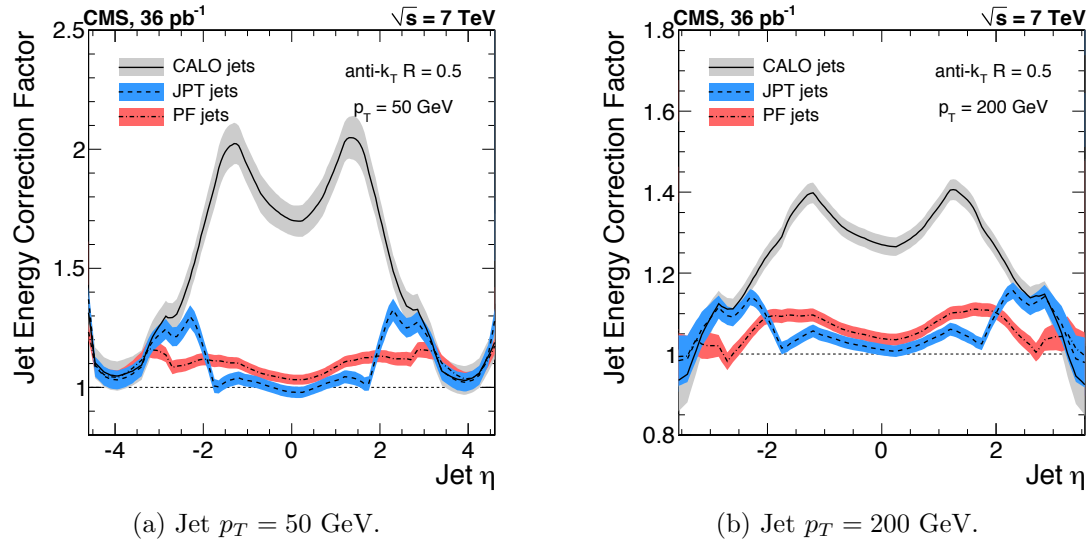


Figure 2.10: Total jet energy correction factor $C_{\text{offset}}C_{\text{MC}}C_{\text{rel}}C_{\text{abs}}$ vs. η , including uncertainty band, for jets reconstructed with the anti- k_T algorithm, $R = 0.5$. Reprinted from Fig. 26 of ref. [47].

where n_{PF} is the number of PF candidates in the event. $\cancel{E}_{T\text{raw}}$ may be corrected for the same effects that necessitate jet corrections, since $\cancel{E}_{T\text{raw}}$ is usually the result of jet mis-measurement (except, of course, in electroweak physics processes that include an energetic neutrino, or SUSY production). CMS *Type-I* \cancel{E}_T corrections simply involve replacing the PF jets with their corrected energies (cf. Sec 2.1.3) and recalculating \cancel{E}_T . Only jets with electromagnetic fraction (EMF) below 90% and $p_T > 20$ GeV are replaced. This ensures that very electromagnetic jets (as well as isolated leptons, which also receive no correction), which consist chiefly of neutral pions and are measured accurately by the ECAL, do not receive a correction derived for jets with a large fraction of their energy in charged hadrons. In addition, the p_T cut guarantees that jet corrections are only applied where they are known to within a few percent. For this search, the level of agreement between the SM background estimate and the two-photon search sample in a low- \cancel{E}_T control region is the same regardless of whether the \cancel{E}_T is corrected or not, so for simplicity the Type-I \cancel{E}_T corrections are not used (see Sec. ??).

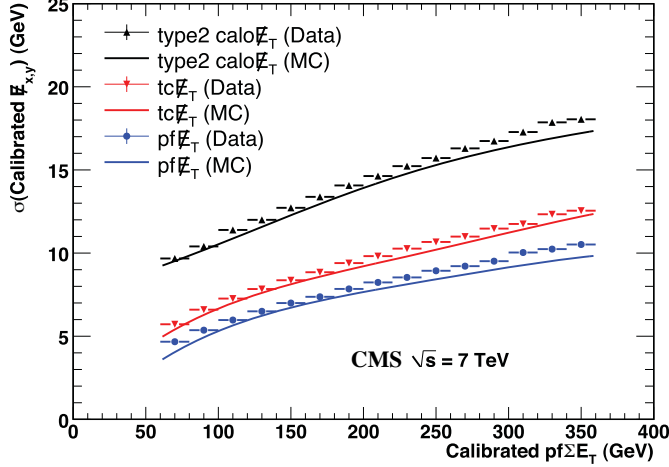


Figure 2.11: σ of a Gaussian fit to the x- and y-components of calibrated E_T vs. the calibrated PF E_T sum in a sample of events containing at least two jets with $p_T > 25$ GeV. σ is calibrated such that the E_T scale is equal for all three algorithms. PF $\sum E_T$ is corrected, on average, to the particle level using a Pythia v8 simulation [55]. The blue markers (data) and line (MC) refer to PF jets. Reprinted from Fig. 13 of ref. [53].

587 Figure 2.11 shows the σ of a Gaussian fit to the x- and y-components of calibrated
 588 E_T vs. the calibrated PF E_T sum in a sample of events containing at least two jets
 589 with $p_T > 25$ GeV. Again, PF E_T outperforms E_T constructed of calorimeter towers
 590 or track-corrected calorimeter deposits.

591 2.2 HLT

592 From the objects described in Sec. 2.1, four samples of events are formed:

- 593 • $\gamma\gamma$ candidate sample, in which the two highest E_T objects are photons,
- 594 • $e\gamma$ control sample, in which the two highest E_T objects are one electron and
 one photon,
- 596 • ee control sample, in which the two highest E_T objects are electrons, and
- 597 • ff control sample, in which the two highest E_T objects are fakes.

598 In all samples, the leading EM object is required to have $E_T > 40$ GeV, while the
 599 trailing EM object is required to have $E_T > 25$ GeV. The high level triggers used to
 600 select the four samples, by run range, are listed in Table 2.3. No trigger is prescaled.

Table 2.3: HLT paths triggered by the $\gamma\gamma$, $e\gamma$, ee , and ff samples, by run range. No triggers are prescaled.

Run range	$\gamma\gamma$	$e\gamma$	ee	ff
160404-163261	Photon26_ IsoVL_ Photon18	Photon26_ IsoVL_ Photon18	Photon26_ IsoVL_ Photon18	Photon26_ IsoVL_ Photon18
161216-166967	Photon36_ CaloIdL_ Photon22_ CaloIdL	Photon36_ CaloIdL_ Photon22_ CaloIdL	Photon36_ CaloIdL_ Photon22_ CaloIdL	Photon36_ CaloIdL_ Photon22_ CaloIdL
166347-180252	Photon36_ CaloIdL_ IsoVL_ Photon22_ CaloIdL_ IsoVL	Photon36_ CaloIdL_ IsoVL_ Photon22_ CaloIdL_ IsoVL	Photon36_ CaloIdL_ IsoVL_ Photon22_ R9Id	Photon36_ CaloIdL_ IsoVL_ Photon22_ R9Id
				Photon36_ R9Id_ Photon22_ CaloIdL_ IsoVL
				Photon36_ R9Id_ Photon22_ R9Id

601 Each piece of the HLT path name is defined as follows.

602 • Photon: Energy deposit in the ECAL that fired an L1 trigger (cf. Sec. ??). For

603 **Photon26_IsoVL_Photon18**, the L1 seed E_T threshold is 12 GeV, while for all **Switched**
 604 other triggers in Table 2.3 it is 20 GeV (cf. Sec. ??). **HLT**
 605 • Integer following the word **Photon**: E_T threshold in GeV for offline reconstructed
 606 photon, using the full photon reconstruction of Sec. 2.1.1 minus the laser cali-
 607 brations and assuming the primary vertex at (0, 0, 0). **path**
 608 • **CaloIdL**: For EB photons, $H/E < 0.15$ and $\sigma_{inj} < 0.014$. **names**
 609 • **IsoVL**: $I_{ECAL} < 0.012E_T + 6$ GeV, $I_{HCAL} < 0.005E_T + 4$ GeV, and $I_{track} <$
 610 $0.002E_T + 4$ GeV. **to ver-**
 611 • **R9Id**: $R9 > 0.8$. **batim**
 612 In addition, the versions of **HLT_Photon26_IsoVL_Photon18** and **font and**
 613 **Photon36_CaloIdL_Photon22_CaloIdL** that were active during runs 160404-163268 **added**
 614 included a cut $E_{max}/E_{5\times5} < 0.98$ for spike rejection. E_{max} is the energy in the highest **refer-**
 615 energy crystal of the EM cluster and $E_{5\times5}$ is the energy in the 5×5 crystal matrix **ence**
 616 around the seed crystal. For runs after 163268, Swiss cross spike rejection of individual **to L1**
 617 crystals from HLT quantities was performed (cf. Sec. 2.1.1). All information about the **section**
 618 evolution of the CMS HLT settings can be found in the HLT configuration browser **Switched**
 619 at <http://j2eeps.cern.ch/cms-project-confdb-hltdev/browser/>. **HLT**
 620 As an example of the naming convention just described, the HLT path **path**
 621 **Photon36_CaloIdL_IsoVL_Photon22_R9Id** is fired if one photon is found with $E_T >$
 622 36 GeV passing the **CaloIdL** and **IsoVL** requirements, and another is found with **names**
 623 $E_T > 22$ GeV passing the **R9Id** requirement. **to ver-**
 624 For the offline E_T cuts described in this section, the triggers are $> 99\%$ efficient, **batim**
 625 as shown in Figure 2.12 [41]. The efficiencies are measured with respect to triggers **font**
 626 with lower E_T thresholds. **Added**
 627 **HLT efficiency discussion**

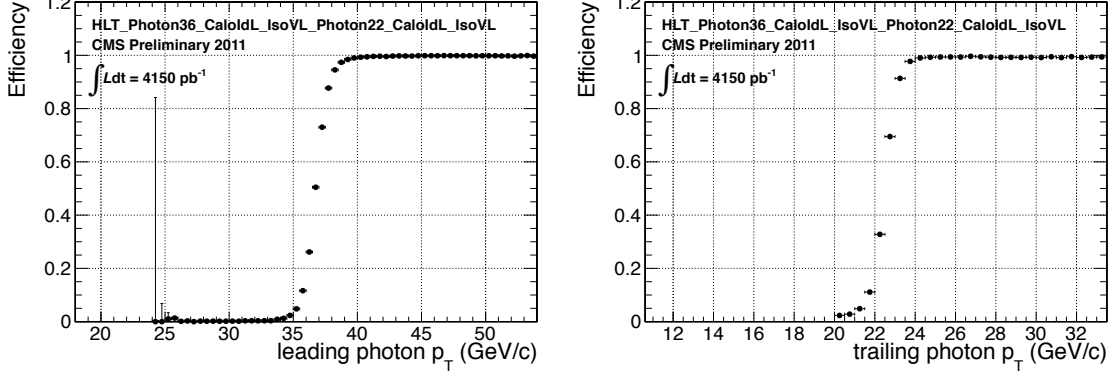


Figure 2.12: Efficiency of HLT_Photon36_CaloIdL_IsoVL_Photon22_CaloIdL_IsoVL for offline selected leading photon (left) and trailing photon (right) vs. photon p_T . Reprinted from Fig. 2 of ref. [41].

627 2.3 Event Quality

628 To suppress instrumental backgrounds, a set of event quality cuts are applied to the
 629 $\gamma\gamma$, $e\gamma$, ee , and ff samples. First, all events are required to pass a good run selec-
 630 tion, as determined by the CMS Physics Validation Team (<https://twiki.cern.ch/twiki/bin/view/CMS/PVTMain>, CERN computing ID needed). The good run selec-
 631 tion excludes luminosity sections during which a sufficient part of the CMS detector
 632 was unpowered or malfunctioning. Such conditions could occur if, for example, a high
 633 voltage supply trips off in the middle of a run, or a DAQ error corrupts data quality
 634 but is not spotted until after the data have been collected. The severity of a detec-
 635 tor problem is judged by its effect on a wide range of analyses and reconstruction
 636 algorithms. Of the $\sim 5 \text{ fb}^{-1}$ of integrated luminosity delivered by the LHC in 2011,
 637 4.68 fb^{-1} passed the good run selection. This analysis is performed on the entire 2011
 638 certified dataset.

640 Second, all events must contain at least one good interaction vertex. The criteria
 641 for a good vertex are:

- 642 • $\chi^2 \neq 0 \parallel \text{ndof} \neq 0 \parallel N_{\text{tracks}} \neq 0$, where χ^2 and ndof are calculated for the track
 643 fit to the vertex, and N_{tracks} is the number of tracks in the vertex fit

- 644 • $\text{ndof} > 4$
- 645 • $|z| < 24 \text{ cm}$, where z is the z -coordinate of the vertex position
- 646 • $|\rho| < 2 \text{ cm}$, where ρ is the transverse displacement of the vertex position from
647 the beam line

648 The good vertex requirement eliminates non-collision backgrounds such as beam
649 scraping, beam halo, cosmic muon interactions, and instrumental effects.

650 Third, the two electromagnetic objects in the $\gamma\gamma$, $e\gamma$, ee , and ff events must
651 be separated in ϕ by at least 0.05. This requirement protects against beam halo
652 bremsstrahlung, in which a halo muon traveling parallel to the beam line radiates an
653 energetic photon while itself depositing a large amount of energy in the ECAL. In
654 this case, the two ECAL hits would likely be at the same ϕ (and ρ).

655 Fourth, the two EM objects must be separated in R by at least 0.6. Since the
656 isolation cone size used is 0.3, this ensures that the isolation energy of one EM object
657 cannot be in the veto strip (Fig. 2.5) of the other.

658 Finally, the $\gamma\gamma$, $e\gamma$, ee , and ff events must pass an HCAL noise filter and ECAL
659 dead channel filter. The HCAL noise filter guarantees that all HCAL reconstructed
660 hits are inconsistent with any noise source. Noise sources [56] include:

- 661 • Ion feedback in the HPDs absent any true incident photons, in which a thermal
662 electron ionizes a molecule in the HPD acceleration gap, faking a real signal
- 663 • HPD discharge affecting nearly all channels in the same HPD [57], partially
664 explained by the effect of the 4 T CMS magnetic field on the flashover voltage
665 of the dielectric [59]
- 666 • Concurrent signals in nearly all 72 channels of a single RBX, as yet unexplained
- 667 • HF PMT window hits (as opposed to the usual quartz fiber hits)

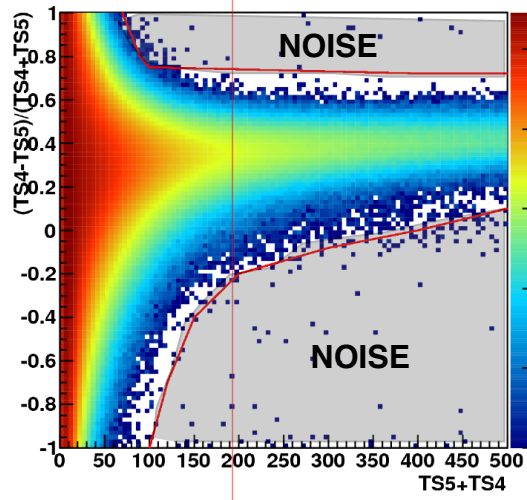


Figure 2.13: $(TS4 - TS5)/(TS4 + TS5)$ vs. $TS4 + TS5$ for a minimum bias sample. HB/HE hits are considered noisy if they lie in the sparsely populated gray region labeled "NOISE" defined by the curved red lines. Adapted from ref. [58].

- 668 • ADC saturation

669 Since HCAL noise may induce fake jets or E_T , events are rejected if any of the
670 following criteria are true:

- 671 • Any HPD has > 17 hits

- 672 • A single HPD has > 10 hits, but every other HPD has zero hits

- 673 • An RBX has > 10 zero-ADC-count hits

674 • Any HB/HE reconstructed hit corresponding to an RBX with > 50 GeV of
675 energy fails a two-dimensional cut defined by the variables $(TS4 - TS5)/(TS4 +$
676 $TS5)$ vs. $TS4 + TS5$, where $TS4(TS5)$ is the hit amplitude in the fourth(fifth)
677 time sample read out for that hit. The cut is defined in Fig. 2.13.

678 The ECAL dead channel filter is designed to flag events in which significant EM
679 energy was deposited in a masked region of the ECAL by using the trigger primitive
680 information for the corresponding trigger tower. Energy deposited in a masked region

681 of ECAL can cause fake E_T . Events are rejected if the trigger primitive E_T exceeds
 682 the maximum value of 63.75 GeV in any trigger tower that is masked in the readout.

683 2.4 Photon Identification Efficiency

684 In order to determine the cross section (or cross section upper limit) for a GGM
 685 signal, the photon identification efficiency is needed. Since no suitably large sample
 686 of $Z \rightarrow \mu\mu\gamma$ events in CMS exists yet, the efficiency calculation relies on the similarity
 687 between detector response to electrons and photons. A scale factor to correct the MC
 688 photon ID efficiency to the real photon efficiency for the data is obtained from the
 689 ratio of the electron efficiency from the data to the electron efficiency from MC.
 690 The different types of photon ID variables—calorimeter and track isolation, ratio of Removed
 691 hadronic to electromagnetic energy of the shower, and transverse shower shape—are refer-
 692 chosen so that their distributions for isolated electrons and photons are similar.³ ence to
 693 The photon selection efficiency is plots

$$\epsilon_\gamma = \epsilon_\gamma^{\text{MC}} \times \frac{\epsilon_e^{\text{data}}}{\epsilon_e^{\text{MC}}} \quad (2.6)$$

694 where

- 695 • ϵ_γ is the photon ID efficiency in data,
- 696 • $\epsilon_\gamma^{\text{MC}}$ is the photon ID efficiency in MC,
- 697 • ϵ_e^{data} is the electron ID efficiency obtained using $Z \rightarrow ee$ electrons in the data
 698 that satisfy the photon ID cuts, and

³ $R9$ differs between photons and radiating electrons, but the requirement $R9 < 1$ is loose enough not to introduce problems with the use of electrons to measure the photon ID efficiency.

- 699 • ϵ_e^{data} is the electron ID efficiency obtained using $Z \rightarrow ee$ electrons in MC that
 700 satisfy the photon ID cuts.

701 The ratio $\epsilon_e^{\text{data}}/\epsilon_e^{\text{MC}}$ is defined as the scale factor by which the GGM signal MC
 702 photon ID efficiency must be multiplied to give an estimate of the photon ID efficiency
 703 in data. The photon ID requirements of Table 2.1 plus the IsoVL HLT requirement
 704 described in Sec. 2.2 and Table 2.3 are repeated in Table 2.4.

Table 2.4: Candidate photon ID requirements.

Variable	Cut
I_{ECAL}	$< 0.012E_T + 6 \text{ GeV}$
I_{HCAL}	$< 0.005E_T + 4 \text{ GeV}$
I_{track}	$< 0.002E_T + 4 \text{ GeV}$
H/E	< 0.05
$\sigma_{i\eta i\eta}$	< 0.011
$I_{\text{ECAL}} - 0.0792\rho + I_{\text{HCAL}} - 0.0252\rho + I_{\text{track}}$	$< 6 \text{ GeV}$
$R9$	< 1

705 2.4.1 Tag and Probe Method

706 A *Z tag and probe* method is utilized to measure the efficiency of the photon ID
 707 cuts in Table 2.1. The tag is a well-identified electron. The probe, by contrast, is as
 708 loosely identified as possible, and all tags must pass the probe criteria in addition to
 709 the stringent tag criteria. The tag and probe criteria used in this study are shown in
 710 Table 2.5.

711 The invariant mass of the tag and probe are required to be within a narrow window
 712 around Z mass. Assuming that the probabilities of the tag and probe legs of the Z
 713 decay to pass the photon ID cuts are uncorrelated, the efficiency can be estimated as

$$\epsilon = \frac{N_{\text{tag-pass}}}{N_{\text{tag-pass}} + N_{\text{tag-fail}}} \quad (2.7)$$

Table 2.5: Tag and probe criteria. The superscript 0.4 indicates that the isolation variable was calculated in a cone of $\Delta R = 0.4$ around the photon candidate. The isolations without superscripts use the standard $\Delta R = 0.3$ cones.

Variable	Cut	
	Tag	Probe
RECO object	photon	photon
HLT	HLT_Ele17_CaloIdVT_CaloIsoVT_TrkIdT_TrkIsoVT_SC8_Mass30_v* (must have fired the 17 GeV leg)	—
H/E	< 0.05	< 0.15
$I_{\text{ECAL}}^{0.4}$	$< 0.006E_T + 4.2 \text{ GeV}$	—
$I_{\text{HCAL}}^{0.4}$	$< 0.0025E_T + 2.2 \text{ GeV}$	—
$I_{\text{track}}^{0.4}$	$< 0.001E_T + 2.0 \text{ GeV}$	—
E_T	$> 25 \text{ GeV}$	—
SC E_T	—	$> 15 \text{ GeV}$
SC $ \eta $	< 1.4442	< 1.4442
$\sigma_{i\eta i\eta}$	< 0.009	—
Has pixel seed	Yes	—
Track match type	General track ^a	—
Track match ΔR	< 0.04	—
Track match p_T	$> 15 \text{ GeV}$	—
Track match $ \eta $	< 1.479	—

^aA general track is reconstructed with the CMS standard combinatorial track finder [60].

714 where $N_{\text{tag-pass}}$ is the number of tag-probe pairs in which the probe leg passes the
 715 photon ID cuts under study and $N_{\text{tag-fail}}$ is the number of tag-probe pairs in which
 716 the probe leg fails the cuts. Implicit in these definitions is a double counting of pairs
 717 in which both electrons pass the tag and probe criteria [61]. In addition, in the rare
 718 circumstance (less than 1% in MC [61]) that two or more probes may be matched to
 719 one tag, the pair with invariant mass closest to the Z mass is chosen.

720 In practice, $N_{\text{tag-pass}}$ and $N_{\text{tag-fail}}$ are returned by a simultaneous unbinned maxi-
 721 mum likelihood fit to the invariant mass distributions of tag-pass and tag-fail events,
 722 with appropriate signal and background PDF assumptions. The fit form used is

$$\begin{aligned} f_{\text{tag-pass}}(m_{\text{tag-pass}}) &= \epsilon N_S f_S^{\text{pass}}(m_{\text{tag-pass}}) + N_B^{\text{pass}} f_B^{\text{pass}}(m_{\text{tag-pass}}) \\ f_{\text{tag-fail}}(m_{\text{tag-fail}}) &= (1 - \epsilon) N_S f_S^{\text{fail}}(m_{\text{tag-fail}}) + N_B^{\text{fail}} f_B^{\text{fail}}(m_{\text{tag-fail}}) \end{aligned} \quad (2.8)$$

723 where $f_{\text{tag-pass}}(m_{\text{tag-pass}})$ and $f_{\text{tag-fail}}(m_{\text{tag-fail}})$ are the tag-pass and tag-fail PDFs,
 724 respectively; ϵ is the efficiency; N_S is the total number of Z signal events summed over
 725 both samples; $f_S^{\text{pass}}(m_{\text{tag-pass}})$ and $f_S^{\text{fail}}(m_{\text{tag-fail}})$ are the tag-pass and tag-fail signal
 726 PDFs, respectively; N_B^{pass} and N_B^{fail} are the numbers of background events in the tag-
 727 pass and tag-fail samples, respectively; and $f_B^{\text{pass}}(m_{\text{tag-pass}})$ and $f_B^{\text{fail}}(m_{\text{tag-fail}})$ are the
 728 tag-pass and tag-fail background PDFs, respectively. This particular implementation
 729 of the tag and probe methodology is based on tag `CMSSW_4_2_5` of the CMSSW
 730 package `PhysicsTools/TagAndProbe`, and uses the MINUIT2 [62] library, as coded
 731 in RooFit [63], for the likelihood maximization. For this study, CMSSWv4.2.8 was
 732 used.

733 For both samples, the signal shape is assumed to be a Crystal Ball function [64]
 734 convoluted with the Z generated lineshape, while the background shape is a PDF
 735 that describes the falling background as well as the kinematic turn-on at low invariant

736 mass. The background PDF, called `RooCMSShape` [61], is given by

$$f_{\text{RooCMSShape}}(x) = \begin{cases} 1e20 & \text{for } (x - \mu)\gamma < -70 \\ 0 & \text{for } (x - \mu)\gamma > 70 \\ \text{erfc}((\alpha - x)\beta) \exp(-(x - \mu)\gamma) & \text{otherwise} \end{cases} \quad (2.9)$$

737 where α , β , γ , and μ are parameters of the fit, most of which are held fixed. In the
738 three lowest E_T bins, all parameters of the tag-pass and tag-fail background PDFs
739 are left floating, because the effect of the relaxed E_T cuts has a significant effect on
740 the background shape. More details of the signal and background PDFs are given
741 in Table 2.6. The fixed signal and background parameter values were determined by
742 fitting a small sample ($0.0 \leq \eta < 0.25$) of `Fall11 MC signal (DYJetsToLL)` and back-
743 ground (`QCD_Pt-20to30_BCToE`, `QCD_Pt-30to80_BCToE`, `QCD_Pt-80to170_BCToE`,
744 `GJet_Pt-20_doubleEMEnriched`, `WJetsToLNu`, `TTJets`) with parameters left float-
745 ing.⁴

Added

746 Some fit examples are shown in Figures 2.14 and 2.15. In Fig. 2.14, which shows fits
747 fits to data and MC for $15 \text{ GeV} \leq \text{probe } E_T < 20 \text{ GeV}$, the kinematic turn-on is below
748 the invariant mass range covered by the plot. The exponentially falling background
749 is easily seen underneath the signal, and is especially pronounced in the background-
750 dominated tag-fail sample.

751 2.4.2 Photon Efficiency Scale Factor $\epsilon_e^{\text{data}}/\epsilon_e^{\text{MC}}$

752 Figure 2.16 shows the dependence of the photon ID efficiency scale factor $\epsilon_e^{\text{data}}/\epsilon_e^{\text{MC}}$
753 on E_T , η , and N_{jet} , where jets are defined as in Table 2.2, but with only the two
754 Z electrons considered as candidates for overlap removal. Errors are statistical only.

⁴See Appendix A for a discussion of the MC samples.

Table 2.6: Parameter values (parameter definitions are in the text) for the signal and background PDFs for the different samples. The background PDF applies to all efficiency bins except the four lowest E_T bins, which use a floating `RooCMSShape` background. When a bracketed range is given, the parameter is allowed to float within that range. When a constant is given, the parameter is fixed to that constant.

PDF	Crystal Ball fit parameters				RooCMSShape fit parameters			
	μ	σ	α	n	μ	α	β	γ
Tag-pass signal	[-1.0, 1.0]	[1.0, 3.0]	0.87	97.0	N/A	N/A	N/A	N/A
Tag-fail signal	[-1.0, 1.0]	[1.0, 3.0]	0.73	134.9	N/A	N/A	N/A	N/A
Tag-pass background	N/A	N/A	N/A	N/A	65.0	61.949	0.04750	0.01908
Tag-fail background	N/A	N/A	N/A	N/A	α	[50.0, 100.0]	0.065	0.048

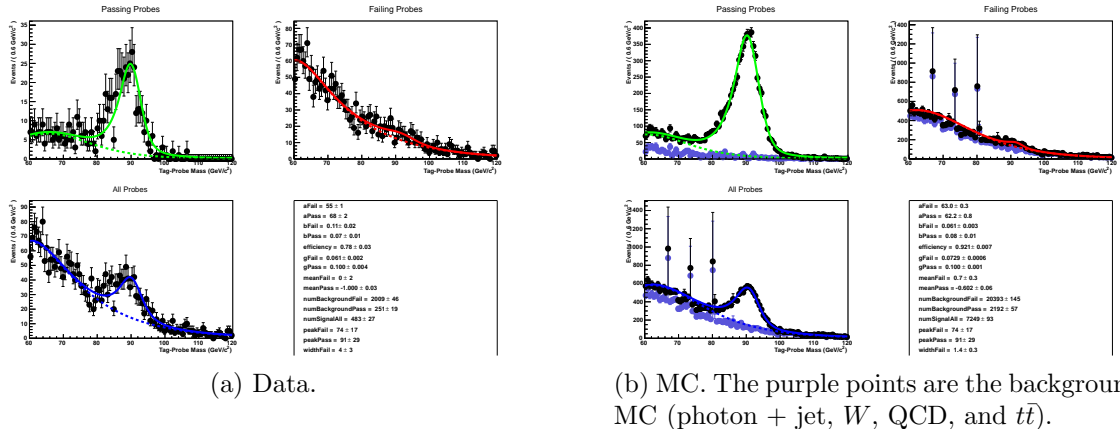


Figure 2.14: Tag and probe invariant mass fits for $15 \text{ GeV} \leq \text{probe } E_T < 20 \text{ GeV}$. Errors are statistical only. The tag-pass fit is shown in green, the tag-fail fit in red, and a fit to both samples in blue. Dotted lines are the background components of the fits; solid lines are signal plus background.

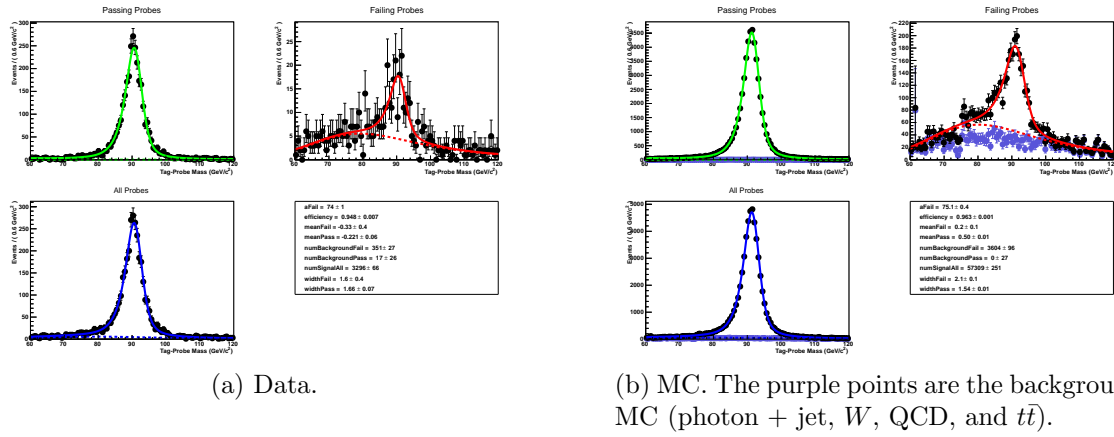


Figure 2.15: Tag and probe invariant mass fits for $-0.25 \leq \text{probe } \eta < -0.5$. Errors are statistical only. The tag-pass fit is shown in green, the tag-fail fit in red, and a fit to both samples in blue. Dotted lines are the background components of the fits; solid lines are signal plus background.

755 There no significant dependence of the scale factor on these variables, so only one
756 scale factor is computed from the entire dataset.

757 The effect of pileup is studied by comparing the efficiencies ϵ_e^{data} and ϵ_e^{MC} vs. the
758 number of primary vertices (N_{PV}) in the event. The efficiency only drops a few percent
759 for events with large N_{PV} after using pileup-corrected isolation cuts, as can be seen in
760 Figure 2.17a. The MC tracks the data, and the scale factor is flat vs. N_{PV} , as shown
761 in Fig. 2.17b.

762 The scale factor is measured to be $\epsilon_e^{\text{data}}/\epsilon_e^{\text{MC}} = 0.994 \pm 0.002(\text{stat.}) \pm 0.035(\text{syst.})$.
763 Four main sources of systematic error, in addition to the statistical error of 0.2%, were
764 studied.

765 **Different behavior of electrons and photons in MC** Even though the photon
766 ID cuts are designed to be similarly efficient for both electrons and photons,
767 there might be a small difference in the performance between the two kinds
768 of particles, e.g. because of electron bremsstrahlung. To check this effect, the
769 MC electron ID efficiency was calculated using a $Z \rightarrow ee$ sample and the MC
770 photon ID efficiency was calculated using a $\gamma + \text{jets}$ sample. Both samples were

Official
result
uses this
syst.
error, so
I am not
recheck-
ing
it

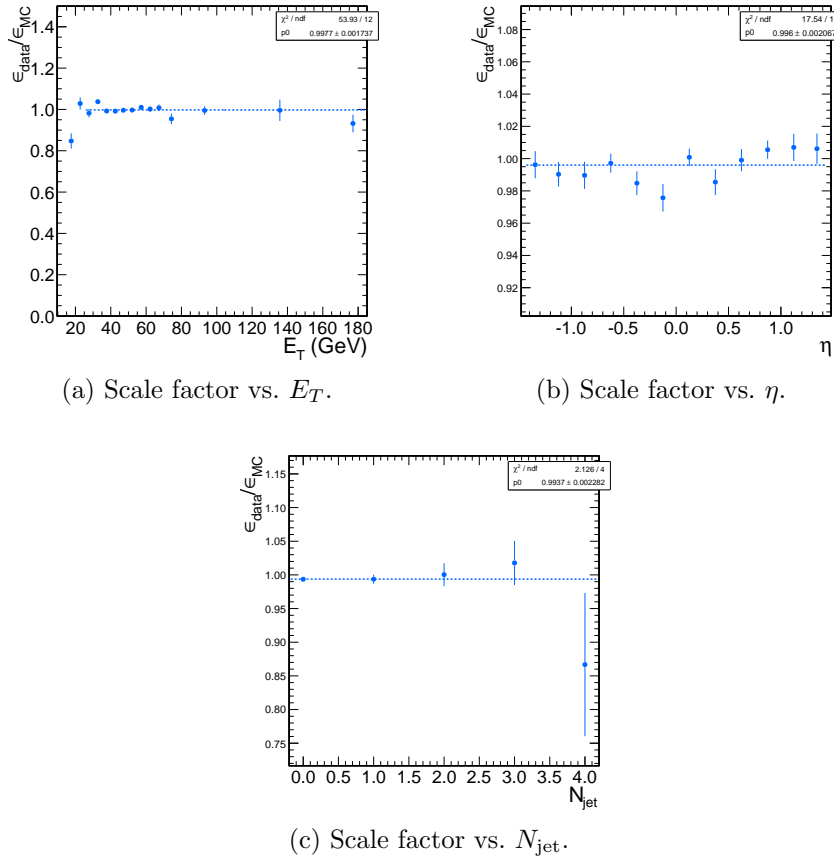


Figure 2.16: Dependence of the photon ID efficiency scale factor on some kinematic variables. Errors are statistical only.

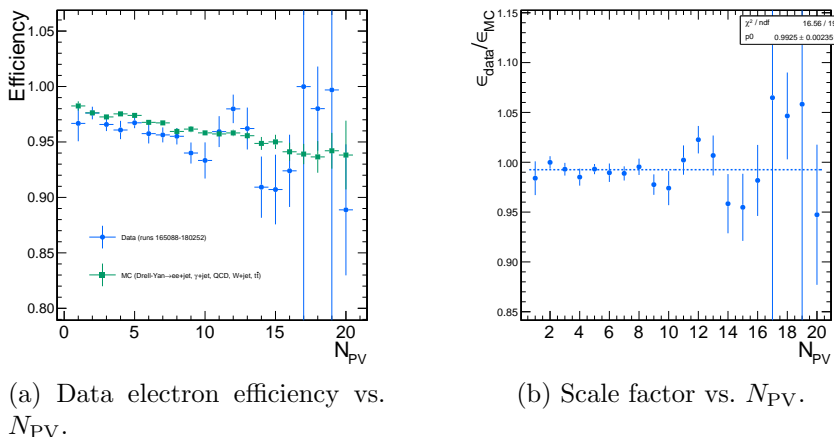


Figure 2.17: Dependence of the photon ID efficiency scale factor on the number of primary vertices per event. Errors are statistical only.

771 reconstructed in CMSSWv3.6. Half the difference between these two results,
 772 0.5%, was taken as an error on the scale factor.

Corrected

773 **Pileup** To account for the possibility that the MC simulation may not adequately some of
 774 reproduce the data in a high pileup environment, the data/MC scale factor these
 775 for events with 1-4 good reconstructed primary vertices was calculated, along bullets
 776 with the same for events with ≥ 5 good reconstructed primary vertices. The
 777 difference between the scale factors from both samples, 2.4%, was taken as an
 778 error on the scale factor from pileup.

779 **Signal fit over/underestimation** It was found that the signal fit slightly under-
 780 estimates the data in the tag-pass sample, and slightly overestimates it in the
 781 tag-fail sample. To cover this effect with a systematic error, the efficiencies in
 782 data and MC, and then the scale factor, were recalculated using the background
 783 (from fit) subtracted integrals of the tag-pass and tag-fail distributions, rather
 784 than the fitted signal yields in those distributions. The difference between the
 785 scale factor found in this way and the nominal scale factor, 1.9%, was taken as
 786 an error on the scale factor.

787 **Signal and background shape assumption** To assess the magnitude of the error
 788 from the signal and background shape assumptions, the tag-pass and tag-fail
 789 tail parameters (Crystal Ball α and n) were varied by $\pm 1\sigma$, and the background
 790 shape was varied between `RooCMSShape`, exponential, power law, and quadratic.
 791 All possible combinations of varied parameters were generated, and the data and
 792 MC were refit and new scale factors generated according to those combinations.
 793 The error was taken as the largest deviation of the scale factor from nominal,
 794 1.8%.

795 Finally, the pixel veto efficiency was estimated from MC to be 0.96 ± 0.005 (syst.),
 796 with error due to varying assumptions of the tracker material distribution [65].

797 Chapter 3

798 Data Analysis

799 The signature of GGM SUSY particle production in this search is an excess of two-
800 photon events with high \cancel{E}_T . \cancel{E}_T is reconstructed using the particle flow algorithm
801 as described in Sec. 2.1.3. Candidate two-photon events, as well as control events,
802 are selected according to the offline object criteria presented in Secs. 2.1.1, 2.1.2,
803 and 2.1.3; the event quality criteria in Sec. 2.3; and the trigger requirements in Sec. 2.2.
804 These are summarized in Table 3.1.

Table 3.1: Selection criteria for $\gamma\gamma$, $e\gamma$, ee , and ff events.

Variable	Cut			
	$\gamma\gamma$	$e\gamma$	ee	ff
HLT match	IsoVL	IsoVL	IsoVL	IsoVL R9Id
E_T	$> 40/ > 25$ GeV			
$SC \eta $	< 1.4442	< 1.4442	< 1.4442	< 1.4442
H/E	< 0.05	< 0.05	< 0.05	< 0.05
$R9$	< 1	< 1	< 1	< 1
Pixel seed	No/No	Yes/No	Yes/Yes	No/No
$I_{\text{comb}}, \sigma_{inj\eta}$	< 6 GeV $\&\&$ < 0.011	< 6 GeV $\&\&$ < 0.011	< 6 GeV $\&\&$ < 0.011	< 20 GeV $\&\&$ $(\geq 6$ GeV \parallel $\geq 0.011)$
JSON	Yes	Yes	Yes	Yes
No. good PVs	≥ 1	≥ 1	≥ 1	≥ 1
ΔR_{EM}	> 0.6	> 0.6	> 0.6	> 0.6
$\Delta\phi_{\text{EM}}$	≥ 0.05	≥ 0.05	≥ 0.05	≥ 0.05

805 This search utilizes 4.7 fb^{-1} of CMS data collected during the period April
 806 December 2011, corresponding to the following datasets [66]:

- 807 • /Photon/Run2011A-05Jul2011ReReco-ECAL-v1/AOD
- 808 • /Photon/Run2011A-05Aug2011-v1/AOD
- 809 • /Photon/Run2011A-03Oct2011-v1/AOD
- 810 • /Photon/Run2011B-PromptReco-v1/AOD

811 The search strategy is to model the backgrounds to the GGM SUSY signal using
 812 \cancel{E}_T shape templates derived from the control samples, and then to look for a high- \cancel{E}_T
 813 excess above the estimated background in the $\gamma\gamma$ sample. There are two categories
 814 of backgrounds: QCD processes with no real \cancel{E}_T and electroweak processes with real
 815 \cancel{E}_T from neutrinos. The relevant QCD background processes are multijet production
 816 with at least two jets faking photons, photon + jet production with at least one jet
 817 faking a photon, and diphoton production, and Z production with a radiated photon
 818 where at least one of the Z decay products (typically a jet) fakes a photon. The
 819 relevant electroweak background processes, which are small compared to the QCD
 820 background, involve $W \rightarrow e\nu$ decay with a recoiling jet that fakes a photon or a
 821 real radiated photon (the W may come from the decay of a top quark in $t\bar{t}$ events).
 822 In both cases, the electron is misidentified as a photon due to a small inefficiency
 823 in reconstructing the electron pixel seed. The main diagrams contributing to the
 824 QCD(electroweak) backgrounds are shown in Figure 3.1(3.2).

825 Data control samples are used to model all of the backgrounds. The primary
 826 control sample used to model the QCD background is the ff sample, which is similar
 827 to the candidate $\gamma\gamma$ sample but with combined isolation or $\sigma_{inj\eta}$ cuts inverted. The cuts
 828 on these variables are used to distinguish between photons and jets, so by inverting
 829 those cuts, the resulting ff sample becomes enriched with QCD dijets. Because the

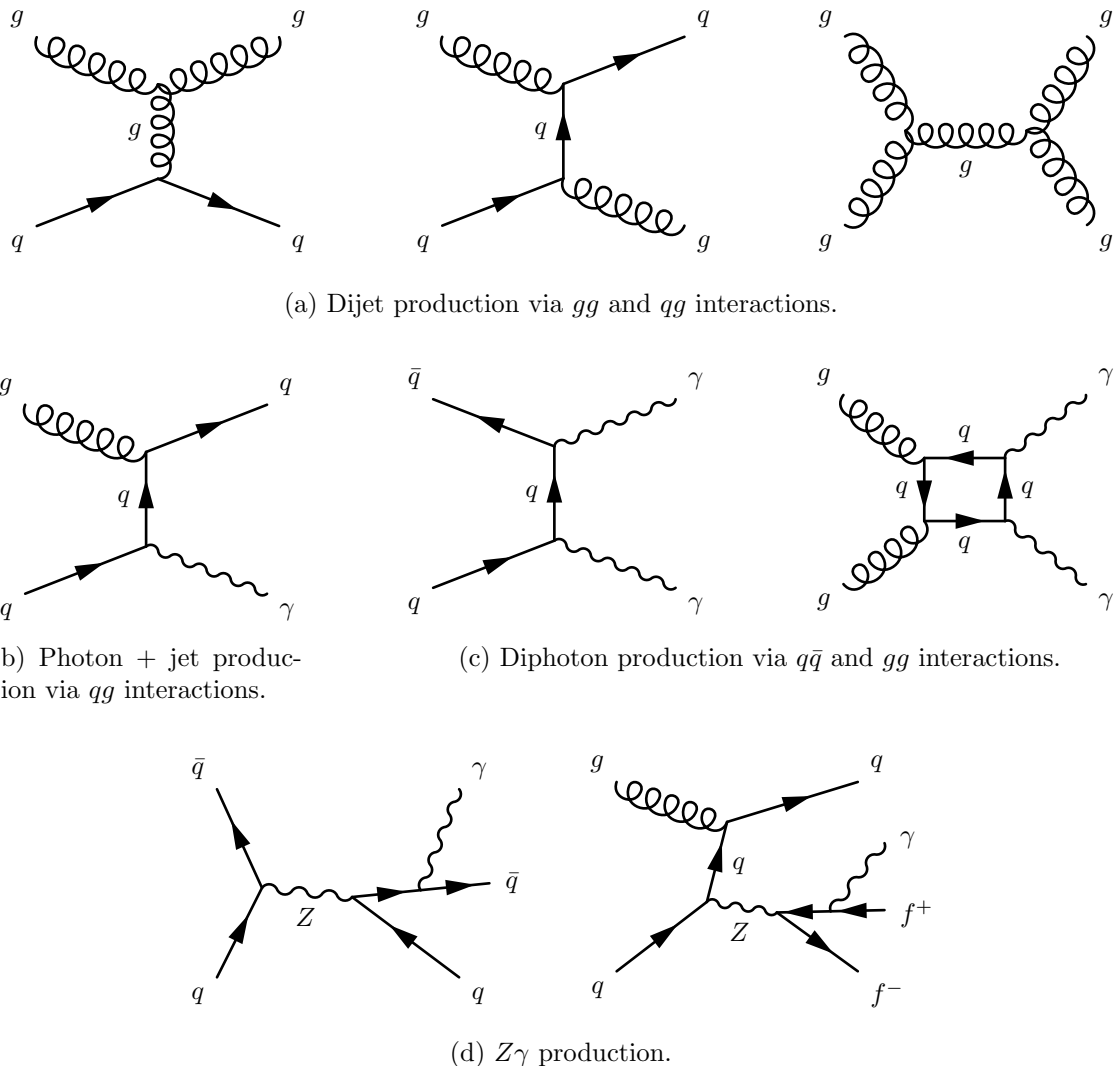


Figure 3.1: Representative Feynman diagrams of some QCD backgrounds to the GGM SUSY search.

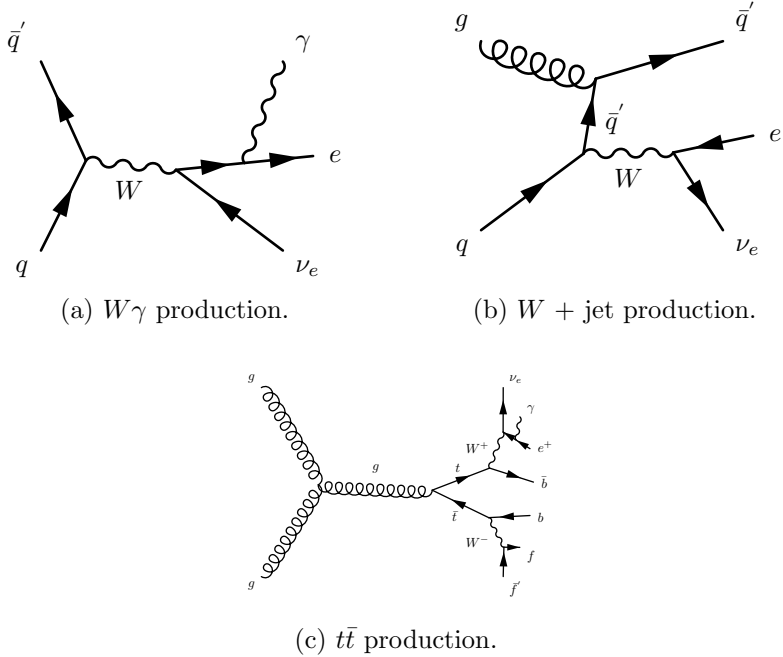


Figure 3.2: Representative Feynman diagrams of some electroweak backgrounds to the GGM SUSY search.

fake photons are still required to pass a tight cut on H/E , they are guaranteed to be very electromagnetic jets, with an EM energy scale and resolution similar to that of the candidate photons. This insures that the resulting estimate of the \cancel{E}_T shape does not have too long of a tail from severe HCAL mis-measurements that are actually rare in the $\gamma\gamma$ sample.

As a cross-check, the ee sample is also used to model the QCD background. This sample of Z decays should have no true \cancel{E}_T , just like the ff sample, and the electron definition (differing from the photon definition only in the presence of a pixel seed) insures that the electron energy scale and resolution is similar to that of the photon.

Finally, the $e\gamma$ sample is used to model the electroweak background from $W \rightarrow e\nu$ decays. The $e\gamma$ \cancel{E}_T distribution is scaled by the electron \rightarrow photon misidentification rate to predict the number of $W\gamma$, $W + \text{jet}$, and $t\bar{t}$ events in the $\gamma\gamma$ sample.

The remainder of this chapter describes the data analysis procedures and the final results of the search. Sec. 3.1 addresses the QCD background estimation. Sec. 3.2

844 addresses the electroweak background estimation. The chapter concludes with a dis-
 845 cussion of systematic errors in Sec. 3.3 and a presentation of the final results in
 846 Sec. 3.4.

847 3.1 Modeling the QCD Background

848 3.1.1 Outline of the Procedure

849 Due to the fact that the CMS ECAL energy resolution is much better than the
 850 HCAL energy resolution, the energies of the two candidate photons in the events of
 851 the $\gamma\gamma$ sample are typically measured to far greater accuracy and precision than the
 852 energy of the hadronic recoil in those events. Therefore, fake E_T in the $\gamma\gamma$ sample
 853 is almost entirely the result of hadronic mis-measurement in QCD dijet, photon +
 854 jet, and diphoton events. The strategy employed to model this background is to find
 855 a control sample in data consisting of two well-measured EM objects, just like the
 856 candidate $\gamma\gamma$ sample, and assign each event a weight to account for the underlying
 857 kinematic differences between the control and candidate samples. Once the reweighted
 858 E_T spectrum of the control sample is created, it is then normalized in the low- E_T
 859 region, the assumption being that GGM SUSY does not predict a significant amount
 860 of events at low E_T . There are three aspects of this QCD background estimation
 861 procedure that bear highlighting:

862 **Choice of control sample** Since the underlying cause of E_T in the candidate sam-
 863 ple is mis-measured hadronic activity, a control sample with similar hadronic
 864 activity to the candidate sample should be chosen. Hadronic activity refers to
 865 number of jets, jet E_T , pileup, etc.

866 **Reweighting** The control sample is reweighted so that its E_T spectrum appears as it
 867 would if the control sample had the same kinematic properties as the candidate

sample (i.e. particle p_T and η distributions, etc.). By choosing an appropriate control sample and reweighting it, the control \cancel{E}_T distribution should now match both the hadronic activity and the kinematics of the candidate sample.

Normalization Finally, the control E_T distribution is normalized in a region of low \cancel{E}_T , where contamination from the expected GGM SUSY signal is small. This implies an extrapolation of the low- \cancel{E}_T QCD background prediction to the high- \cancel{E}_T signal region.

As explained in the beginning of this chapter, the ff sample is used as the primary QCD control sample, while the ee sample is used as a cross-check. Both samples have two well-measured EM objects per event, no real \cancel{E}_T , and similar hadronic activity to the $\gamma\gamma$ sample. Figure 3.3 shows a comparison of the shapes of some distributions relevant to hadronic activity between the $\gamma\gamma$, ee , and ff samples. In general, the ee sample has less hadronic activity than the $\gamma\gamma$ and ff samples, as shown by the more steeply falling ee distributions in Figs. 3.3a, 3.3b, 3.3c, and 3.3d. In addition to the kinematic reweighting, there is also a reweighting by number of jets per event, which attempts to correct for this difference (see Sec. 3.1.2).

3.1.2 Reweighting

To reweight the control sample events to match the kinematics of the candidate sample events, a weight based on the p_T of the di-EM-object system and the number of jets in the event is used. As explained in Sec. 3.1.1, E_T in the $\gamma\gamma$, ff , and ee samples is due to the poorly measured hadronic recoil off the well-measured di-EM system. Therefore, the p_T of the di-EM system is a good handle on the true magnitude of the hadronic recoil, which affects the measured \cancel{E}_T . The di-EM system is depicted in Figure 3.4. As shown in Figure 3.5, \cancel{E}_T is largely uncorrelated with di-EM p_T , so there is little danger of reweighting away a true signal excess.

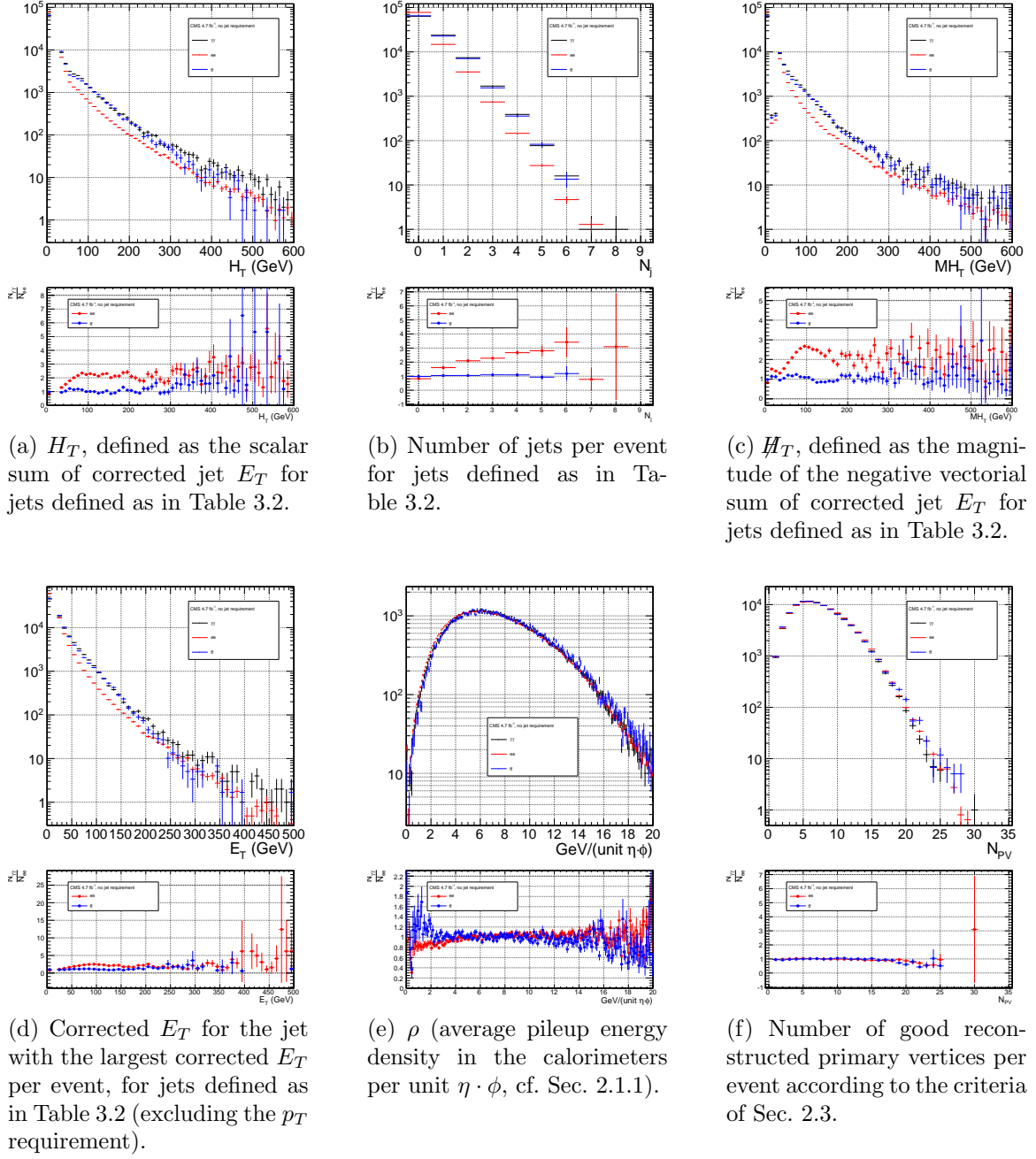


Figure 3.3: Comparison of the shapes of some distributions relevant to hadronic activity between the $\gamma\gamma$, ee ($81 \text{ GeV} \leq m_{ee} < 101 \text{ GeV}$), and ff samples. The ee and ff distributions are normalized to the number of events in the $\gamma\gamma$ distribution. Errors are statistical only.

Table 3.2: Definition of HB/HE/HF hadronic jets.

Variable	Cut
Algorithm	L1FastL2L3Residual corrected PF (cf. Sec. 2.1.3)
p_T	$> 30 \text{ GeV}$
$ \eta $	< 5.0
Neutral hadronic energy fraction	< 0.99
Neutral electromagnetic energy fraction	< 0.99
Number of constituents	> 1
Charged hadronic energy	$> 0.0 \text{ GeV}$ if $ \eta < 2.4$
Number of charged hadrons	> 0 if $ \eta < 2.4$
Charged electromagnetic energy fraction	< 0.99 if $ \eta < 2.4$
ΔR to nearest PF electron ^a , muon ^b , or one of the two primary EM objects	> 0.5

^aA PF electron is defined as an electron reconstructed with the PF algorithm [42] with $p_T > 15 \text{ GeV}$, $|\eta| < 2.6$, and $(I_{\text{charged}} + I_{\text{photon}} + I_{\text{neutral}})/p_T < 0.2$, where $I_{\text{charged}}(I_{\text{photon}})(I_{\text{neutral}})$ is the sum of PF charged hadron(PF photon)(PF neutral hadron) momenta in a $\Delta R = 0.4$ cone around the PF electron.

^bMuons are reconstructed [43] from a combination of muon station and inner tracker hits. Here, a muon must have track $\chi^2 < 10$, at least one good muon station hit, inner track transverse impact parameter $< 0.02 \text{ cm}$, inner track longitudinal impact parameter $< 0.5 \text{ cm}$, $p_T > 15 \text{ GeV}$, $|\eta| < 2.6$, and $(I_{\text{ECAL}} + I_{\text{HCAL}} + I_{\text{track}})/p_T < 0.2$, where $I_{\text{ECAL}}(I_{\text{HCAL}})(I_{\text{track}})$ is the sum of ECAL(HCAL)(track) momenta in a $\Delta R = 0.3$ cone around the muon.

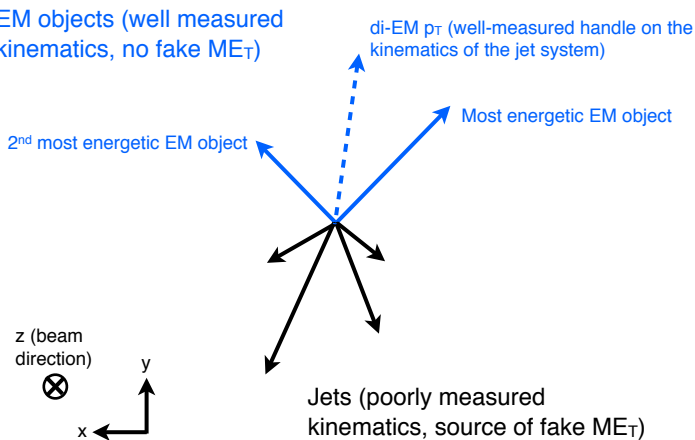


Figure 3.4: Cartoon showing the di-EM system in blue and the hadronic recoil in black. The di-EM p_T (dashed blue line) is used to reweight the control sample kinematic properties to match those of the candidate $\gamma\gamma$ sample.

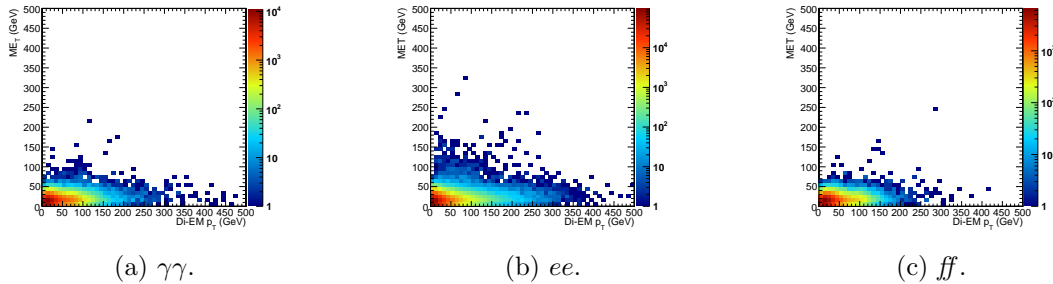


Figure 3.5: E_T vs. di-EM p_T .

Whereas the di-EM p_T reweighting accounts for differences in production kinematics between the control and $\gamma\gamma$ samples, a simultaneous reweighting based on the number of jets in the event accounts for differences in hadronic activity between the samples, especially between ee and $\gamma\gamma$ (cf. Fig. 3.3). Jets are defined as in Table 2.2. Figure 3.6 shows the effect of reweighting by number of jets per event, which is to increase(decrease) the tail of the $ee(jj)$ E_T spectrum.

899 Although the electron and photon energies are well measured by the ECAL, the
 900 ECAL-only measurement of the fake photon energy (cf. Sec 2.1.1) is biased slightly
 901 low due to the fact that fakes (which are really jets) tend to deposit some energy in
 902 the HCAL. This can be seen in Figs. 3.7 and 3.8, which show the relative difference
 903 between the ECAL-only E_T measurement and the PF E_T measurement vs. EMF for
 904 electrons, photons, and fakes. PF E_T is defined as the L1Fast-corrected E_T of the
 905 nearest PF jet with $p_T \geq 20$ GeV (i.e., the E_T of the PF jet object reconstructed from
 906 the same ECAL shower as the fake photon). On average, the fakes tend to deposit
 907 a few percent more energy in the HCAL than the electrons or photons, which is
 908 recovered by the PF algorithm. For this reason, the PF p_T is used in the calculation
 909 of di-EM p_T rather than the ECAL-only p_T .¹ This leads to a modest improvement in
 910 the agreement between the ee and ff E_T spectra, as shown in Figure 3.9.

The control sample event weights are defined as

¹In the few events ($\mathcal{O}(10^{-3})$) in which two PF jet objects, corresponding to the two electrons or fakes, are not found, the ECAL-only p_T is used.

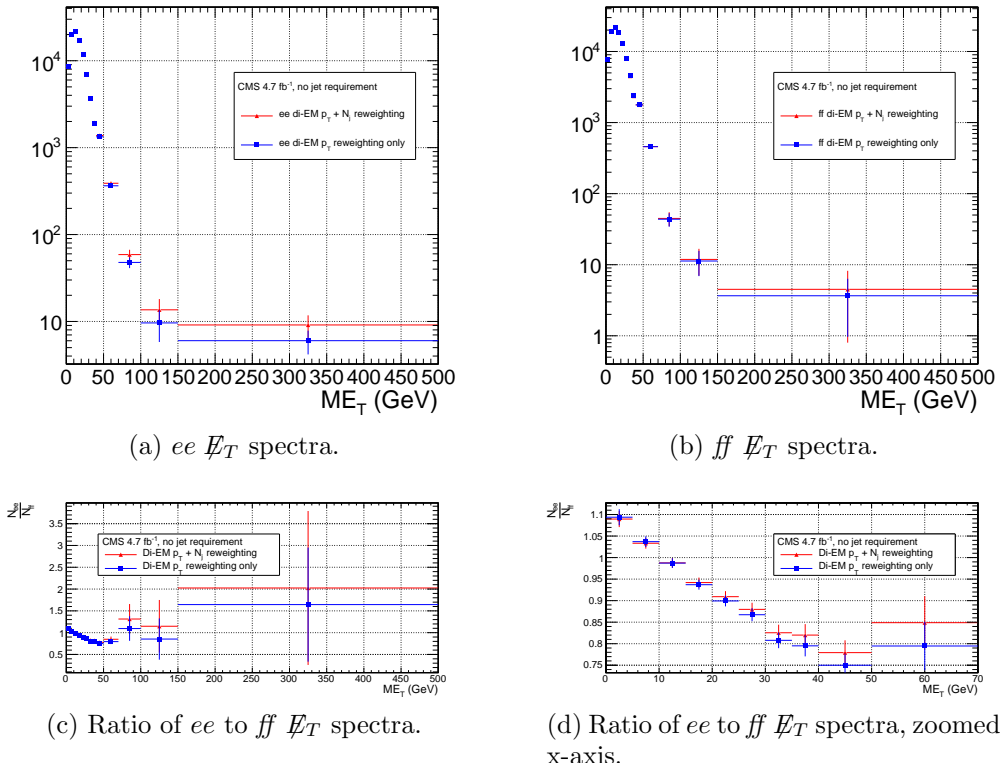


Figure 3.6: \mathbb{E}_T spectra of the reweighted ee ($81 \text{ GeV} \leq m_{ee} < 101 \text{ GeV}$) and ff control samples. Blue squares indicate di-EM p_T reweighting only; red triangles indicate di-EM $p_T + \text{number of jets}$ reweighting. PF p_T (cf. p. 64) is used to calculate the di-EM p_T . The full normalization procedure is employed, along with ee sideband subtraction (discussed at the end of this section). Error bars are statistical only.

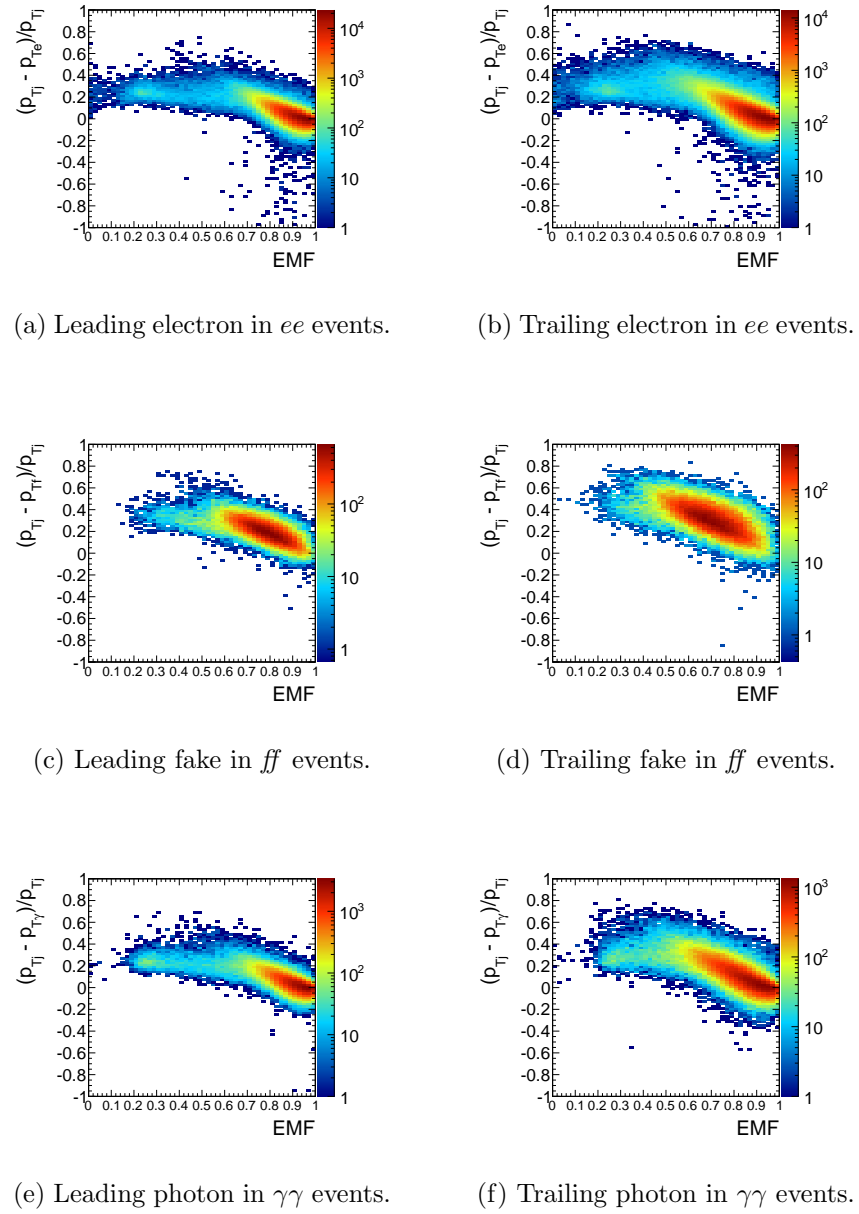


Figure 3.7: Relative difference between the ECAL-only E_T measurement and the PF E_T measurement vs. EMF. PF E_T is defined in the text.

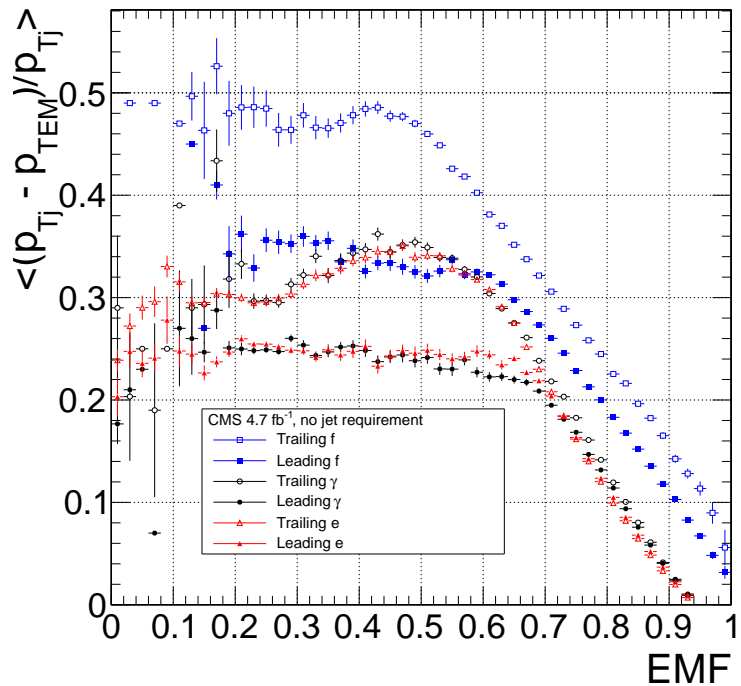


Figure 3.8: Average relative difference between the ECAL-only E_T measurement and the PF E_T measurement vs. EMF for the leading (filled marker) and trailing (open marker) electrons in ee events (red triangles), fakes in ff events (blue squares), and photons in $\gamma\gamma$ events (black circles). These are nothing more than profile histograms of Fig. 3.7. PF E_T is defined in the text. Error bars are statistical only.

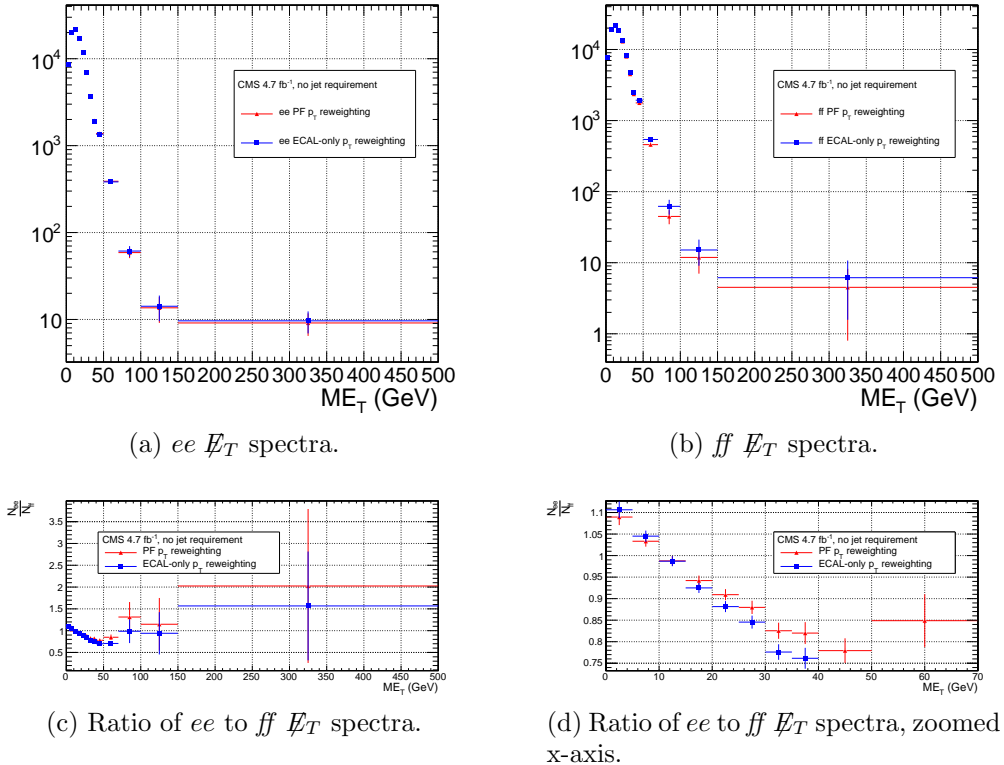


Figure 3.9: E_T spectra of the reweighted ee ($81 \text{ GeV} \leq m_{\text{ee}} < 101 \text{ GeV}$) and ff control samples. Blue squares indicate reweighting using the ECAL-only p_T estimate; red triangles indicate reweighting using the PF p_T estimate. The full reweighting and normalization procedure is employed, along with ee sideband subtraction (discussed at the end of this section). Error bars are statistical only.

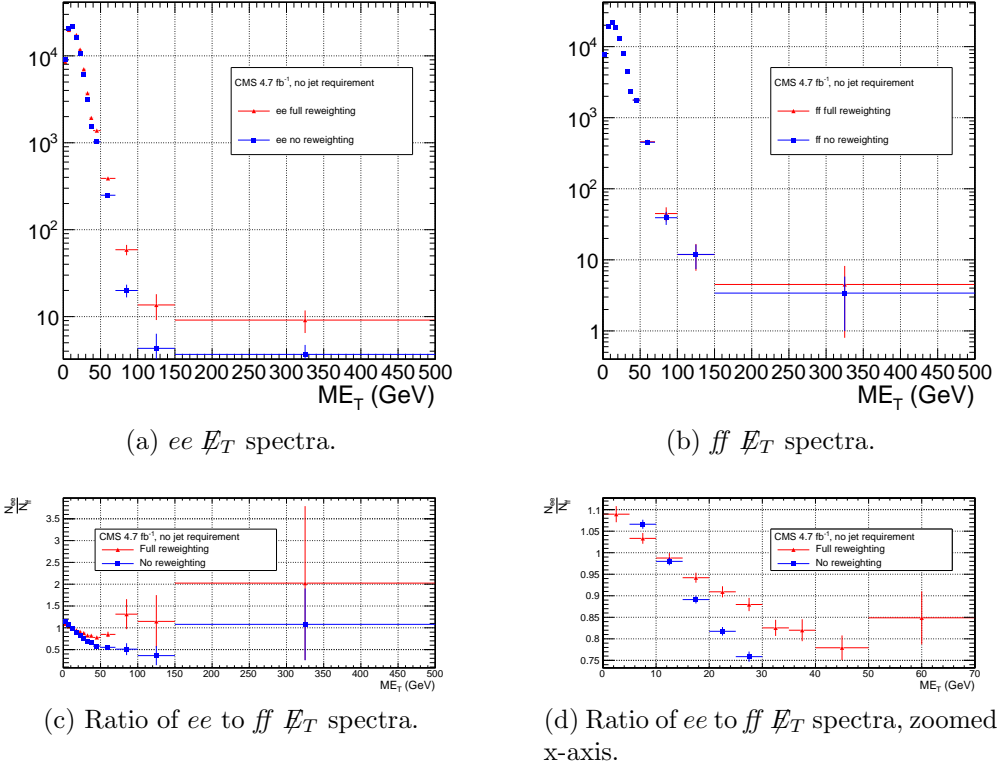


Figure 3.10: E_T spectra of the ee ($81 \text{ GeV} \leq m_{ee} < 101 \text{ GeV}$) and ff control samples. Red triangles indicate full di-EM $p_T +$ number of jets reweighting; blue squares indicate no reweighting. PF p_T (cf. p. 66) is used to calculate the di-EM p_T . The full normalization procedure is employed, along with ee sideband subtraction (discussed at the end of this section). Error bars are statistical only.

$$w_{ij} = \frac{N_{\text{control}}}{N_{\gamma\gamma}} \frac{N_{\gamma\gamma}^{ij}}{N_{\text{control}}^{ij}} \quad (3.1)$$

where i runs over the number of di-EM p_T bins, j runs over the number of jet bins, N_{control} is the total number of events in the control sample, $N_{\gamma\gamma}$ is the total number of events in the $\gamma\gamma$ sample, $N_{\gamma\gamma}^{ij}$ is the number of $\gamma\gamma$ events in the i^{th} di-EM p_T bin and j^{th} jet bin, and N_{control}^{ij} is the number of control sample events in the i^{th} di-EM p_T bin and j^{th} jet bin. The effect of the reweighting is more significant for the ee sample than for the ff sample, as shown in Figure 3.10.

918 The ee sample contains a non-negligible background of $t\bar{t}$ events in which both
 919 W bosons decay to electrons. These events have significant real \cancel{E}_T from the two
 920 neutrinos (unlike the $\gamma\gamma$ events), and therefore inflate the background estimate at
 921 high \cancel{E}_T . In order to remove the $t\bar{t}$ contribution from the ee sample, a sideband
 922 subtraction method is employed.

923 Only events in the ee sample with $81 \text{ GeV} \leq m_{ee} < 101 \text{ GeV}$, where m_{ee} is the
 924 di-electron invariant mass, are used in the QCD background estimate. This choice
 925 maximizes the ratio of Z signal to background. The sidebands used to estimate the
 926 background contribution within the Z window are defined such that $71 \text{ GeV} \leq m_{ee} <$
 927 81 GeV and $101 \text{ GeV} \leq m_{ee} < 111 \text{ GeV}$.

928 The full reweighting procedure is applied to the Z signal region and the two
 929 sideband regions independently. Only Z signal events are used in the calculation of
 930 the di-EM p_T weights for the Z signal region, and likewise only the events within
 931 a given sideband region are used in the calculation of the weights for that region.
 932 Assuming a constant $t\bar{t}$ background shape, the resulting reweighted sideband \cancel{E}_T
 933 distributions are added together and subtracted from the reweighted Z signal \cancel{E}_T
 934 distribution. The sideband subtracted Z signal \cancel{E}_T distribution is then normalized
 935 as discussed in Secs. 3.1.1 and 3.1.3. The statistical and reweighting error from the
 936 sideband regions is propagated to the error on the final ee QCD \cancel{E}_T estimate.

937 The di-EM p_T weights for the two ee sideband regions are shown in Figure 3.11.
 938 The overall scale of the weights, as well as the trend with di-EM p_T , is similar for
 939 the two regions (except at high di-EM p_T , where the statistics are poor anyway).
 940 Figure 3.12 shows the \cancel{E}_T spectra for the two sideband regions and the Z signal
 941 region after subtraction. The shapes of the spectra indicate that the high- \cancel{E}_T $t\bar{t}$ tail,
 942 present in the sideband distributions, was successfully subtracted from the Z signal
 943 distribution.

944 The ee ($81 \text{ GeV} \leq m_{ee} < 101 \text{ GeV}$), ff , and $\gamma\gamma$ di-EM p_T spectra for events with

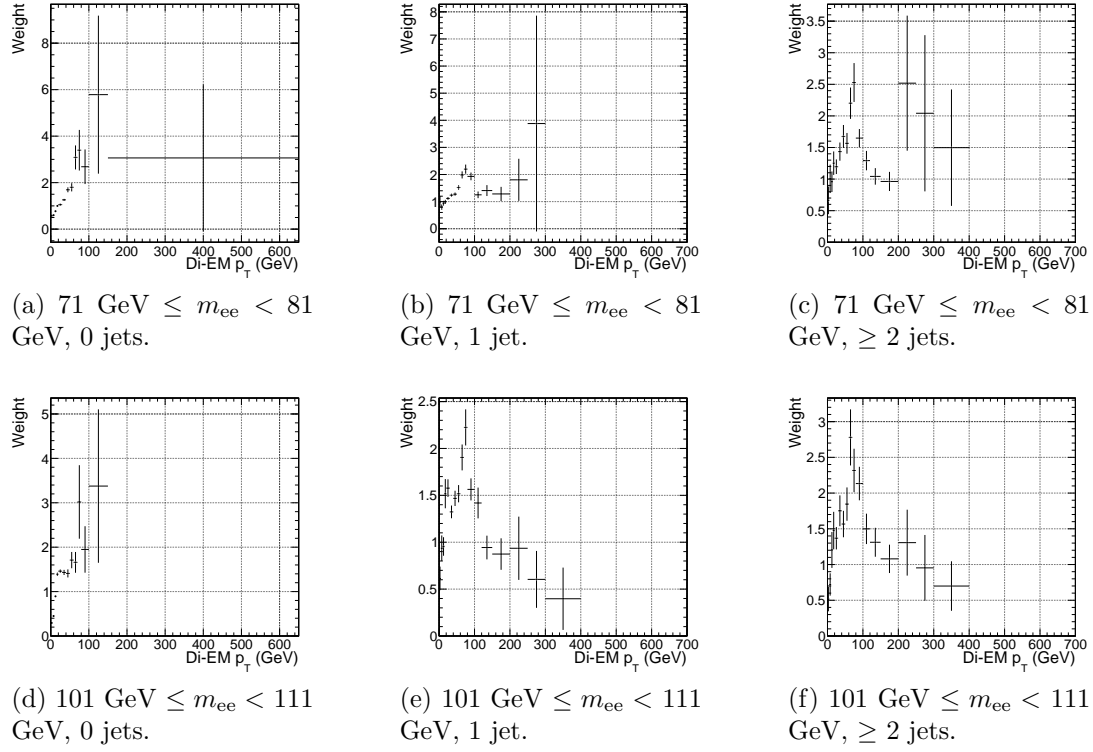


Figure 3.11: ee sideband di-EM p_T weights for events with 0, 1, or ≥ 2 jets (as in Table 2.2). Errors are statistical only.

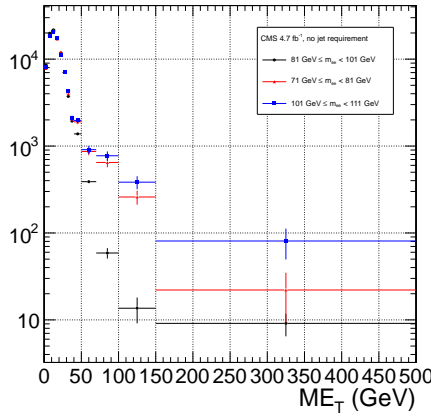


Figure 3.12: E_T spectra of the ee sample for $71 \text{ GeV} \leq m_{ee} < 81 \text{ GeV}$ (red triangles), $81 \text{ GeV} \leq m_{ee} < 101 \text{ GeV}$ (black circles), and $101 \text{ GeV} \leq m_{ee} < 111 \text{ GeV}$ (blue squares). The two sideband distributions (red and blue) and the Z signal distribution (black) are normalized to the total number of $\gamma\gamma$ events. Errors are statistical only.

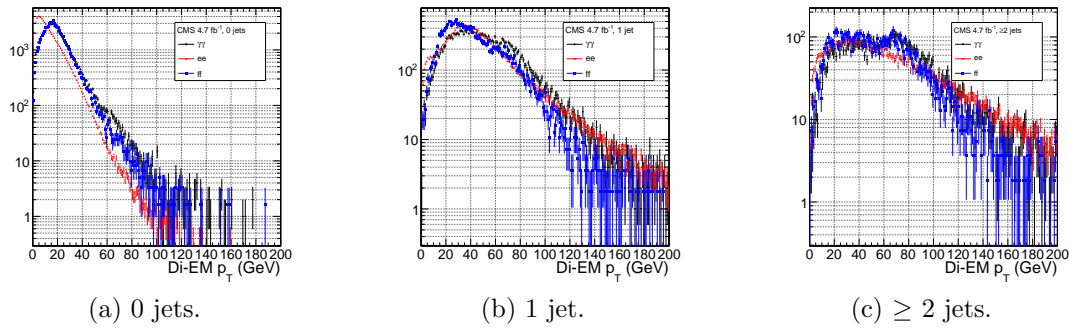


Figure 3.13: ee ($81 \text{ GeV} \leq m_{ee} < 101 \text{ GeV}$) (red triangles), ff (blue squares), and $\gamma\gamma$ (black circles) di-EM p_T spectra for events with 0, 1, or ≥ 2 jets (as in Table 2.2). Errors are statistical only.

945 0, 1, or ≥ 2 jets (as in Table 2.2) are shown in Figure 3.13. Broad humps in the ff
 946 and $\gamma\gamma$ spectra are due to kinematic ΔR and p_T turn-ons that are suppressed in the
 947 ee sample due to the invariant mass cut. Figure 3.14 shows the weights applied to
 948 the ee ($81 \text{ GeV} \leq m_{ee} < 101 \text{ GeV}$) and ff \cancel{E}_T spectra as a function of di-EM p_T and
 949 number of jets per event.

950 3.1.3 Normalization

After reweighting, the \cancel{E}_T distributions of the QCD control samples are normalized to the $\cancel{E}_T < 20$ GeV region of the candidate $\gamma\gamma \cancel{E}_T$ spectrum, where signal contamination is low. The normalization factor is $(N_{\gamma\gamma}^{\cancel{E}_T < 20\text{GeV}} - N_{e\gamma}^{\cancel{E}_T < 20\text{GeV}})/N_{\text{control}}^{\cancel{E}_T < 20\text{GeV}}$, where $N_{e\gamma}^{\cancel{E}_T < 20\text{GeV}}$ is the expected number of electroweak background events with $\cancel{E}_T < 20$ GeV (discussed in Section 3.2).

956 3.2 Modeling the Electroweak Background

⁹⁵⁷ $W\gamma$, $W + \text{jet}$, and $t\bar{t}$ processes in which the W decay electron is misidentified as a
⁹⁵⁸ photon (due to a failure to properly associate a pixel seed to the electron candidate)
⁹⁵⁹ can contribute significantly to the high- \cancel{E}_T tail of the $\gamma\gamma \cancel{E}_T$ spectrum. To estimate

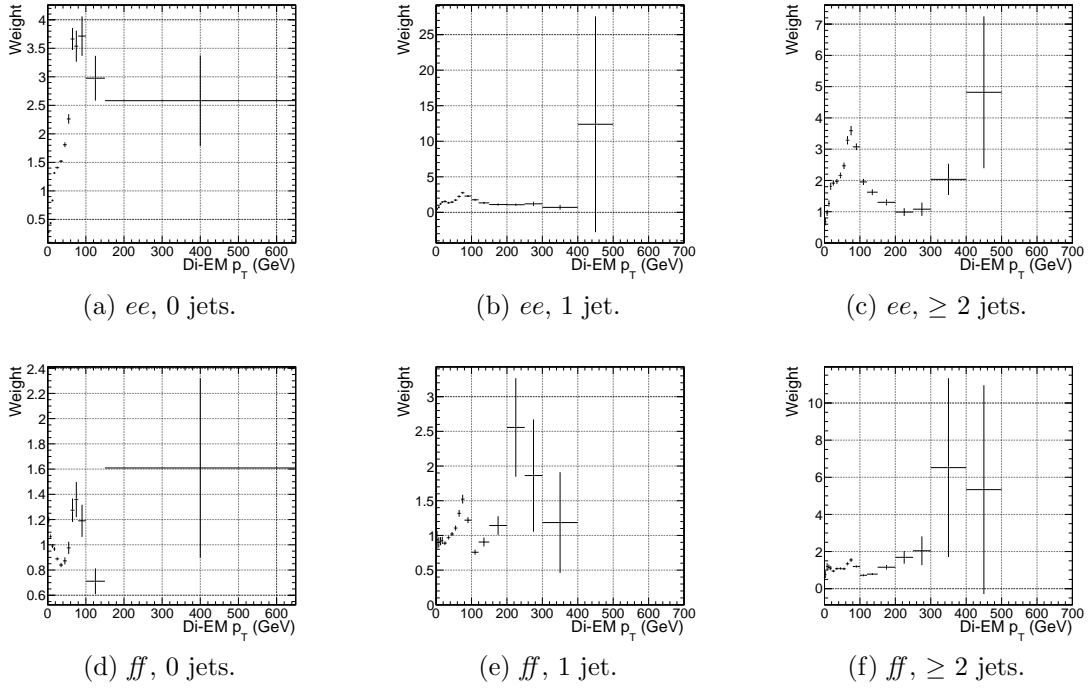


Figure 3.14: ee ($81 \text{ GeV} \leq m_{ee} < 101 \text{ GeV}$) and ff di-EM p_T weights for events with 0, 1, or ≥ 2 jets (as in Table 2.2). Errors are statistical only.

960 this background, the $e\gamma$ sample, which is enriched in $W \rightarrow e\nu$ decays, is scaled by
 961 $f_{e \rightarrow \gamma}/(1 - f_{e \rightarrow \gamma})$, where $f_{e \rightarrow \gamma}$ is the rate at which electrons are misidentified as photons.
 962 The derivation of this scaling factor comes from the two equations

$$N_{e\gamma}^W = f_{e \rightarrow e} N_W \quad (3.2)$$

$$N_{\gamma\gamma}^W = (1 - f_{e \rightarrow e}) N_W \quad (3.3)$$

963 where $N_{e\gamma}^W$ is the number of W events in the $e\gamma$ sample in which the electron was
 964 correctly identified, $f_{e \rightarrow e}$ is the probability to correctly identify an electron, N_W is
 965 the true number of triggered $W \rightarrow e\nu$ events, and $N_{\gamma\gamma}^W$ is the number of W events in
 966 the $\gamma\gamma$ sample in which the electron was misidentified as a photon. The contribution
 967 from $Z \rightarrow ee$ can be neglected (i.e. $f_{e \rightarrow \gamma}$ is small and the Z contribution involves
 968 $f_{e \rightarrow \gamma}^2$, since both electrons have to be misidentified). Since $f_{e \rightarrow e} = 1 - f_{e \rightarrow \gamma}$, solving

969 for $N_{\gamma\gamma}^W$ gives

$$N_{\gamma\gamma}^W = \frac{f_{e\rightarrow\gamma}}{1 - f_{e\rightarrow\gamma}} N_{e\gamma}^W \quad (3.4)$$

970 $f_{e\rightarrow\gamma}$ is measured by fitting the Z peaks in the ee and $e\gamma$ samples. The number of
971 Z events fitted in the ee and $e\gamma$ samples, respectively, is given by

$$N_{ee}^Z = (1 - f_{e\rightarrow\gamma})^2 N_Z \quad (3.5)$$

$$N_{e\gamma}^Z = 2f_{e\rightarrow\gamma}(1 - f_{e\rightarrow\gamma}) N_Z \quad (3.6)$$

972 where N_Z is the true number of triggered $Z \rightarrow ee$ events. Solving for $f_{e\rightarrow\gamma}$ gives

$$f_{e\rightarrow\gamma} = \frac{N_{e\gamma}^Z}{2N_{ee}^Z + N_{e\gamma}^Z} \quad (3.7)$$

973 A Crystal Ball function is used to model the Z signal shape in both the ee and
974 $e\gamma$ samples, while an exponential convoluted with an error function (`RooCMSShape`,
975 see Sec. 2.4.1) is used to model the background shape. The fixed fit parameters are
976 identical for the two samples, but the other parameters are allowed to float indepen-
977 dently. Table 3.3 shows the values and ranges of the fixed and floating fit parameters,
978 respectively.

979 Fits to the ee and $e\gamma$ invariant mass spectra are shown in Figure 3.15. Figure 3.16
980 indicates that the dependence of $f_{e\rightarrow\gamma}$ on the electron p_T and η is small. (Note that all
981 fit parameters are floating in the p_T -dependent fits.) Therefore, a constant misidenti-
982 fication rate (derived from all ee and $e\gamma$ events), rather than a p_T - and η -dependent
983 misidentification rate, is used in the final electroweak background estimate, with the

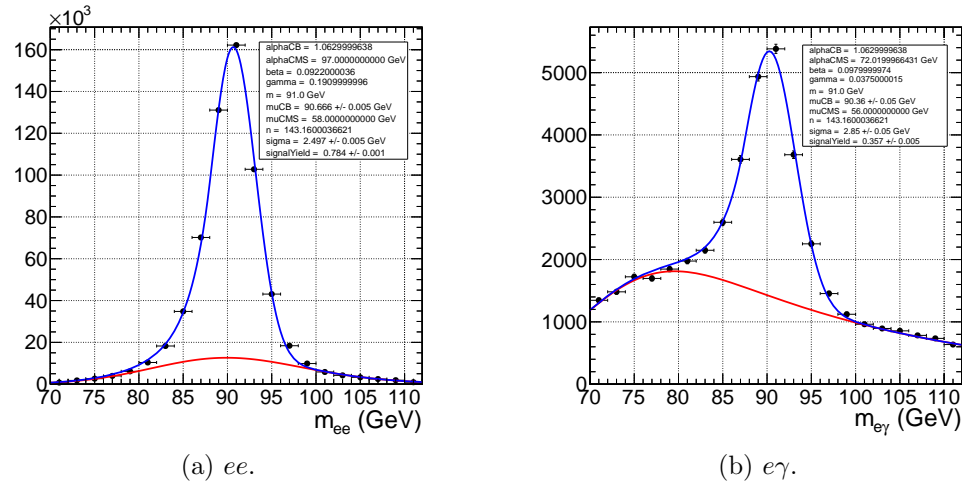


Figure 3.15: Fits to the ee and $e\gamma$ invariant mass spectra using the Crystal Ball RooCMSShape function described in the text and in Table 3.3. The total fit is shown in blue, while the background component is shown in red.

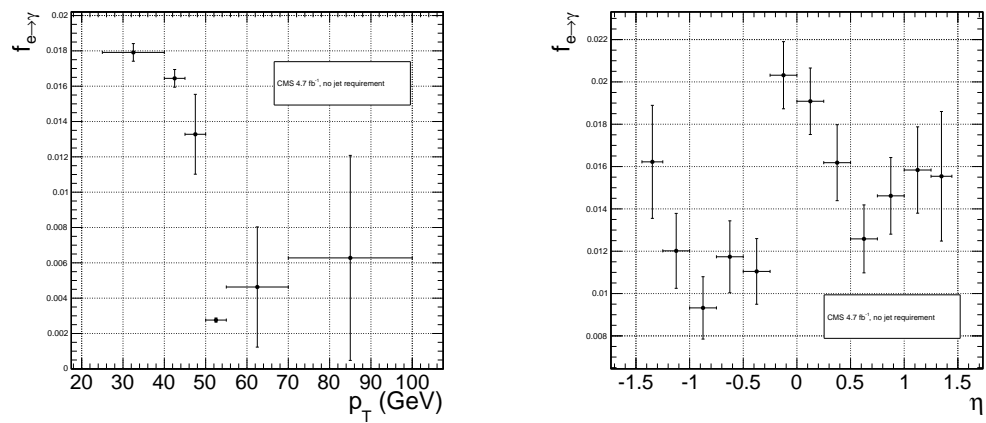
984 difference between the constant rate and the rate for electrons with p_T between 25
 985 and 40 GeV (the range in which the bulk of the trailing photons in the $\gamma\gamma$ sample
 986 lie) taken as a systematic error.

Using the integrals of the Z fits shown in Fig. 3.15, Eq. 3.7, and the p_T systematic discussed above, $f_{e \rightarrow \gamma}$ is calculated to be $0.014 \pm 0.000(\text{stat.}) \pm 0.004(\text{syst.})$. The scaled $e\gamma$ MET distribution is shown in Figure 3.17.

In the 36 pb^{-1} version of this analysis [67], it was shown that the ee sample could accurately predict the QCD and real Z contribution to the $e\gamma$ sample at low \cancel{E}_T , and that the expectation from $W \rightarrow e\nu$ MC accounted for the remaining W contribution at high \cancel{E}_T . A plot of the \cancel{E}_T distributions of the 2010 $e\gamma$ sample and the predicted components is shown in Figure 3.18. This exercise helps to validate both the QCD and electroweak background prediction methods.

Table 3.3: Parameter values for the signal and background PDFs for the ee and $e\gamma$ samples. When a bracketed range is given, the parameter is allowed to float within that range. When a constant is given, the parameter is fixed to that constant.

PDF	Crystal Ball fit parameters				RooCMSShape fit parameters			
	μ	σ	α	n	μ	α	β	γ
ee signal	[86.2, 96.2]	[1.0, 5.0]	1.063	143.16	N/A	N/A	N/A	N/A
$e\gamma$ signal	[86.2, 96.2]	[1.0, 5.0]	1.063	143.16	N/A	N/A	N/A	N/A
ee background	N/A	N/A	N/A	N/A	58	97.0	0.0922	0.191
$e\gamma$ background	N/A	N/A	N/A	N/A	56	72.02	0.098	0.0375



(a) $f_{e \rightarrow \gamma}$ vs. electron p_T . For the lowest p_T bin, the fit to the $e\gamma$ spectrum does not converge well, so the Z signal fraction is fixed to the value in Fig. 3.15b.

(b) $f_{e \rightarrow \gamma}$ vs. electron η .

Figure 3.16: $f_{e \rightarrow \gamma}$ vs. electron p_T and η .

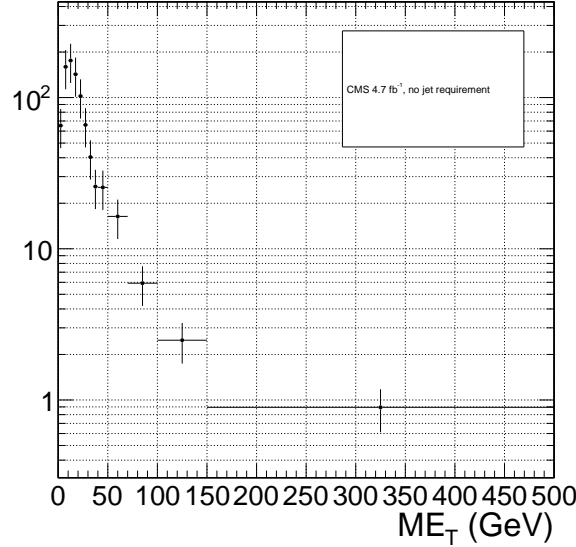


Figure 3.17: E_T spectrum of the $e\gamma$ sample after scaling by $f_{e \rightarrow \gamma}$. The total error on $f_{e \rightarrow \gamma}$ is propagated to the total error on the electroweak background estimate.

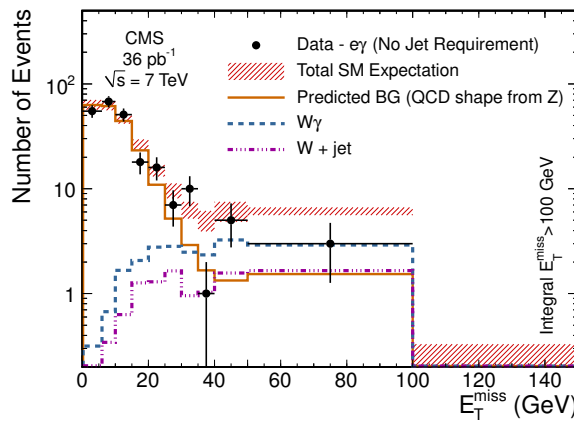


Figure 3.18: E_T spectrum of the $e\gamma$ sample in 36 pb^{-1} of 2010 LHC data scaled by the 2010 measured $f_{e \rightarrow \gamma}$ (black dots), QCD and real Z predicted background from the 2010 ee sample (solid orange line), MC $W + \text{jet}$ estimate (dash-dotted purple line), and MC $W\gamma$ estimate (dashed blue line). The total $e\gamma$ prediction (red band) is the sum of the ee , $W + \text{jet}$, and $W\gamma$ predictions. Reprinted from Fig. 2 of ref. [67].

996 3.3 Errors on the Background Prediction

997 The statistical error on the final background estimate in a particular \cancel{E}_T bin comes
 998 from three sources: the number of control sample events collected in that bin, the
 999 statistical error on the weights applied to events in that bin, and the statistics of the
 1000 normalization region. In the case of the ee control sample, there are contributions
 1001 from the statistics of the m_{ee} sidebands as well.

1002 In order to estimate the statistical error due to the reweighting procedure, 1000
 1003 toy sets of weights are generated. Each set includes a weight for each (di-EM p_T , N_j)
 1004 bin, with the values picked from a Gaussian distribution with mean and standard
 1005 deviation equal to the observed weight for that bin and its statistical error. The effect
 1006 of reweighting error is not correlated between \cancel{E}_T bins. For each of the 1000 exper-
 1007 iments, the control sample data are reweighted according to the generated weights,
 1008 and the background estimates are calculated for each \cancel{E}_T bin. Since the distribution
 1009 of the toy background estimates follows a Gaussian distribution in each \cancel{E}_T bin, the
 1010 RMS spread of the estimates is taken as the statistical error due to reweighting. This
 1011 procedure is carried out for the ff , ee , low sideband ee , and high sideband ee samples.

1012 The total statistical error on the background estimate per \cancel{E}_T bin is given by

$$\sigma_{\text{stat}}^2 = \sigma_{\text{stat,QCD}}^2 + \sigma_{\text{stat,EW}}^2 \quad (3.8)$$

1013 where $\sigma_{\text{stat,QCD}}^2$ is the square of the total statistical error on the QCD prediction in
 1014 the \cancel{E}_T bin

$$\sigma_{\text{stat,QCD}}^2 = \sigma_{\text{stat},s}^2 + \sigma_{\text{Poisson,QCD}}^2 + \sigma_{\text{reweight},s}^2 + \sigma_{\text{reweight,QCD}}^2 \quad (3.9)$$

and $\sigma_{\text{stat,EW}}$ is the Poisson error on the number of $e\gamma$ events in the \cancel{E}_T bin ($= \sqrt{N_{e\gamma}}$, where $N_{e\gamma}$ is the prediction in the \cancel{E}_T bin after scaling by $f_{e\rightarrow\gamma}$). The contributions to $\sigma_{\text{stat,QCD}}^2$ are discussed below.

- $\sigma_{\text{stat},s}^2$ is the statistical error contributed by the normalization factor s (i.e. from Poisson error in the normalization region $\cancel{E}_T < 20$ GeV):

$$\begin{aligned}\sigma_{\text{stat},s}^2 = & \frac{N_{\text{control}}^2}{(N_{\gamma\gamma}^{\text{norm}} - N_{e\gamma}^{\text{norm}})^2} (\sigma_{\text{Poisson},\gamma\gamma}^{\text{norm}})^2 + (\sigma_{\text{Poisson},e\gamma}^{\text{norm}})^2 + \\ & \frac{N_{\text{control}}^2}{(N_{\text{control}}^{\text{norm}})^2} (\sigma_{\text{Poisson,control}}^{\text{norm}})^2\end{aligned}\quad (3.10)$$

where N_{control} is the number of reweighted, normalized events in the \cancel{E}_T bin, $N_{\gamma\gamma}^{\text{norm}}$ is the number of $\gamma\gamma$ events in the normalization region, $N_{e\gamma}^{\text{norm}}$ is the number of $e\gamma$ events in the normalization region (after scaling by $f_{e\rightarrow\gamma}$), $\sigma_{\text{Poisson},\gamma\gamma}^{\text{norm}}$ is the Poisson error on the number of $\gamma\gamma$ events in the normalization region ($= \sqrt{N_{\gamma\gamma}^{\text{norm}}}$), $\sigma_{\text{Poisson},e\gamma}^{\text{norm}}$ is the Poisson error on the number of $e\gamma$ events in the normalization region ($= \sqrt{N_{e\gamma}^{\text{norm}}}$), $N_{\text{control}}^{\text{norm}}$ is the number of QCD control (ee or ff) events in the normalization region, and $\sigma_{\text{Poisson,control}}^{\text{norm}}$ is the Poisson error on the number of QCD control (ee or ff) events in the normalization region ($= \sqrt{\sum_{i=1}^{N_{\text{control}}^{\text{norm}}} w_i^2}$, where w_i is the di-EM p_T weight applied to event i). For the ee control region, N_{control} and $N_{\text{control},\text{norm}}$ are sideband subtracted, and $\sigma_{\text{Poisson,control}}^{\text{norm}}$ includes the Poisson error on the number of sideband events.

- $\sigma_{\text{Poisson,QCD}}$ is the Poisson error due to the number of QCD control (ee or ff) events in the \cancel{E}_T bin, equal to $\sqrt{\sum_{i=1}^{N_{\text{control}}^{\text{norm}}} w_i^2}$, where w_i is the di-EM p_T weight applied to event i . For the ee control region, $\sigma_{\text{Poisson,QCD}}$ includes the Poisson error on the number of subtracted sideband events.
- $\sigma_{\text{reweight},s}$ is the error contributed by the control sample reweighting in the nor-

1036 malization region ($= \frac{N_{\text{control}}^2}{(N_{\text{control}}^{\text{norm}})^2} \sigma_{\text{reweight,control}}^{\text{norm}}$). $\sigma_{\text{reweight,control}}^{\text{norm}}$ is the quadrature
 1037 sum of the RMS of the 1000 toy reweighting experiments for each \cancel{E}_T bin in the
 1038 normalization region. For the ee control sample, it also includes (in quadrature)
 1039 the RMS of the toys in the sideband samples.

- 1040 • $\sigma_{\text{reweight,QCD}}$ is the error contributed by the control sample reweighting in the \cancel{E}_T
 1041 bin ($= s\sigma_{\text{reweight,control}}$). $\sigma_{\text{reweight,control}}$ is the RMS of the 1000 toy reweighting
 1042 experiments for the E_T bin. For the ee control sample, it also includes (in
 1043 quadrature) the RMS of the toys in the sideband samples.

1044 The dominant source of systematic error on the background estimate is the slight
 1045 difference in hadronic activity between the ee , ff , and $\gamma\gamma$ samples. This results in a
 1046 small bias (~ 1 GeV) of the ee \cancel{E}_T distribution towards lower values with respect to
 1047 the ff and $\gamma\gamma$ samples, as shown in Figure 3.19. Therefore, the ff sample is used as
 1048 the primary QCD background estimator, and the difference between the ee and ff
 1049 predictions is assigned as an error on the knowledge of the hadronic activity. For \cancel{E}_T
 1050 > 100 GeV, this error amounts to 43% of the total QCD + electroweak background
 1051 estimate.

1052 The second largest source of systematic error comes from the p_T dependence of the
 1053 $e \rightarrow \gamma$ misidentification rate (see 3.2). For $\cancel{E}_T > 100$ GeV, the expected electroweak
 1054 background is 3.4 ± 1.0 events, so this error amounts to 4.8% of the total QCD +
 1055 electroweak background estimate.

1056 The assumption of a constant $t\bar{t}$ and $W + \text{jets}$ background shape under the Z
 1057 peak in the ee sample induces a systematic error on the ee sideband-subtracted back-
 1058 ground prediction. To assess the magnitude of this error, the sideband subtraction
 1059 (see Sec. 3.1.2) is performed once using only the prediction from the high sideband,
 1060 and once using only the prediction from the low sideband. In each of these cases, the
 1061 prediction is weighted by a factor of two, to account for the fact that the sideband
 1062 regions are only half as wide (10 GeV) as the signal region (20 GeV). The maximum

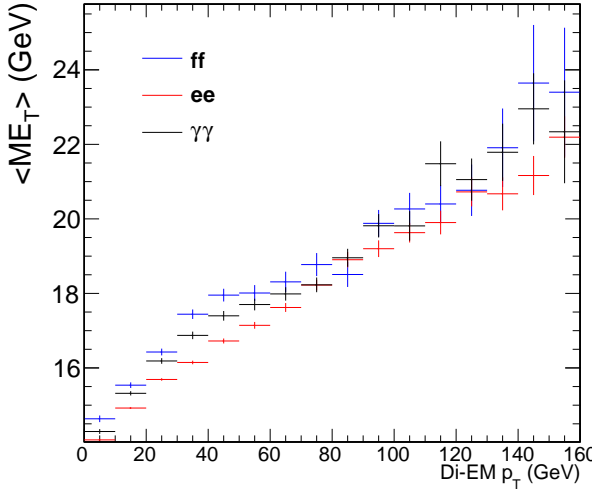


Figure 3.19: Average E_T vs. di-EM p_T for the ff (blue), ee (red), and $\gamma\gamma$ (black) samples.

1063 variation from the nominal ee estimate is taken as the error, which amounts to 11%
 1064 for $E_T > 100$ GeV. E_T distributions using the nominal ee sideband subtraction, the
 1065 low-sideband-only subtraction, and the high-sideband-only subtraction are shown in
 1066 Figure 3.20.

Added

1067 Finally, the few percent error on the jet energy correction factors introduces an this
 1068 error on the final background estimate through (a) the use of the PF p_T to measure para-
 1069 the di-EM p_T , (b) the counting of jets passing a 30 GeV p_T threshold for placement of graph
 1070 the event in an N_j bin for reweighting, and (c) the counting of jets above threshold for
 1071 the ≥ 1 -jet version of the selection. To estimate this error, 100 pseudo-experiments
 1072 are generated with identical properties as the true data sample, except with corrected
 1073 jet energies (in all events) all shifted by an amount $r\sigma(p_T, \eta)$. r is a random number
 1074 drawn from a Gaussian distribution with mean 0 and width 1, and $\sigma(p_T, \eta)$ is the
 1075 uncertainty on the jet energy correction factor (which, like the correction factor itself,
 1076 is a function of p_T and η). The same factor r is applied to all jets in all events in the
 1077 pseudo-experiment because the jet energy correction errors are correlated from jet to
 1078 jet (they result from e.g. uncertainties in MC simulation or uncertainties in ECAL

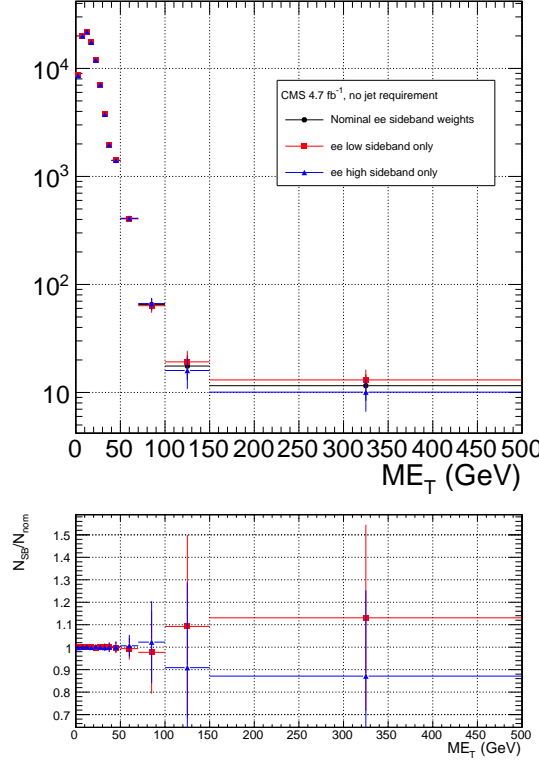


Figure 3.20: ee E_T distributions using the nominal sideband subtraction (black circles), low sideband only (red squares), and high sideband only (blue triangles). The bottom plot shows the ratio of the low sideband distribution to the nominal (red squares) and the ratio of the high sideband distribution to the nominal (blue triangles).

1079 energy scale [47]). The standard error of the mean of the 100 resulting background
1080 estimates in each relevant E_T bin is taken as the error. The error in each E_T bin is
1081 assumed to be uncorrelated. This process is repeated for both the inclusive and ≥ 1 -
1082 jet selections. For $E_T \geq 100$ GeV, the jet energy correction uncertainty is 1.5% (2.2%)
1083 of the total background for the inclusive (≥ 1 -jet) selection.

1084 The uncertainty in how to define the (di-EM p_T , N_j) bins, especially at high di-
1085 EM p_T where the statistics are low, is covered by the 1000-toys procedure as long as
1086 the bins are not too coarse. This is shown in Figure 3.21. If the bins are too coarse,
1087 the details of the shape of the di-EM p_T spectra are lost, and the reweighting has a
1088 smaller effect.

1089 The use of uncorrected instead of corrected PF E_T (see Sec. 2.1.3) makes no

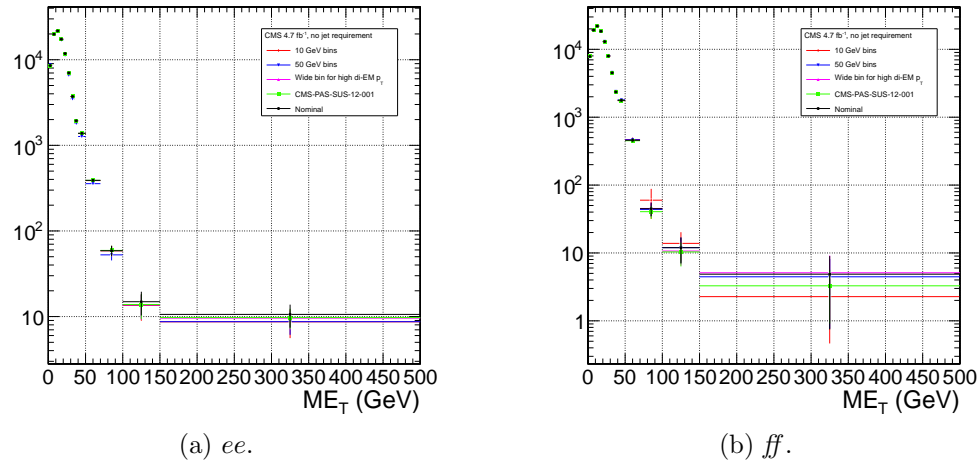


Figure 3.21: Comparison of \cancel{E}_T distributions for five different di-EM p_T bin definitions: uniform bins of width 10 GeV (red diamonds); uniform bins of width 50 GeV (blue downward-pointing triangles); bins with lower edges $\{0.0, 5.0, 10.0, 15.0, 20.0, 30.0, 40.0, 50.0, 60.0, 70.0, 80.0, 100.0, 750.0\}$ GeV for 0-jet events and $\{0.0, 5.0, 10.0, 15.0, 20.0, 30.0, 40.0, 50.0, 60.0, 70.0, 80.0, 100.0, 150.0\}$ GeV for ≥ 1 -jet events (magenta upward-pointing triangles), i.e. a single wide bin at high di-EM p_T ; bins with lower edges $\{0.0, 5.0, 10.0, 15.0, 20.0, 30.0, 40.0, 50.0, 60.0, 70.0, 80.0, 100.0, 150.0\}$ GeV for 0-jet events and $\{0.0, 5.0, 10.0, 15.0, 20.0, 30.0, 40.0, 50.0, 60.0, 70.0, 80.0, 100.0, 120.0, 150.0, 200.0\}$ GeV for ≥ 1 -jet events (green squares), i.e. the bins used in ref. [19]; and the nominal bin definitions shown in Fig. 3.14 (black circles).

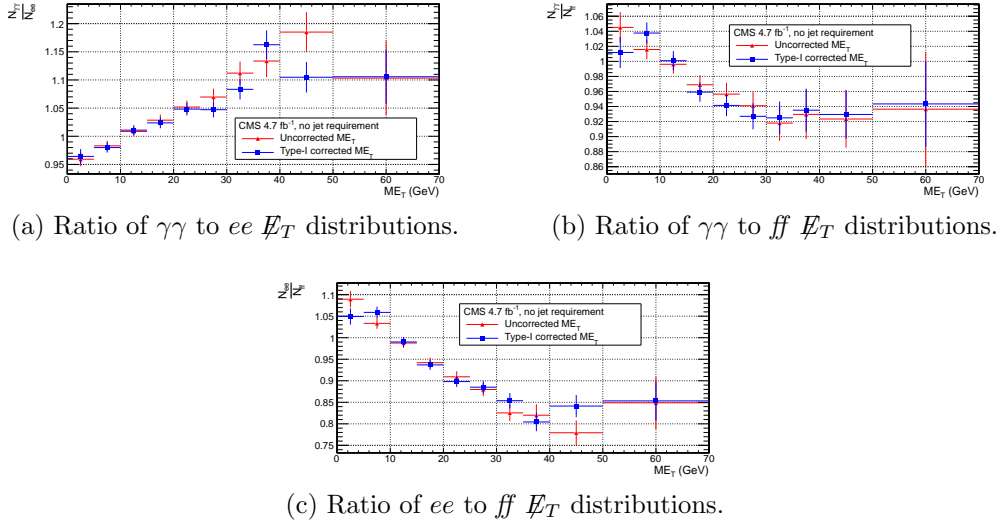


Figure 3.22: Agreement between $\gamma\gamma$, ee , and ff samples for uncorrected (red triangles) and corrected (blue squares) \not{E}_T .

difference in the agreement of the background predictions and the search sample in a control region at low \not{E}_T , as shown in Figure 3.22. Since the control samples are derived from the same data as the search sample, any biases in the \not{E}_T reconstruction due to jet energy scale are present equally in both samples.

Tables 3.4 and 3.5 list all the errors on the ee and ff QCD background predictions, respectively, for the \not{E}_T bins used in the search. Table 3.6 lists the errors on the electroweak background prediction. Finally, Table 3.7 shows the errors on the total QCD + electroweak background prediction, broken down by origin (statistical or systematic) and QCD background estimation sample (ee or ff). In the final result, only the ff QCD estimate is used.

1100 3.4 Results

Figure 3.23(3.24) shows the \not{E}_T distribution of the inclusive(≥ 1 -jet) $\gamma\gamma$ search sample along with the predicted \not{E}_T distributions of the QCD and electroweak backgrounds. The observed number of two-photon events, background estimates and their errors,

Table 3.4: Errors on the ee QCD background prediction as a fraction of the ee prediction.

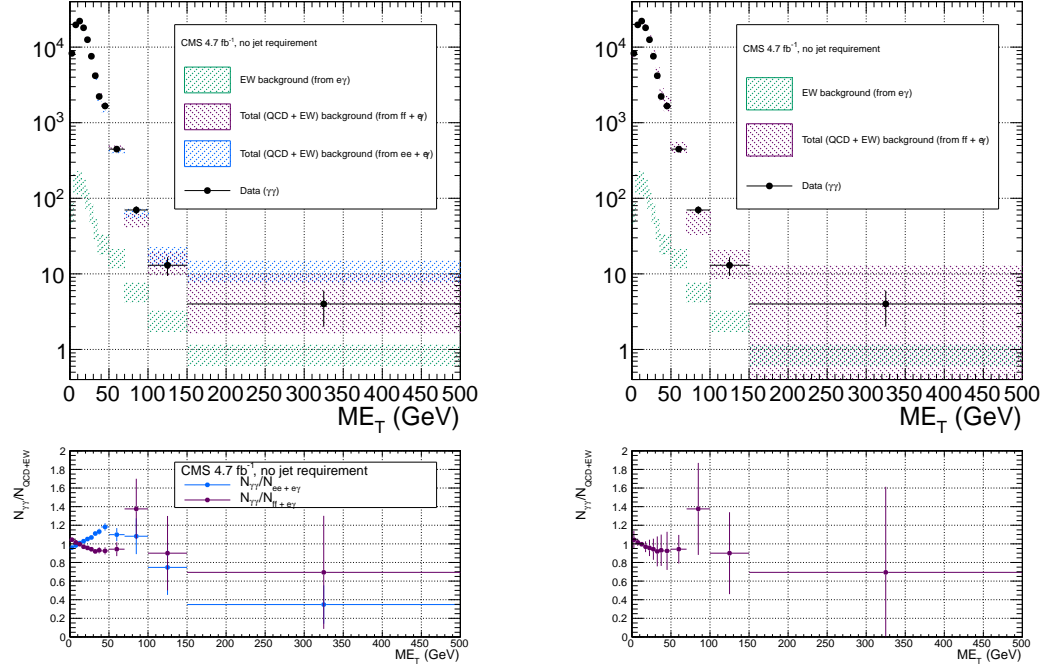
Source of error	Fractional uncertainty (%)				
	[50, 60)	[60, 70)	[70, 80)	[80, 100)	≥ 100
Total	3.9	8.1	16	25	25
Statistics	3.6	7.8	16	24	22
No. events	3.6	7.7	15	24	20
In norm. region	0.43	0.44	0.46	0.55	0.51
In this E_T bin	3.5	7.7	15	24	20
Reweighting	0.73	1.2	3.5	4.3	7.7
In norm. region	0.19	0.19	0.2	0.24	0.23
In this E_T bin	0.71	1.2	3.5	4.3	7.7
Systematics	2.6	4.4	1.2	7.5	14
$f_{e \rightarrow \gamma}$ (in norm. region)	0.0012	0.0012	0.0013	0.0015	0.0014
m_{ee} background shape	1.4	2	0.72	5.5	12
Jet energy scale	2.2	3.9	0.96	5.1	6.9

Table 3.5: Errors on the ff QCD background prediction as a fraction of the ff prediction.

Source of error	Fractional uncertainty (%)				
	[50, 60)	[60, 70)	[70, 80)	[80, 100)	≥ 100
Total	15	25	61	34	64
Statistics	7.2	14	30	33	38
No. events	7.1	14	29	33	36
In norm. region	0.64	0.64	0.64	0.64	0.64
In this E_T bin	7.1	14	29	33	36
Reweighting	0.85	2.7	5.1	6.9	13
In norm. region	0.27	0.27	0.27	0.27	0.27
In this E_T bin	0.81	2.6	5.1	6.9	13
Systematics	13	21	53	6.6	52
ee/ff difference	13	21	53	5.5	52
$f_{e \rightarrow \gamma}$ (in norm. region)	0.0012	0.0012	0.0012	0.0012	0.0012
Jet energy scale	0.099	1.7	1.8	3.5	1.8

Table 3.6: Errors on the $e\gamma$ electroweak background prediction as a fraction of the $e\gamma$ prediction.

Source of error	Fractional uncertainty (%)				
	[50, 60)	[60, 70)	[70, 80)	[80, 100)	≥ 100
Total	29	29	30	30	30
Statistics	3.6	5.2	6.7	7.2	6.5
Systematics ($f_{e \rightarrow \gamma}$)	29	29	29	29	29



(a) $ee + e\gamma$ and $ff + e\gamma$. The widths of the bands correspond to the errors given in Table 3.7, excluding the error associated with the difference between the ee and ff QCD estimates for the $ff + e\gamma$ E_T distribution.

(b) $ff + e\gamma$. The widths of the bands correspond to the errors given in Table 3.7, including the error associated with the difference between the ee and ff QCD estimates.

Figure 3.23: E_T distribution of the $\gamma\gamma$ search sample (black circles) along with the predicted E_T distributions of the QCD and electroweak backgrounds (blue band for ee QCD prediction + electroweak prediction, purple band for ff QCD prediction + electroweak prediction). The electroweak background prediction is shown in green. The bottom plots show the ratio of the $\gamma\gamma E_T$ distribution to the $ee + e\gamma$ background distribution (blue) and $ff + e\gamma$ background distribution (purple).

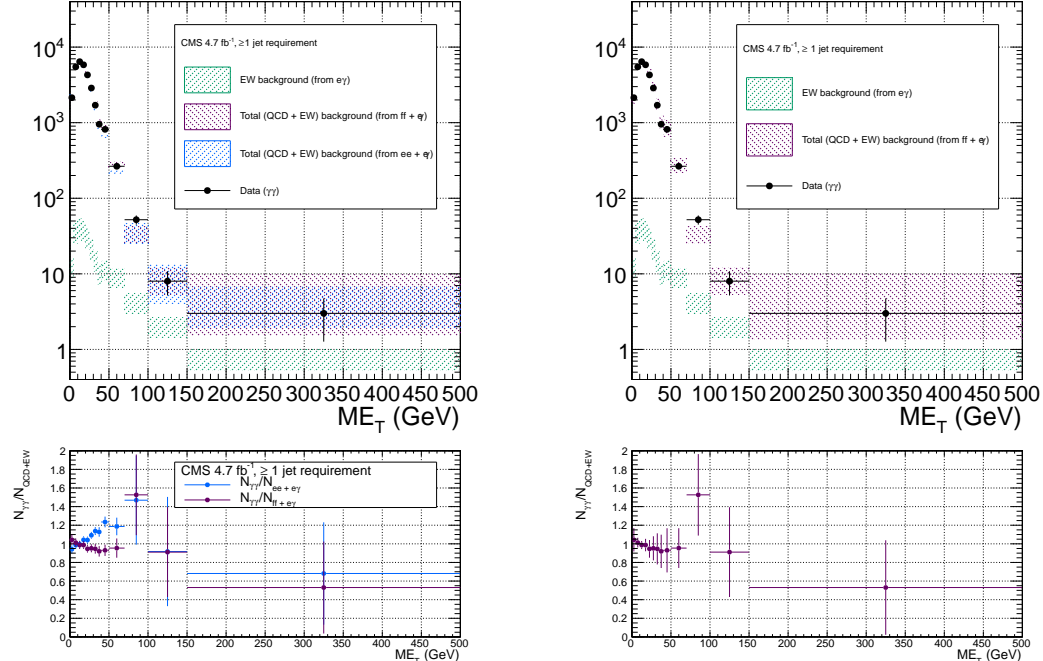
and expected number of inclusive(≥ 1 -jet) two-photon events from two representative GGM SUSY models are listed in Table 3.8(3.9). (Details of the SUSY MC production are given in Chapter 4 and App. A.) No deviation from the Standard Model prediction is observed in the $\gamma\gamma$ search sample.

Table 3.7: Errors on the total QCD + electroweak background prediction as a fraction of the total prediction.

Source of error	Fractional uncertainty (%)				
	[50, 60)	[60, 70)	[70, 80)	[80, 100)	≥ 100
Total ($ee + e\gamma$)	3.9	7.8	15	22	22
Statistics	3.4	7.3	14	21	18
QCD	3.4	7.3	14	21	18
Electroweak	0.13	0.3	0.53	0.79	0.76
Systematics	2.7	4.5	2.6	7.4	13
QCD	2.5	4.1	1.1	6.7	12
Electroweak	1	1.7	2.3	3.2	3.4
Total ($ff + e\gamma$)	14	24	54	30	54
Statistics	6.9	13	26	29	30
QCD	6.9	13	26	29	30
Electroweak	0.11	0.24	0.79	0.83	1.1
Systematics	12	20	47	6.7	43
QCD	12	20	47	5.8	43
Electroweak	0.9	1.3	3.4	3.4	4.8

Table 3.8: Observed numbers of two-photon events, background estimates and their errors, and expected numbers of two-photon events from two representative GGM SUSY models (details of MC simulation given in Chapter 4 and App. A) for the E_T bins used in the search. Errors on the background estimates are detailed in Tables 3.4, 3.5, 3.6, and 3.7. Errors on the expected numbers of GGM events are purely statistical.

Source	No. events				
	[50, 60)	[60, 70)	[70, 80)	[80, 100)	≥ 100
Observation ($\gamma\gamma$)	354	93	37	33	17
Predicted background ($ff + e\gamma$)	361 ± 51.5	113 ± 27.1	26.9 ± 14.5	23.9 ± 7.23	20.2 ± 10.9
$m_{\tilde{q}} = 720$ GeV $M_3 = 720$ GeV $M_1 = 375$ GeV	13.3 ± 2.13	17.7 ± 2.46	15.3 ± 2.33	42.9 ± 3.82	966 ± 18.3
$m_{\tilde{q}} = 1440$ GeV $M_3 = 1440$ GeV $M_1 = 375$ GeV	0.008 ± 0.003	0.009 ± 0.003	0.012 ± 0.003	0.030 ± 0.005	1.92 ± 0.04



(a) $ee + e\gamma$ and $ff + e\gamma$. The widths of the bands correspond to the errors given in Table 3.7, excluding the error associated with the difference between the ee and ff QCD estimates for the $ff + e\gamma$ E_T distribution.

(b) $ff + e\gamma$. The widths of the bands correspond to the errors given in Table 3.7, including the error associated with the difference between the ee and ff QCD estimates.

Figure 3.24: E_T distribution of the $\gamma\gamma + \geq 1$ jet search sample (black circles) along with the predicted E_T distributions of the QCD and electroweak backgrounds (blue band for ee QCD prediction + electroweak prediction, purple band for ff QCD prediction + electroweak prediction). The electroweak background prediction is shown in green. The bottom plots show the ratio of the $\gamma\gamma E_T$ distribution to the $ee + e\gamma$ background distribution (blue) and $ff + e\gamma$ background distribution (purple).

Table 3.9: Observed numbers of two-photon + ≥ 1 -jet events, background estimates and their errors, and expected numbers of two-photon + ≥ 1 -jet events from two representative GGM SUSY models (details of MC simulation given in Chapter 4 and App. A) for the \cancel{E}_T bins used in the search. Errors on the background estimates are detailed in Tables 3.4, 3.5, 3.6, and 3.7. Errors on the expected numbers of GGM events are purely statistical.

Source	No. events				
	[50, 60)	[60, 70)	[70, 80)	[80, 100)	≥ 100
Observation ($\gamma\gamma + \geq 1$ jet)	202	63	27	25	11
Predicted background ($ff + e\gamma$)	200 ± 35.4	77.7 ± 28.1	19.4 ± 8.55	14.7 ± 7.04	14.4 ± 5.59
$m_{\tilde{q}} = 720$ GeV $M_3 = 720$ GeV $M_1 = 375$ GeV	13.3 ± 2.13	17.7 ± 2.46	15.3 ± 2.33	42.9 ± 3.82	965 ± 18.3
$m_{\tilde{q}} = 1440$ GeV $M_3 = 1440$ GeV $M_1 = 375$ GeV	0.008 ± 0.003	0.009 ± 0.003	0.012 ± 0.003	0.031 ± 0.004	1.92 ± 0.04

₁₁₀₈ **Chapter 4**

₁₁₀₉ **Interpretation of Results in Terms**
₁₁₁₀ **of GMSB Models**

₁₁₁₁ As shown in Figs. 3.23 and 3.24 and Tables 3.8 and 3.9, no excess of events above
₁₁₁₂ the Standard Model expectation is found in either the ≥ 0 - or ≥ 1 -jet analyses for the
₁₁₁₃ GMSB-sensitive region $\cancel{E}_T \geq 50$ GeV. Therefore, upper limits on the production cross
₁₁₁₄ sections of various GMSB models are calculated and then translated into statements of
₁₁₁₅ exclusion. Section 4.1 describes the GMSB models that were generated with MC and
₁₁₁₆ tested for exclusion. The upper limit calculation and translation to model exclusions
₁₁₁₇ is laid out in Section 4.2. The upper limits themselves are presented in Section 4.3,
₁₁₁₈ and, finally, the exclusions are presented in Section 4.4.

₁₁₁₉ **4.1 Simplified Models**

₁₁₂₀ The exclusion reach of the two-photon search is presented for three different two-
₁₁₂₁ dimensional scans in GMSB parameter space. The first scan covers the bino NLSP
₁₁₂₂ scenario of Sec. 1.5. In this scan, M_2 , which controls the amount of wino mixing, is
₁₁₂₃ set to 3.5 TeV. M_1 , which controls the amount of bino mixing, is set to 375 GeV.
₁₁₂₄ This insures that all gauginos except the lightest neutralino are too heavy to be

produced in significant numbers at the LHC. All other mass parameters except for
 M_3 (\sim gluino mass) and $m_{\tilde{q}}$ (\sim first- and second-generation squark mass) are set to
 3.5 TeV, which insures that squark/gluino decay to intermediate states such as third-
 generation squarks or any flavor of lepton is strongly suppressed. M_3 and $m_{\tilde{q}}$ are
 scanned over from $M_3 = m_{\tilde{q}} = 400$ GeV to $M_3 = m_{\tilde{q}} = 2$ TeV in 80-GeV steps.
 The resulting simplified model consists only of a gluino, first- and second-generation
 squarks, and the lightest neutralino and its decay products (the gravitino is forced to
 be the LSP). The scan in M_3 - $m_{\tilde{q}}$ space illuminates the sensitivity of the two-photon
 search to different levels of signal hadronic activity.

The second scan is identical to the first except that the values of M_1 and M_2
 are inverted ($M_1 = 3.5$ TeV and $M_2 = 375$ GeV). This corresponds to the wino
 NLSP scenario of Sec. 1.5. Now, both the lightest neutralino and the lightest chargino
 have masses of order 375 GeV, and are therefore produced with approximately equal
 frequency in the gluino and squark decays. The chargino decays to $W + \tilde{G}$, so final
 states in this scan often include leptons or large jet multiplicity. Since there is no
 guarantee that two neutralinos will be produced and will decay to two photons, this
 search is not well optimized for the wino NLSP scenario. However, a related CMS
 search with one photon and ≥ 3 jets has an exclusion reach of ~ 1 TeV in M_3 and
 $m_{\tilde{q}}$ for this scenario [19].

The third scan is M_3 vs. M_1 for $m_{\tilde{q}}$, M_2 , and all other mass parameters equal to
 2.5 TeV. M_3 is scanned from 160 GeV to 2 TeV in 80-GeV steps, while M_1 is scanned
 from 150 GeV to 1050 GeV in 100-GeV steps. $M_3 < M_1$ is not allowed, as this would
 imply that the gluino, not the lightest neutralino, is the NLSP. This scan highlights
 the performance of the two-photon search as a function of M_1 (i.e. as a function of
 decays open to the neutralino), whereas the previous two scans keep M_1 fixed.

For each scan, the sparticle mass spectrum is generated with SuSpect 2.41 [78]
 and the decay widths with SDECAY 1.3 [79]. The event data (including produc-

tion, unstable particle decay, parton showering, and hadronization) is generated with
 Pythia 6.422 [83], using the sparticle mass spectra and decay widths as inputs. The
 gravitino is always forced to be the LSP. The simulated data are reconstructed with
 CMSSWv4.2.2, which uses a detector simulation based on GEANT 4 [80]. Next to
 leading order cross sections are calculated with PROSPINO 2.1 [81], and shown in
 Figure 4.1 for the three signal MC scenarios.

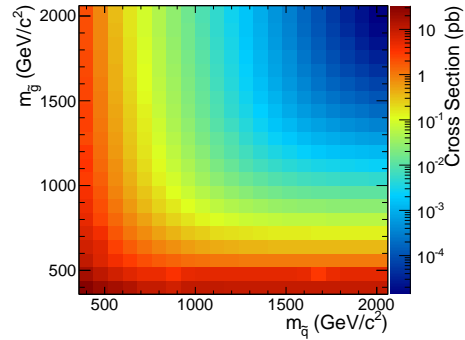
4.2 Upper Limit Calculation and Model Exclusion

The upper limits are calculated according to the prescription followed for the 2011
 ATLAS + CMS Higgs limit combination [68]. This prescription utilizes the frequentist
 CL_s method [69] with profile likelihood test statistic [70]. The CL_s method and the
 profile likelihood are explained in Section 4.2.2, using specific signal MC points to
 illustrate the procedure. First, however, the signal MC acceptance \times efficiency, which
 is an input to the limit setting procedure, is presented in Section 4.2.1.

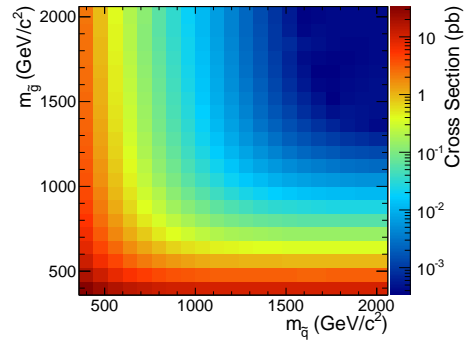
4.2.1 Signal Acceptance \times Efficiency

The signal acceptance \times efficiency (denoted $\mathcal{A} \times \epsilon$), defined for each signal point as
 the number of $\gamma\gamma$ events selected with $\cancel{E}_T \geq 50$ GeV divided by the total number of
 events generated, is shown in Figure 4.2 for the three different scenarios described in
 Sec. 4.1.

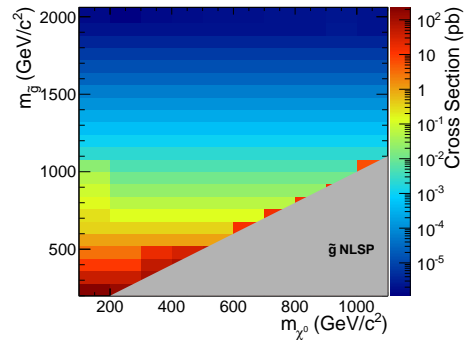
In Figs. 4.2a and 4.2b, the large drop in $\mathcal{A} \times \epsilon$ for $m_{\tilde{q}} > M_3$ is due to an increase
 in the number of jets produced per event and a consequent reduction in the number
 of photons that pass the $I_{\text{comb}} < 6$ GeV cut. For $m_{\tilde{q}} > M_3$, there is more phase space
 available to produce gluinos in the hard scatter than squarks. However, since gluinos
 must decay via squarks, and in these models all squarks are heavier than the gluino,
 only the two-jet decay $\tilde{g} \rightarrow qq\tilde{\chi}^0$ is available. Conversely, when $m_{\tilde{q}} < M_3$, there is



(a) M_2 decoupled ($M_2 = 3.5$ TeV), $M_1 = 375$ GeV, M_3 vs. $m_{\tilde{q}}$.



(b) M_1 decoupled ($M_1 = 3.5$ TeV), $M_2 = 375$ GeV, M_3 vs. $m_{\tilde{q}}$.



(c) $m_{\tilde{q}}$ decoupled ($m_{\tilde{q}} = 2.5$ TeV), M_3 vs. M_1 .

Figure 4.1: Next to leading order cross sections for the three different MC scenarios described in the text.

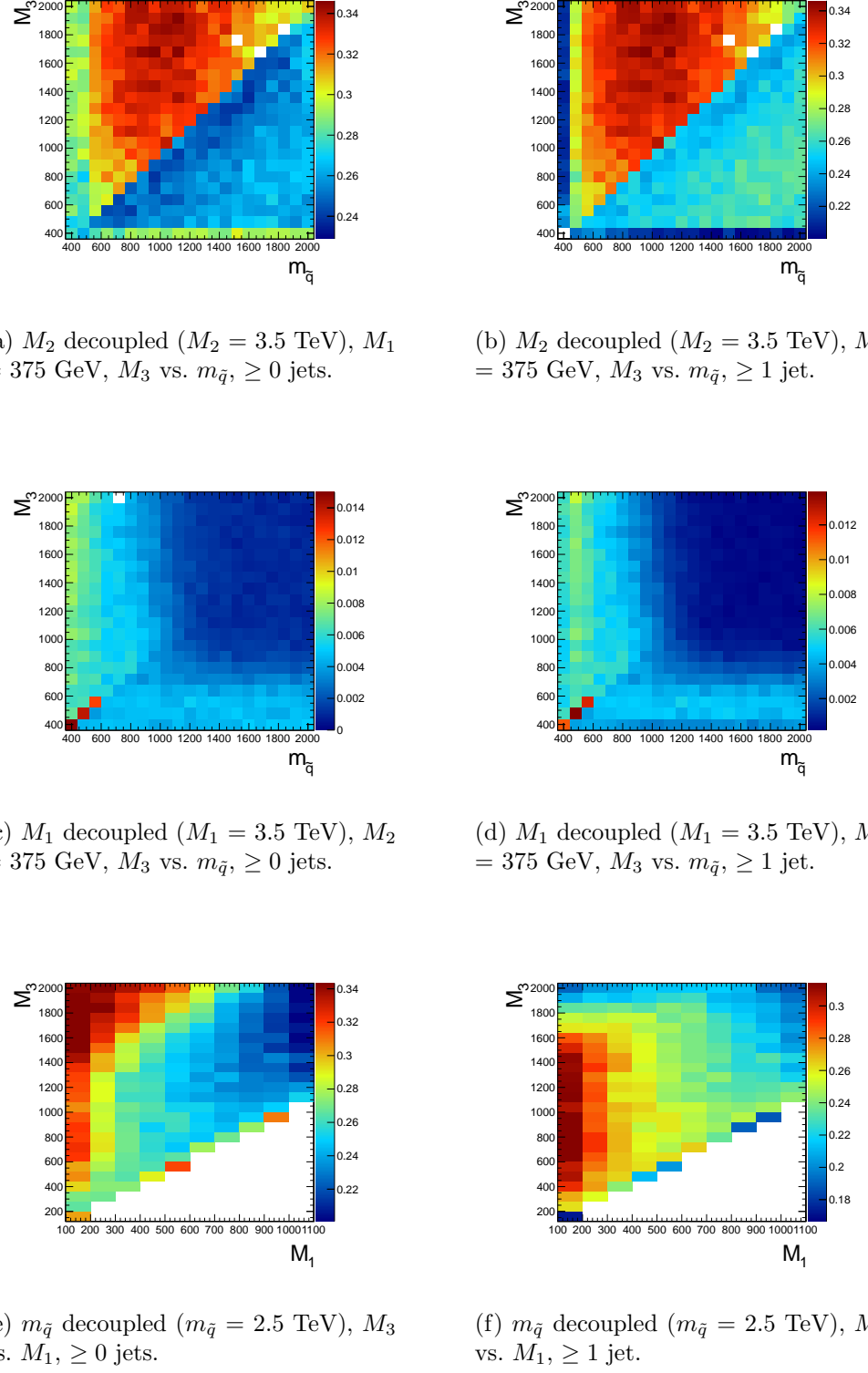


Figure 4.2: Signal acceptance \times efficiency (defined in the text) for the three different scenarios described in Sec. 4.1.

1176 more phase space available to produce squarks, which may then decay via one jet as
 1177 $\tilde{q} \rightarrow q\tilde{\chi}^0$. Jets in SUSY events may be very close to the neutralino decay photons,
 1178 and as a result the photons may fail the strict isolation requirements, leading to lower
 1179 $\mathcal{A} \times \epsilon$ for jet-rich events. The worsened acceptance along $M_3 = 400$ GeV and $m_{\tilde{q}} = 400$
 1180 GeV in Fig. 4.2b is due to efficiency of the jet cut, which decreases drastically as M_3
 1181 and $m_{\tilde{q}}$ approach M_1 because of shrinking phase space to produce hard jets in the
 1182 squark and gluino decays to neutralinos.

1183 The broad peak in $\mathcal{A} \times \epsilon$ shown in Fig. 4.2a for $m_{\tilde{q}} < M_3$ and ~ 600 GeV $< m_{\tilde{q}} <$
 1184 ~ 1600 GeV is due to the $\cancel{E}_T > 50$ GeV cut. The efficiency of the cut decreases
 1185 as $m_{\tilde{q}}$ decreases because of the fixed M_1 of 375 GeV. If the squark-neutralino mass
 1186 splitting gets too small, the likelihood of producing an energetic enough gravitino to
 1187 pass the \cancel{E}_T cut decreases.

1188 $\mathcal{A} \times \epsilon$ is generally much lower for the $M_2 = 375$ GeV grid (Figs. 4.2c and 4.2d)
 1189 due to the larger contribution from chargino decays to $W + \tilde{G}$, which do not give rise
 1190 to photons in the final state. The increased acceptance for $M_3 > m_{\tilde{q}}$ is due to the
 1191 same jet multiplicity issue affecting the $M_1 = 375$ GeV grid. As M_3 and $m_{\tilde{q}}$ increase
 1192 relative to the fixed M_2 , the jets from squark and gluino decay get more energetic,
 1193 increasing the chance that they will overlap with the neutralino decay photon and
 1194 cause it to fail the isolation cut. For $m_{\tilde{q}} \gtrsim 1$ TeV and $M_3 \gtrsim 800$ GeV, the acceptance
 1195 is so low that not enough events were simulated to see the acceptance decrease over
 1196 the statistical error.

1197 In Fig. 4.2e, the neutralino is always heavy enough to guarantee decay to a photon
 1198 that can pass the 40 GeV p_T cut. $\mathcal{A} \times \epsilon$ increases as M_3 increases because the larger
 1199 gluino-neutralino mass splitting gives the neutralino a larger kinetic energy, increasing
 1200 the chance that it will decay to a photon with 40 GeV p_T or higher. After the bino mass
 1201 increases beyond the threshold needed to produce high p_T photons, $\mathcal{A} \times \epsilon$ decreases
 1202 with increasing M_1 , independent of gluino mass, because higher M_1 means more phase

space is open to decays of the form $\tilde{\chi}_1^0 \rightarrow Z\tilde{G}$ and $\tilde{\chi}_1^0 \rightarrow H\tilde{G}$. The two-photon search
is naturally not as efficient for these decays.

Added

There is a small chance that some real GMSB signal events could be reconstructed as ff events in the data. To correct the signal acceptance for this effect, the number of signal events reconstructed as ff events is subtracted from the number of signal events, effectively reducing the signal acceptance. This is generally a small correction ($\sim 5\%$).

4.2.2 CL_s and the Profile Likelihood Test Statistic

The process of setting a cross section upper limit entails (1) defining a test statistic, (2) generating a distribution for that test statistic under the signal + background and background-only hypotheses, and (3) deciding whether or not the observed value of the test statistic is more compatible with the signal + background (i.e. weaker upper limit) or background-only (i.e. stronger upper limit) hypotheses by considering where it falls within the test statistic distributions. An important requirement on the choice of test statistic is that it be able to effectively discriminate between the signal + background and background-only hypotheses, i.e. the shape of its distribution for these two hypotheses should be different. The procedure for determining the excludability of a particular model given the value of the test statistic observed should not give rise to pathological behavior in the presence of small signals, low statistics, or weak sensitivity to models, as is commonly the case in high energy physics. These demands on the test statistic and the limit setting procedure itself dictate the choice of the profile likelihood test statistic and CL_s procedure.

In the remainder of this section, the notation is taken from ref. [68].

1226 **Profile Likelihood**

1227 For a specific model of GMSB, the limit setting procedure concerns the question of
 1228 whether to reject the signal + background hypothesis $\mu s + b$ in favor of the background-
 1229 only (Standard Model) hypothesis of b ($\mu = 0$). μ is a dimensionless signal strength
 1230 parameter. s is the expected number of signal events, calculated from MC simulated
 1231 signal events as in Secs. 4.1 and 4.2.1. b is the expected number of background events,
 1232 estimated in Chap. 3. By the Neyman-Pearson lemma [71], the ratio of the likelihood
 1233 of $\mu s + b$ to the likelihood of b is the test statistic with the highest power to reject $\mu s + b$
 1234 at whatever confidence level is desired. In practice, this means that the likelihood ratio
 1235 is the best discriminator between the GMSB and Standard Model hypotheses.

1236 The likelihood of the signal + background hypothesis as a function of the data
 1237 (either real or generated) is defined as

$$\mathcal{L}(\text{data}|\mu, \theta) = \prod_{i=1}^N \frac{(\mu s_i(\theta) + b_i(\theta))^{n_i}}{n_i!} e^{-\mu s_i(\theta) - b_i(\theta)} p(\tilde{\theta}|\theta) \quad (4.1)$$

1238 where $N = 5$ is the number of E_T bins used in the analysis ([50, 60) GeV, [60,
 1239 70) GeV, [70, 80) GeV, [80, 100) GeV, and [100, ∞) GeV); $s_i(\theta)$ and $b_i(\theta)$ are the
 1240 expected number of signal and background events in E_T bin i , respectively; n_i is the
 1241 number of events observed in E_T bin i ; and θ represents all the nuisance parameters
 1242 (uncertainties). $p(\tilde{\theta}|\theta)$ represents the product of probability distribution functions
 1243 (PDFs) for the nuisance parameters, where $\tilde{\theta}$ is the default value of the nuisance
 1244 parameter. In this analysis, there are eight experimental nuisance parameters per E_T
 1245 bin, given here as relative errors on the expected number of signal events:

- 1246 • Uncertainty on the measured integrated luminosity (4.5% in all bins) [72]
- 1247 • Uncertainty on the signal acceptance due to $\epsilon_e^{\text{data}}/\epsilon_e^{\text{MC}}$ and the pixel veto effi-
 1248 ciency error (cf. Sec. 2.4.2) (8% in all bins)

- 1249 ● Uncertainty on the signal acceptance due to imperfect pileup simulation (2.6%
 1250 in all bins)

- 1251 ● Systematic uncertainty on QCD background prediction due to difference be-
 1252 tween ff and ee estimates (5.5%-53% of the QCD background depending on
 1253 bin)

- 1254 ● Systematic uncertainty on electroweak background prediction due to p_T depen-
 1255 dence of $f_{e \rightarrow \gamma}$ (29%-30% of the electroweak background depending on bin)

- 1256 ● Statistical uncertainty on the signal acceptance (1.8%-100% depending on model
 1257 and bin)

- 1258 ● Statistical uncertainty on the QCD background prediction (7.2%-38% of the
 1259 QCD background depending on bin)

- 1260 ● Statistical uncertainty on the electroweak background prediction (3.6%-7.2% of
 1261 the electroweak background depending on bin)

 1262 and one very small theoretical nuisance parameter: the uncertainty on the signal
 1263 acceptance due to underlying parton distribution function (PDF) uncertainties. In
 1264 the limit-setting code, the uncertainties on signal acceptance due to photon efficiency
 1265 and PDF errors are added in quadrature and treated as one. The uncertainty on the
 1266 signal acceptance due to jet energy correction uncertainties is negligible, due to the
 1267 presence of many hard jets in GMSB signal events. The uncertainties on integrated
 1268 luminosity and pileup are 100% correlated between \cancel{E}_T bins, and the uncertainty on
 1269 signal acceptance can usually be treated similarly because the error on $\epsilon_e^{\text{data}}/\epsilon_e^{\text{MC}}$ often
 1270 dominates the PDF error on acceptance (although these three uncertainties are 0%
 1271 correlated with each other).

1272 To estimate the uncertainty due to imperfect simulation of LHC pileup, the square
 1273 of the average data efficiency for photons over the range 1-15 reconstructed primary

vertices (see Fig. 2.17a), weighted by the number of $\gamma\gamma$ events per primary vertex bin, is calculated. The efficiency per primary vertex bin is estimated from a linear fit to Fig. 2.17a. The process is repeated for MC using the entire range of primary vertices in Fig. 2.17a (all MC signal points have the same pileup simulation). The error is taken as $2 \times |\text{avg. data efficiency squared} - \text{avg. MC efficiency squared}| / (\text{avg. data efficiency squared} + \text{avg. MC efficiency squared})$.

Each nuisance parameter PDF is modeled by a log-normal distribution:

$$p(\tilde{\theta}|\theta) = \frac{1}{\sqrt{2\pi} \ln \kappa} \exp\left(-\frac{(\ln \tilde{\theta}/\theta)^2}{2(\ln \kappa)^2}\right) \frac{1}{\tilde{\theta}} \quad (4.2)$$

where $\tilde{\theta} = 1$ and $\kappa = 1 +$ the one-standard-deviation relative error on the nuisance parameter (e.g. for the 4.5% error due to integrated luminosity, $\kappa = 1.045$).

Similarly, the likelihood of the background-only hypothesis as a function of the data (either real or generated) is defined as

$$\mathcal{L}(\text{data}|0, \theta) = \prod_{i=1}^N \frac{b_i(\theta)^{n_i}}{n_i!} e^{-b_i(\theta)} p(\tilde{\theta}|\theta) \quad (4.3)$$

The profile likelihood test statistic is defined as

$$\tilde{q}_\mu = -2 \ln \frac{\mathcal{L}(\text{data}|\mu, \hat{\theta}_\mu)}{\mathcal{L}(\text{data}|\hat{\mu}, \hat{\theta})}, 0 \leq \hat{\mu} \leq \mu \quad (4.4)$$

where the $\hat{\theta}_\mu$ maximize $\mathcal{L}(\text{data}|\mu, \hat{\theta}_\mu)$ when it is evaluated at a particular μ , and $\hat{\mu}$ and $\hat{\theta}$ are the global maximum likelihood estimators of μ and θ . The condition $\hat{\mu} \leq \mu$ insures that the obtained cross section upper limit is one-sided, i.e. there is no possibility to find a lower limit on the cross section. The profile likelihood test

1290 statistic has the nice property that in the asymptotic (large statistics) limit its PDF
 1291 can be approximated by analytic formulae, eliminating the need to generate multiple
 1292 toy experiments to get the PDF. However, the approximation breaks down for small
 1293 numbers of observed events, so in practice the asymptotic limit is only used as a first
 1294 guess at the location of the true limit.

1295 The PDFs $f(\tilde{q}_\mu | \mu, \hat{\theta}_\mu^{\text{obs}})$ and $f(\tilde{q}_\mu | 0, \hat{\theta}_0^{\text{obs}})$ for the profile likelihood test statistic
 1296 under the signal + background and background-only hypotheses, respectively, are
 1297 obtained by generating toy MC pseudo-experiments. $\hat{\theta}_\mu^{\text{obs}}$ and $\hat{\theta}_0^{\text{obs}}$ maximize Eqs. 4.1
 1298 and 4.3, respectively, when they are evaluated for the observed data. For each μ (and
 1299 the background-only hypothesis $\mu = 0$), the pseudo-experiments are generated by
 1300 picking random values of s and b from a Poisson distribution with the θ fixed as just
 1301 described.

1302 **CL_s**

1303 In the classical frequentist approach, a signal model may be excluded at the 95%
 1304 confidence level (CL) if the probability of any measurement of the test statistic to be
 1305 greater than or equal to the observed value given the signal + background hypothesis
 1306 is 5%. This means that the observed value of the test statistic is so incompatible
 1307 with what one would expect to observe if the signal model were true that, under the
 1308 assumption that the signal model *is* true, the chance of observing a test statistic even
 1309 further afield from the signal expectation is only 5%. Mathematically,

$$\begin{aligned} p_\mu &\equiv P(\tilde{q}_\mu \geq \tilde{q}_\mu^{\text{obs}} | \mu s + b) = \int_{\tilde{q}_\mu^{\text{obs}}}^{\infty} f(\tilde{q}_\mu | \mu, \hat{\theta}_\mu^{\text{obs}}) d\tilde{q}_\mu \\ p_\mu &\leq 0.05 \Rightarrow \text{exclude } \mu \end{aligned} \quad (4.5)$$

1310 where $\tilde{q}_\mu^{\text{obs}}$ is the observed value of the test statistic and p_μ is the p-value. As indicated
 1311 in Eq. 4.5, the p-value is simply the integral of the PDF of \tilde{q}_μ from $\tilde{q}_\mu^{\text{obs}}$ to infinity.

1312 By construction, the classical 95% CL frequentist approach described above will
 1313 reject a true signal + background hypothesis 5% of the time. This can happen if the
 1314 experiment gets “unlucky” and the observation fluctuates low, causing $\tilde{q}_\mu^{\text{obs}}$ to fall in
 1315 the tail of the \tilde{q}_μ distribution. This poses a problem for the case of very weak signals
 1316 ($\mu \sim 0$), because it will lead to spurious exclusions of models to which the experiment
 1317 has little sensitivity. To avoid this pitfall, the CL_s limit setting method is used.

1318 In the CL_s method, the classical frequentist p-value of Eq. 4.5 is simply divided by
 1319 one minus the p-value of the background-only hypothesis, and it is this ratio, rather
 1320 than the p-value of the signal + background hypothesis alone, that is required to be
 1321 ≤ 0.05 . Mathematically,

$$1 - p_0 \equiv P(\tilde{q}_\mu \geq \tilde{q}_\mu^{\text{obs}} | b) = \int_{\tilde{q}_\mu^{\text{obs}}}^{\infty} f(\tilde{q}_\mu | 0, \hat{\theta}_0^{\text{obs}}) d\tilde{q}_\mu \quad (4.6)$$

$$\text{CL}_s(\mu) \equiv \frac{p_\mu}{1 - p_0} \quad (4.7)$$

$$\text{CL}_s(\mu) \leq 0.05 \Rightarrow \text{exclude } \mu$$

1322 where p_0 is the p-value for the background-only hypothesis ($\mu = 0$). In the case of
 1323 low sensitivity to μ , $p_\mu \lesssim 1 - p_0$, so $\text{CL}_s(\mu) \lesssim 1$ and μ will not be excluded. On the
 1324 contrary, for high sensitivity to μ ($\mu s \gg \sigma_b$), $p_\mu \ll 1 - p_0$, so models that can be
 1325 excluded by the criterion $p_\mu \leq 0.05$ will also be excluded by the criterion $\text{CL}_s \leq 0.05$.
 1326 Compared to the classical frequentist method, CL_s limits can be a little stronger in
 1327 the case of low signal sensitivity [68].

1328 To determine the upper limit on the cross section of a particular model, the lowest
 1329 value of μ for which $\text{CL}_s(\mu) \leq 0.05$, denoted $\mu^{95\% \text{CL}}$, is found. The cross section upper
 1330 limit of that model is then simply $\mu^{95\% \text{CL}}$ multiplied by the expected cross section of

1331 the model (cf. Fig. 4.1).

1332 In contrast to the observed upper limit, the expected upper limit is calculated from
 1333 an ensemble of background-only MC pseudo-experiments. The distribution $f(\mu_{\text{pseudo}}^{\text{95%CL}})$
 1334 is plotted (one entry per pseudo-experiment). The median expected upper limits and
 1335 $\pm 1\sigma$ and $\pm 2\sigma$ bands are defined as

$$0.5 = \int_0^{\mu_{\text{exp}}^{\text{95%CL}}} f(\mu_{\text{pseudo}}^{\text{95%CL}}) d\mu_{\text{pseudo}}^{\text{95%CL}} \quad (4.8)$$

$$0.16 = \int_0^{\mu_{-1\sigma,\text{exp}}^{\text{95%CL}}} f(\mu_{\text{pseudo}}^{\text{95%CL}}) d\mu_{\text{pseudo}}^{\text{95%CL}} \quad (4.9)$$

$$0.84 = \int_0^{\mu_{+1\sigma,\text{exp}}^{\text{95%CL}}} f(\mu_{\text{pseudo}}^{\text{95%CL}}) d\mu_{\text{pseudo}}^{\text{95%CL}} \quad (4.10)$$

$$0.025 = \int_0^{\mu_{-2\sigma,\text{exp}}^{\text{95%CL}}} f(\mu_{\text{pseudo}}^{\text{95%CL}}) d\mu_{\text{pseudo}}^{\text{95%CL}} \quad (4.11)$$

$$0.975 = \int_0^{\mu_{+2\sigma,\text{exp}}^{\text{95%CL}}} f(\mu_{\text{pseudo}}^{\text{95%CL}}) d\mu_{\text{pseudo}}^{\text{95%CL}} \quad (4.12)$$

1336 The technical procedure followed to calculate the 95% CL cross section upper
 1337 limits for each GMSB model tested is given below.

1338 1. Calculate a guess for the median expected limit and $\pm 2\sigma$ error bands ($\mu_{\pm 2\sigma,\text{guess}}^{\text{95%CL}}$)
 1339 using the asymptotic formulae for $f(\tilde{q}_\mu | 0, \hat{\theta}_0^{\text{obs}})$.

1340 2. Calculate observed ($\mu_{\text{obs,asym}}^{\text{95%CL}}$), median expected ($\mu_{\text{exp,asym}}^{\text{95%CL}}$), and $\pm 1\sigma$ ($\mu_{\pm 1\sigma,\text{asym}}^{\text{95%CL}}$)
 1341 and $\pm 2\sigma$ ($\mu_{\pm 2\sigma,\text{asym}}^{\text{95%CL}}$) expected CL_s limits using the asymptotic formulae for
 1342 $f(\tilde{q}_\mu | \mu, \hat{\theta}_\mu^{\text{obs}})$ and $f(\tilde{q}_\mu | 0, \hat{\theta}_0^{\text{obs}})$. Restrict the range of $\mu_{\text{obs,asym}}^{\text{95%CL}}$ and $\mu_{\text{exp,asym}}^{\text{95%CL}}$ to
 1343 $[0, 5 \times \mu_{\pm 2\sigma,\text{guess}}^{\text{95%CL}}]$ (this avoids pathological behavior of the limit-setting code
 1344 when the expected number of signal events is much greater than the observed
 1345 number of events and only introduces a $\sim 5\%$ upward bias in the observed limit,
 1346 well within the $\pm 1\sigma$ error bands).

1347 3. Calculate median expected ($\mu_{\text{exp}}^{\text{95%CL}}$) and $\pm 1\sigma$ ($\mu_{\pm 1\sigma}^{\text{95%CL}}$) and $\pm 2\sigma$ ($\mu_{\pm 2\sigma}^{\text{95%CL}}$) ex-

1348 pected CL_s limits using 100 toy MC pseudo-experiments to generate $f(\tilde{q}_\mu|\mu, \hat{\theta}_\mu^{\text{obs}})$
 1349 and $f(\tilde{q}_\mu|0, \hat{\theta}_0^{\text{obs}})$. Restrict the range of $\mu_{\text{exp}}^{95\%\text{CL}}$ to $[0, 5 \times \mu_{\pm 2\sigma, \text{guess}}^{95\%\text{CL}}]$.

1350 4. If $\mu_{\pm 2\sigma}^{95\%\text{CL}}$ could not be calculated, set $\mu_{\pm 2\sigma}^{95\%\text{CL}} = \mu_{\pm 2\sigma, \text{asym}}^{95\%\text{CL}}$ instead.

1351 5. If $\mu_{+2\sigma}^{95\%\text{CL}} \neq \mu_{-2\sigma}^{95\%\text{CL}}$ and $\mu_{\text{obs}, \text{asym}}^{95\%\text{CL}} > 0.0001$:

1352 • If $\mu_{\text{obs}, \text{asym}}^{95\%\text{CL}} > \mu_{+2\sigma}^{95\%\text{CL}}$, set $\mu_{+2\sigma}^{95\%\text{CL}} = 1.3 \times \mu_{\text{obs}, \text{asym}}^{95\%\text{CL}}$.

1353 • If $\mu_{\text{obs}, \text{asym}}^{95\%\text{CL}} < \mu_{-2\sigma}^{95\%\text{CL}}$, set $\mu_{-2\sigma}^{95\%\text{CL}} = 0.7 \times \mu_{\text{obs}, \text{asym}}^{95\%\text{CL}}$.

1354 6. If $\mu_{+2\sigma}^{95\%\text{CL}} = \mu_{-2\sigma}^{95\%\text{CL}}$, set $\mu_{\pm 2\sigma}^{95\%\text{CL}} = \mu_{\pm 2\sigma, \text{asym}}^{95\%\text{CL}}$ instead.

1355 7. Scan over 100 equally spaced test values of μ between $\mu_{-2\sigma}^{95\%\text{CL}}$ and $\mu_{+2\sigma}^{95\%\text{CL}}$ and,
 1356 if $\mu > 0.0001$, calculate the CL_s p-value (p_μ) for this test value of μ to 10^{-6}
 1357 precision using a minimum of 500 toy experiments to generate $f(\tilde{q}_\mu|\mu, \hat{\theta}_\mu^{\text{obs}})$ and
 1358 $f(\tilde{q}_\mu|0, \hat{\theta}_0^{\text{obs}})$.

1359 8. Determine the observed ($\mu_{\text{obs}, \text{scan}}^{95\%\text{CL}}$), median expected ($\mu_{\text{exp}, \text{scan}}^{95\%\text{CL}}$), and $\pm 1\sigma$ ($\mu_{\pm 1\sigma, \text{scan}}^{95\%\text{CL}}$)
 1360 and $\pm 2\sigma$ ($\mu_{\pm 2\sigma, \text{scan}}^{95\%\text{CL}}$) expected CL_s limits from the scan p-values for the signal
 1361 + background and background-only pseudo-experiments.

1362 Finally, a particular GMSB model is excluded if the upper limit on the cross
 1363 section for that model is less than the expected theoretical cross section.

1364 4.3 Cross Section Upper Limits

1365 Figure 4.3 shows the observed upper limits on the cross sections for the models de-
 1366 scribed in Sec. 4.1. In some ($\mathcal{O}(10^{-3})$) cases, the upper limit is zero due to a com-
 1367 putational failure. The upper limit for these points is estimated from the average of the
 1368 upper limits of the four neighboring points, as shown in Figure 4.4. If any of the four
 1369 points is also missing a valid upper limit, it is dropped from the average. The errors

1370 on the individual upper limits used in the estimate are propagated to the error on
 1371 the average.

1372 4.4 Exclusion Contours

1373 Exclusion contours for the GMSB models discussed above are shown in Figure 4.5. The
 1374 contours are derived from plots of predicted cross section minus cross section upper
 1375 limit ($\sigma \times (1 - \mu^{95\%CL})$), where σ is the nominal value of the predicted cross section
 1376 for a given GMSB model) vs. the two model parameters of interest, so the values are
 1377 either negative (not excluded) or positive (excluded). Sometimes, a particular point
 1378 may have a different sign than its four same-sign neighbors (cf. Fig. 4.4) due to a
 1379 fluctuation. In these cases, $\sigma \times (1 - \mu^{95\%CL})$ for the anomalous point is estimated
 1380 as the average $\sigma \times (1 - \mu^{95\%CL})$ of the four neighboring points. The errors on the
 1381 individual values of $\sigma \times (1 - \mu^{95\%CL})$ used in the estimate are propagated to the error
 1382 on the average.

1383 In the plots in Fig. 4.5, the expected limit (i.e. the contour derived from $\sigma \times (1 -$
 1384 $\mu_{\text{exp,scan}}^{95\%CL})$) is drawn in dark orange and the 1σ experimental band around the expected
 1385 limit (i.e. the shaded region between the contours derived from $\sigma \times (1 - \mu_{\pm 1\sigma, \text{scan}}^{95\%CL})$) is
 1386 drawn in light orange. The values of $\mu_{\text{exp,scan}}^{95\%CL}$ and $\mu_{\pm 1\sigma, \text{scan}}^{95\%CL}$ only reflect the experimental
 1387 uncertainties given in Sec. 4.2.2.

1388 The observed limits (derived from $\sigma \times (1 - \mu_{\text{obs,scan}}^{95\%CL})$) and 1σ theoretical error
 1389 bands around the observed limits in Fig. 4.5 are drawn in blue. The contours that
 1390 define this band are derived from $\pm(\sigma_{\pm 1\sigma} - \sigma \mu_{\text{obs,scan}}^{95\%CL})$, where $\sigma_{\pm 1\sigma}$ is the nominal
 1391 value of the predicted cross section \pm the one-standard-deviation theoretical error on
 1392 the predicted cross section. In this way, the experimental and theoretical errors, the
 1393 latter due to imperfect knowledge of the predicted cross section, are shown separately.
 1394 Comparing with Fig. 4.1, one can easily see that the shapes of the exclusion curves

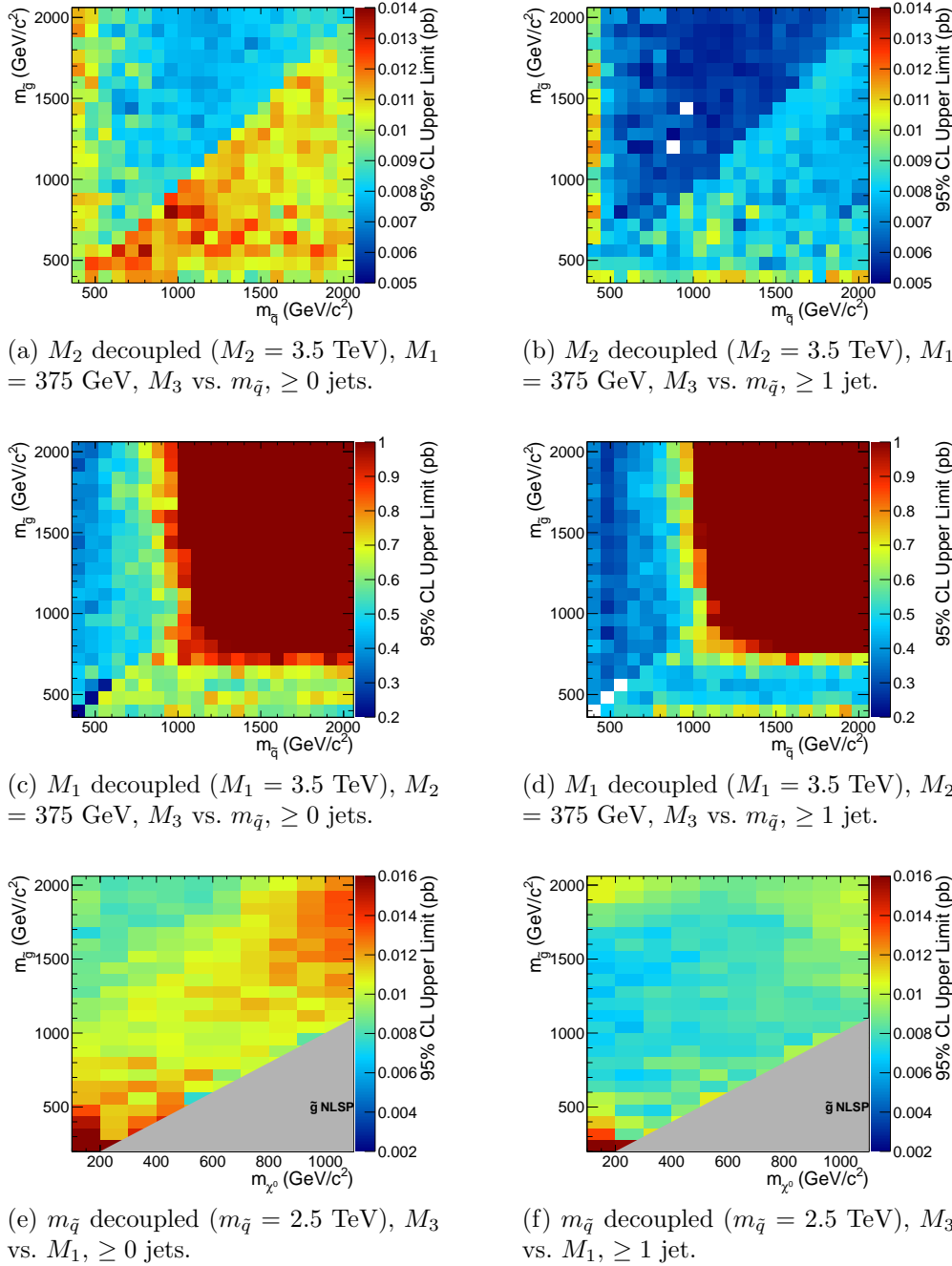


Figure 4.3: Cross section upper limits for the three different scenarios described in Sec. 4.1.

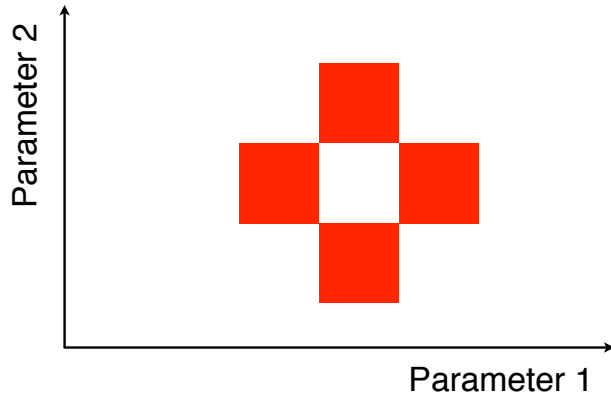


Figure 4.4: Diagram of the points (red squares) used in the estimation of an upper limit when a computational failure occurs (middle white square).

¹³⁹⁵ are driven by the contours in the expected cross section plane.

¹³⁹⁶ The dominant theoretical uncertainties on the GMSB cross sections are due to:

¹³⁹⁷ • PDF uncertainty (4%-100% depending on model)

¹³⁹⁸ • Renormalization scale uncertainty (0.036%-25% depending on model)

¹³⁹⁹ The PDF4LHC [73] recommendations are used to calculate the effect of these uncer-
¹⁴⁰⁰ tainties on the GMSB cross sections. The recommendations state that PDF sets from
¹⁴⁰¹ MSTW08 [74], CTEQ6.6 [75], and NNPDF2.0 [76] should be considered in the deter-
¹⁴⁰² mination of the PDF uncertainties, because these three PDF sets include constraints
¹⁴⁰³ from the Tevatron and from fixed target experiments, as well as from HERA [?], and
¹⁴⁰⁴ are thus the most complete.

¹⁴⁰⁵ Each collaboration's PDF prediction comes from a global fit to experimental data
¹⁴⁰⁶ with a certain number of free parameters. The best fit parameters come from mini-
¹⁴⁰⁷ mizing the χ^2 ; increasing the χ^2 by one from its minimum can be written in terms of
¹⁴⁰⁸ the N -dimensional Hessian error matrix [?] where N is the number of free parameters.

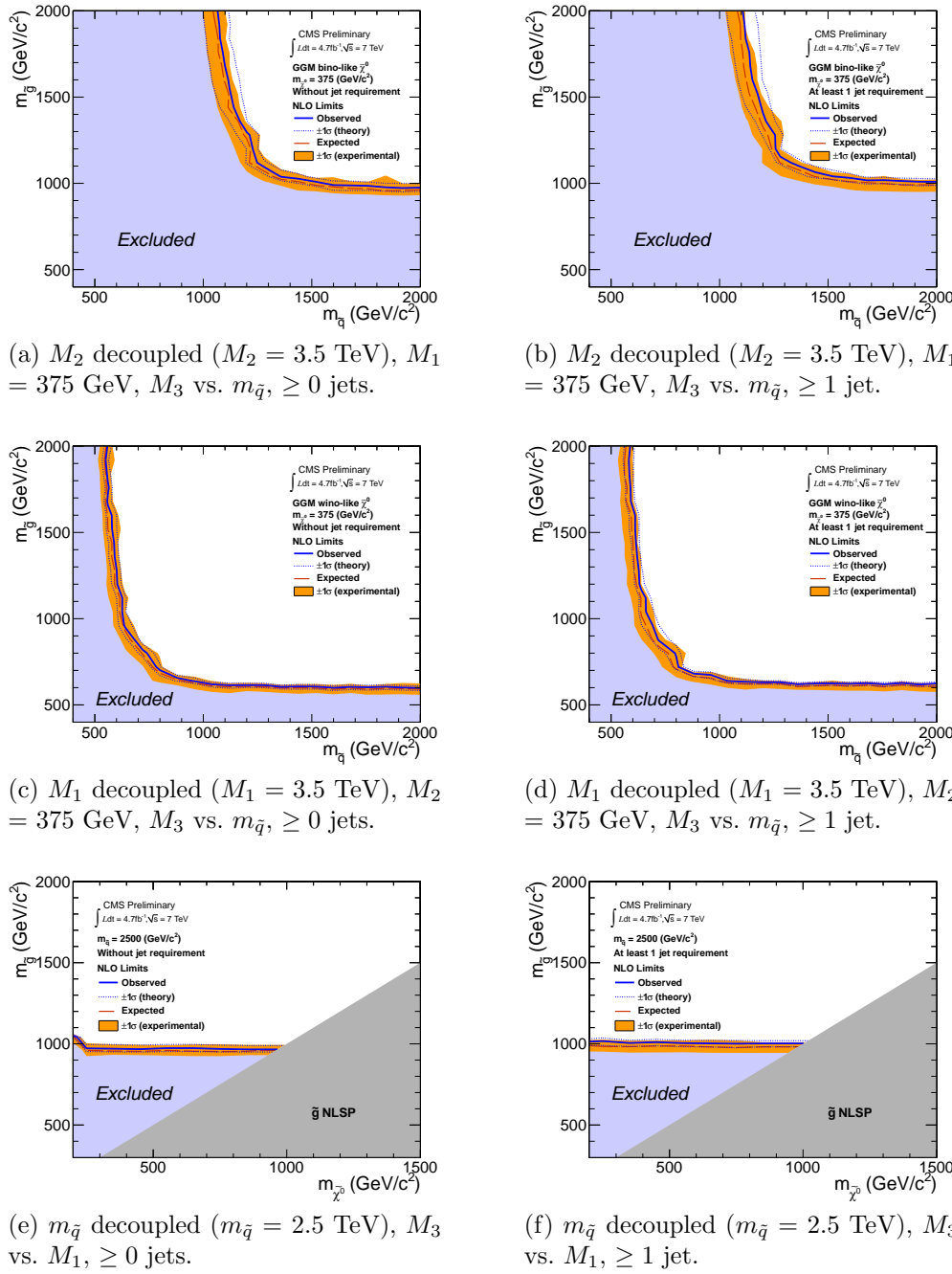


Figure 4.5: Exclusion contours for the three different scenarios described in Sec. 4.1.

1409 To form the i^{th} pair of members of the PDF set, the PDF is evaluated once at the
 1410 parameter values given by the i^{th} eigenvector of the Hessian matrix, and then again
 1411 at the parameter values given by the negative of the i^{th} eigenvector. Each PDF set
 1412 therefore contains $2N$ members, corresponding to the positive and negative values of
 1413 the N eigenvectors [77].

1414 To calculate the PDF uncertainties for a given GMSB model, the leading order
 1415 Pythia cross section is reweighted by a factor of the error PDF divided by the leading
 1416 order PDF with which the model was generated. This is repeated for each error PDF
 1417 in a given PDF set. The $\pm 1\sigma$ deviations are proportional to the maximum difference
 1418 between cross sections obtained this way. The actual equation for the $\pm 1\sigma$ errors is
 1419 Eq. (43) of ref. [77]. In the same way, the $\pm 1\sigma$ errors are calculated for the CTEQ6.6,
 1420 MSTW08, and NNPDF2.0 PDF sets. The total error is given by the half the difference
 1421 between the largest $+1\sigma$ deviation and the smallest -1σ deviation [73].

1422 The uncertainties on the signal cross sections due to the choice of renormaliza-
 1423 tion/factorization scale ($\alpha_S(M_Z)$) are evaluated by calculating the PROSPINO next
 1424 to leading order cross section once with $\alpha_S(M_Z)$ halved, then once with $\alpha_S(M_Z)$ dou-
 1425 bled. The lower error on the cross section is taken as the absolute difference between
 1426 the nominal and halved-scale values of the cross section, while the upper error is taken
 1427 as the absolute difference between the nominal and doubled-scale values. The PDF
 1428 and α_S uncertainties are added in quadrature to give the total PDF uncertainty.

1429 Note that the quoted GMSB cross sections are evaluated at next to leading order
 1430 using PROSPINO, but it is the leading order Pythia cross sections that are reweighted
 1431 to the next to leading order MSTW08, CTEQ6.6, and NNPDF2.0 PDFs to get the
 1432 error bands. In addition, since to a good approximation the GMSB production cross
 1433 sections for the M_3 - $m_{\tilde{q}}$ scans only depend on M_3 and $m_{\tilde{q}}$, the same PDF errors per
 1434 point are used for the \tilde{B} -like and \tilde{W} -like grids.

¹⁴³⁵ **Appendix A**

¹⁴³⁶ **Monte Carlo Samples**

¹⁴³⁷ A number of MC samples are utilized in this analysis and referred to throughout the
¹⁴³⁸ text. Below is a list of the MC samples used and an explanation of what the sample
¹⁴³⁹ names mean.

¹⁴⁴⁰ **A.0.1 List of Samples**

¹⁴⁴¹ 1. Drell-Yan:

¹⁴⁴² /DYJetsToLL_TuneZ2_M-50_7TeV-madgraph-tauola/
¹⁴⁴³ Fall11-PU_S6_START42_V14B-v1/AODSIM

¹⁴⁴⁴ 2. QCD enriched with B and D meson decays to electrons:

¹⁴⁴⁵ /QCD_Pt-20to30_BCToE_TuneZ2_7TeV-pythia6/
¹⁴⁴⁶ Fall11-PU_S6_START42_V14B-v1/AODSIM,
¹⁴⁴⁷ /QCD_Pt-30to80_BCToE_TuneZ2_7TeV-pythia6/
¹⁴⁴⁸ Fall11-PU_S6_START42_V14B-v1/AODSIM,
¹⁴⁴⁹ /QCD_Pt-80to170_BCToE_TuneZ2_7TeV-pythia6/
¹⁴⁵⁰ Fall11-PU_S6_START42_V14B-v1/AODSIM

¹⁴⁵¹ 3. Photon + jet doubly enriched with jets passing an EM filter:

1452 /GJet_Pt-20_doubleEMEnriched_TuneZ2_7TeV-pythia6/
 1453 Fall11-PU_S6_START42_V14B-v1/AODSIM

1454 4. W leptonic decays:

1455 /WJetsToLNu_TuneZ2_7TeV-madgraph-tauola/
 1456 Fall11-PU_S6_START42_V14B-v1/AODSIM

1457 5. $t\bar{t}$:

1458 /TTJets_TuneZ2_7TeV-madgraph-tauola/
 1459 Fall11-PU_S6_START42_V14B-v2/AODSIM

1460 A.0.2 Explanation of Naming Conventions

1461 • L: charged lepton

1462 • B: B hadron

1463 • C: D , or charmed, hadron

1464 • E: electron or positron

1465 • G: photon

1466 • W: W boson

1467 • Nu: neutrino

1468 • T: top quark

1469 • TuneZ2: Pythia tune incorporating 2010 LHC data with CTEQ6L1 [75] PDFs
 1470 [82]

1471 • M-50: Generated l^+l^- invariant mass threshold of 50 GeV

1472 • 7TeV: Generated center-of-mass energy 7 TeV

- 1473 • **pythia6**: Parton showering and hadronization simulated with Pythia v6.424
- 1474 [83]
- 1475 • **madgraph**: Hard interaction generated with MadGraph [84]
- 1476 • **tauola**: τ decays generated with Tauola [85]
- 1477 • **PU_S6**: Generated with S6 pileup scenario
- 1478 • **START42_V14B**: Reconstructed with best alignment and calibration constants
1479 and magnetic field conditions as of August 3, 2011
- 1480 • **Pt_XtoY**: $X \leq$ generated $\hat{p}_T < Y$
- 1481 • **BCToE**: Enriched in B and D meson decays to electrons
- 1482 • **doubleEMEnriched**: Enriched in electromagnetic jets

1483

Bibliography

- 1484 [1] S.L. Glashow, J. Iliopoulos, and L. Maiani, *Phys. Rev. D* **2** (1970) 1285; S.L.
1485 Glashow, *Nucl. Phys.* **22(4)** (1961) 579; J. Goldstone, A. Salam, and S. Weinberg,
1486 *Phys. Rev.* **127** (1962) 965; S. Weinberg, *Phys. Rev. Lett.* **19** (1967) 1264; A.
1487 Salam and J.C. Ward, *Phys. Lett.* **13(2)** (1964) 168.
- 1488 [2] M. Gell-Mann, *Phys. Lett.* **8** (1964) 214; G. Zweig, *CERN 8419/TH. 412* (1964)
1489 (unpublished).
- 1490 [3] J. Drees, *Int. J. Mod. Phys.* **A17** (2002) 3259.
- 1491 [4] P.W. Higgs, *Phys. Lett.* **12(2)** (1964) 132; P.W. Higgs, *Phys. Rev. Lett.* **13** (1964)
1492 508; P.W. Higgs, *Phys. Rev.* **145** (1966) 1156.
- 1493 [5] I. Aitchison, *Supersymmetry in Particle Physics: An Elementary Introduction*
1494 (Cambridge University Press, Cambridge 2007), p. 4.
- 1495 [6] S. P. Martin, *A Supersymmetry Primer* **v4** (2006) 86. [arXiv:hep-ph/9709356](https://arxiv.org/abs/hep-ph/9709356).
- 1496 [7] M. Dine and W. Fischler, *Phys. Lett.* **B110** (1982) 227; C.R. Nappi and B.A.
1497 Ovrut, *Phys. Lett.* **B113** (1982) 175; L. Alvarez-Gaumé, M. Claudson, and M.B.
1498 Wise, *Nucl. Phys.* **B207** (1982) 96; M. Dine and A.E. Nelson, *Phys. Rev.* **D48**
1499 (1993) 1277; M. Dine, A.E. Nelson, and Y. Shirman, *Phys. Rev.* **D51** (1995)
1500 1362; M. Dine, A.E. Nelson, Y. Nir, and Y. Shirman, *Phys. Rev.* **D53** (1996)
1501 2658.

- 1502 [8] A.H. Chamseddine, R. Arnowitt, and P. Nath, *Phys. Rev. Lett.* **49** (1982) 970; R.
 1503 Barbieri, S. Ferrara, and C.A. Savoy, *Phys. Lett.* **B119** (1982) 343; L.E. Ibáñez,
 1504 *Phys. Lett.* **B118** (1982) 73; L.J. Hall, J.D. Lykken, and S. Weinberg, *Phys. Rev.*
 1505 **D27** (1983) 2359; N. Ohta, *Prog. Theor. Phys.* **70** (1983) 542; J. Ellis, D.V.
 1506 Nanopoulos, and K. Tamvakis, *Phys. Lett.* **B121** (1983) 123; L. Alvarez-Gaumé,
 1507 J. Polchinski, and M. Wise, *Nucl. Phys.* **B221** (1983) 495.
- 1508 [9] P. Meade, N. Seiberg, and D. Shih, *Progr. Theor. Phys. Suppl.* **177** (2009) 143.
- 1509 [10] G. Aad et al., *CERN-PH-EP-2011-160* (2011).
- 1510 [11] T. Aaltonen et al., *Phys. Rev. Lett.* **104** (2010) 011801.
- 1511 [12] CMS Collaboration, *CMS-PAS-SUS-11-009* (2011).
- 1512 [13] <http://en.wikipedia.org/wiki/Tevatron>.
- 1513 [14] E. Fernandez et al., *Phys. Rev. Lett.* **54** (1985) 1118; E. Fernandez et al., *Phys.*
 1514 *Rev.* **D35** (1987) 374; D. Decamp et al., *Phys. Lett.* **B237(2)** (1990) 291; F.
 1515 Abe et al., *Phys. Rev. Lett.* **75** (1995) 613; S. Abachi et al., *Phys. Rev. Lett.* **75**
 1516 (1995) 618; G. Alexander et al., *Phys. Lett.* **B377(4)** (1996) 273; S. Aid et al.,
 1517 *Z. Phys.* **C71(2)** (1996) 211; S. Aid et al., *Phys. Lett.* **B380(3-4)** (1996) 461; B.
 1518 Aubert et al., *Phys. Rev. Lett.* **95** (2005) 041802.
- 1519 [15] O. Buchmueller et al., *CERN-PH-TH/2011-220* (2011).
- 1520 [16] <https://twiki.cern.ch/twiki/bin/view/CMSPublic/PhysicsResultsSUS>.
- 1521 [17] G. Aad et al., *JINST* **3** (2008) S08003.
- 1522 [18] B.C. Allanach et al., *Eur. Phys. J.* **C25** (2002) 113.
- 1523 [19] CMS Collaboration, *CMS-PAS-SUS-12-001* (2012).

- 1524 [20] A. Boyarsky, J. Lesgourges, O. Ruchayskiy, and M. Viel, *CERN-PH-TH/2008-*
 1525 *234* (2009).
- 1526 [21] E. Komatsu et al., *Astrophys. J. Suppl. Ser.* **180** (2009) 330.
- 1527 [22] C.-H. Chen and J.F. Gunion, *Physical Review D***58** (1998) 075005.
- 1528 [23] F. Staub, W. Porod, J. Niemeyer, *JHEP* **1001** (2010) 058.
- 1529 [24] S. Chatrchyan et al. (CMS Collaboration), *JINST* **3** (2008) S08004.
- 1530 [25] R. Brunelière, *Nucl. Instr. Meth. Res.* **A572** (2007) 33.
- 1531 [26] S. Chatrchyan et al. (CMS Collaboration), *JINST* **5** (2010) T03011.
- 1532 [27] CMS Collaboration, *CMS PAS EGM-10-002* (2010).
- 1533 [28] P. Meridiani and C. Seez, *CMS IN-2011/002* (2011).
- 1534 [29] P. Adzic et al. (CMS Electromagnetic Calorimeter Group), *Eur. Phys. J.* **C44S2**
 1535 (2006) 1.
- 1536 [30] P. Adzic et al. (CMS Electromagnetic Calorimeter Group), *JINST* **3** (2008)
 1537 P10007.
- 1538 [31] M. Malberti, *Nuc. Sci. Symposium Conference Record NSS/MIC IEEE* (2009)
 1539 2264.
- 1540 [32] S. Chatrchyan et al. (CMS Collaboration), *JINST* **5** (2010) T03010.
- 1541 [33] R. Paramatti, *J. Phys. Conf. Ser.* **293** (2011) 012045.
- 1542 [34] Y. Yang, [http://www.hep.caltech.edu/cms/posters/Pi0Poster_](http://www.hep.caltech.edu/cms/posters/Pi0Poster_CMSWeekDec2011.pdf)
 1543 CMSWeekDec2011.pdf (2011).
- 1544 [35] M. Anderson, A. Askew, A.F. Barfuss, D. Evans, F. Ferri, K. Kaadze, Y. Maravin,
 1545 P. Meridiani, and C. Seez, *CMS IN-2010/008* (2010).

- 1546 [36] <https://twiki.cern.ch/twiki/bin/view/CMS/ECALEnergyScaleCorrections>.
- 1547 [37] The H $\rightarrow \gamma\gamma$ working group, *CMS AN-2011/426* (2011).
- 1548 [38] M. Cacciari, *LPTHE-P06-04* (2006).
- 1549 [39] M. Cacciari, G.P. Salam, and G. Soyez, *CERN-PH-TH-2011-297* (2011).
- 1550 [40] S. Chatrchyan et al. (CMS Collaboration), *Phys. Rev. Lett.* **106** (2011) 082001.
- 1551 [41] A. Askew, B. Cox, D. Elvira, Y. Gershtein, M. Hildreth, D. Jang, Y.-F. Liu, D.
1552 Mason, D. Morse, U. Nauenberg, M. Paulini, R. Stringer, R. Yohay, and S.L.
1553 Zang, *CMS AN-2011/515* (2011).
- 1554 [42] F. Beaudette, D. Benedetti, P. Janot, and M. Pioppi, *CMS AN-2010/034* (2010).
- 1555 [43] M. Konecki, in Proceedings of the European Physical Society Europhysics Con-
1556 ference on High Energy Physics, Krakow, 2009, Eur. Phys.Soc. Mulhouse (ed.)
1557 (unpublished).
- 1558 [44] W. Adam, R. Früwirth, A. Strandlie, and T. Todorov, *J. Phys.* **G31** No. 9 (2005).
- 1559 [45] CMS Collaboration, *CMS PAS PFT-09-001* (2009).
- 1560 [46] CMS Collaboration, *CMS PAS PFT-10-002* (2010).
- 1561 [47] S. Chatrchyan et al., *JINST* **6** (2011) P11002.
- 1562 [48] CMS Collaboration, *CERN-PH-EP 2011-102* (2011).
- 1563 [49] M. Cacciari, G.P. Salam, and G. Soyez, *JHEP* **0804** (2008) 063.
- 1564 [50] G. Salam, talk given at CERN Theory Institute: SM and BSM Physics at the
1565 LHC (2009).
- 1566 [51] C.W. Fabjan and R. Wigmans, *Rep. Prog. Phys.* **52** (1989) 1519.

- 1567 [52] <http://www-cdf.fnal.gov/physics/new/top/2004/jets/cdfpublic.html>
 1568 (visited on 16 January 2011).
- 1569 [53] S. Chatrchyan et al. (CMS Collaboration), *JINST* **6** (2011) P09001.
- 1570 [54] CMS Collaboration, *CMS PAS JME-09-002* (2009).
- 1571 [55] T. Sjöstrand, S. Mrenna, and P. Z. Skands, *Comput. Phys. Commun.* **178** (2008)
 1572 852.
- 1573 [56] S. Chatrchyan et al. (CMS Collaboration), *JINST* **5** (2010) T03014.
- 1574 [57] J. P. Chou, S. Eno, S. Kunori, S. Sharma, and J. Wang, *CMS IN-2010/006*
 1575 (2010).
- 1576 [58] Y. Chen, talk given at a meeting of the CMS JetMET group (2011).
- 1577 [59] R. Korzekwa et al., *iEEE Trans. Elec. Dev.* **38** (1991) 745.
- 1578 [60] W. Adam, Th. Speer, B. Mangano, and T.Todorov, *CMS NOTE* **2006/041**
 1579 (2006).
- 1580 [61] G. Daskalakis, D. Evans, C.S. Hill, J. Jackson, P. Vanlaer, J. Berryhill, J. Haupt,
 1581 D. Futyian, C. Seez, C. Timlin, and D. Wardrope, *CMS AN-2007/019* (2007).
- 1582 [62] F. James and M. Roos, *Comput. Phys. Commun.* **10** (1975) 343.
- 1583 [63] W. Verkerke and D.P. Kirkby, *CHEP-2003-MOLT007* (2003).
- 1584 [64] J.E. Gaiser, Ph.D. thesis, Stanford University (1982).
- 1585 [65] A. Askew, S. Arora, Y. Gershtein, S. Thomas, G. Hanson, R. Stringer, W. Flana-
 1586 gan, B. Heyburn, U. Nauenberg, S.L. Zang, R. Nandi, D. Elvira, D. Mason, M.
 1587 Balazs, B. Cox, B. Francis, A. Ledovskoy, and R. Yohay, *CMS AN* **2010/271**
 1588 (2010).

- 1589 [66] Information about all CMS datasets is available from the CMS Data Aggregation
 1590 System (DAS), located at the URL <https://cmsweb.cern.ch/das/>.
- 1591 [67] S. Chatrchyan et al., *Phys. Rev. Lett.* **106** (2011) 211802.
- 1592 [68] G. Aad et al. (ATLAS Collaboration), S. Chatrchyan et al. (CMS Collaboration),
 1593 and LHC Higgs Combination Group, *CMS-NOTE-2011/005* (2011).
- 1594 [69] A.L. Read, in *Proceedings of the First Workshop on Confidence Limits, Geneva,*
 1595 2000, edited by L. Lyons, Y. Perrin, and F.E. James (CERN, Geneva, 2000), p.
 1596 81.
- 1597 [70] G. Cowan, K. Cranmer, E. Gross, and O. Vitells, *Eur. Phys. J.* **C71** (2011) 1554.
- 1598 [71] J. Neyman and E.S. Pearson, *Phil. Trans. R. Soc. Lond.* **A231** (1933) 289.
- 1599 [72] CMS Collaboration, *CMS PAS EWK-11-001* (2011).
- 1600 [73] S. Alekhin et al. (The PDF4LHC Working Group), [arXiv:1101.0536 \[hep-ph\]](https://arxiv.org/abs/1101.0536);
 1601 M. Botje et al. (The PDF4LHC Working Group), [arXiv:1101.0538 \[hep-ph\]](https://arxiv.org/abs/1101.0538);
 1602 <http://www.hep.ucl.ac.uk/pdf4lhc/index.html>.
- 1603 [74] A.D. Martin, W.J. Stirling, R.S. Thorne, and G. Watt, *Eur. Phys. J.* **C63** (2009)
 1604 189.
- 1605 [75] P. M. Nadolsky, H.-L. Lai, Q.-H. Cao, J. Huston, J. Pumplin, D. Stump, W.-K.
 1606 Tung, and C.-P. Yuan, *Phys. Rev.* **D78** (2008) 013004.
- 1607 [76] R.D. Ball, L. Del Debbio, S. Forte, A. Guffanti, J.I. Latorre, J. Rojo, and M.
 1608 Ubiali, *Nucl. Phys.* **B838** (2010) 136.
- 1609 [77] J.M. Campbell, J.W. Huston, and W.J. Stirling, *Rep. Prog. Phys.* **70** (2007) 89.
- 1610 [78] A. Djouadi, J.-L. Kneur, G. Moultaka, [arXiv:hep-ph/0211331](https://arxiv.org/abs/hep-ph/0211331) (2005).

- ₁₆₁₁ [79] M. Muhlleitner, A. Djouadi, Y. Mambrini, *Comput. Phys. Commun.* **168** (2005) 46.
- ₁₆₁₂
- ₁₆₁₃ [80] J. Allison et al., *IEEE Trans. Nucl. Sci.* **53**(1) (2006) 270.
- ₁₆₁₄ [81] W. Beenakker, R. Hoepker, M. Spira, [arXiv:hep-ph/9611232](https://arxiv.org/abs/hep-ph/9611232) (1996).
- ₁₆₁₅ [82] R. Field, talk given at LHC Physics Centre at CERN Minimum Bias and Underlying Event Working Group Meeting (2011).
- ₁₆₁₆
- ₁₆₁₇ [83] T. Sjöstrand, S. Mrenna, and P. Z. Skands, *JHEP* **0605** (2006) 026.
- ₁₆₁₈ [84] dummy
- ₁₆₁₉ [85] dummy